

# RESOURCE-EFFICIENT QUANTUM ALGORITHMS FOR QUANTUM CHEMISTRY

**Chee Chong Hian**  
*(B. Sc. (Hons.) in Physics, NTU)*

A THESIS SUBMITTED  
FOR THE DEGREE OF DOCTOR OF PHILOSOPHY  
CENTRE FOR QUANTUM TECHNOLOGIES  
NATIONAL UNIVERSITY OF SINGAPORE

2024

Thesis Advisor:

Associate Professor Dimitris G. Angelakis

Examiners:

Professor Gong Jiangbin  
Assistant Professor Patrick Rebentrost

# Declaration

I hereby declare that this thesis is my original work and it has been entirely written by me. I also duly acknowledge all the sources of information which have been used in the thesis. This thesis has also not been submitted for any degree in any university previously.

---

Chee Chong Hian

1 November 2024

# Acknowledgements

In the pursuit of knowledge, no endeavour is truly ever solitary. The completion of this thesis reflects not only my individual effort but also the collective support, guidance, and wisdom of many individuals, both seen and unseen. For this reason, I would like to express my appreciation to these wonderful people.

First and foremost, I extend my deepest gratitude to my advisor, Dimitris Angelakis, who provided me with the opportunity to pursue my research interests at the Centre for Quantum Technologies (CQT) in the National University of Singapore under his supervision. His ability to convey complex ideas to diverse audiences with clarity and flair has greatly inspired me and enhanced my presentation approach. I believe these skills will form a critical foundation for my future career.

Secondly, I am sincerely grateful to Daniel Leykam, for his invaluable guidance and expertise in topological photonics. He has displayed strong dedication to scientific rigour by providing constructive feedback to sharpen my scientific arguments, and showering kind encouragement to push me and the boundaries of my research. I deeply appreciate his contributions to my academic growth and the completion of my research endeavour.

## Acknowledgements

---

Thirdly, I would like to give my deepest appreciation to Adrian Matthew Mak from A\*STAR for his kind mentorship and expertise in computational chemistry. His generosity and patience in providing essential chemical knowledge and technical assistance have challenged me to consider new perspectives and innovative methods, greatly enriching my overall research experience. I am truly thankful for the impact he has had on my research projects.

Fourth, I would like to thank my collaborators for their invaluable scientific input and contributions to this thesis, as well as for their collaborative spirit that has enriched my academic experience. My gratitude also extends to my peers and colleagues within and outside CQT for their cherished friendships. The camaraderie and mutual support within this academic community have been a constant source of motivation. A heartfelt thanks goes to my family and friends, whose unwavering faith in my abilities have given me the strength to overcome the challenges that accompany my academic journey. Their encouragement has been the solid ground which I have stood on throughout this process. Special thanks also go to the examiners, whose insightful comments have been instrumental in improving this thesis. Additionally, I would like to acknowledge the dedicated CQT staff for providing essential administrative and logistical support, making CQT a conducive research environment.

Finally, I acknowledge the contributions of the countless scholars and thinkers whose work has laid the groundwork for my own. The ideas and concepts that have influenced my research are a testament to the vast and interconnected landscape of human thought, within which my work is but a small contribution. To all who have played a role in this journey, whether directly or indirectly, your influence is woven into the fabric of this work, and for that, I offer my sincerest thanks.

# Contents

<b>Declaration</b>	<b>i</b>
<b>Acknowledgements</b>	<b>ii</b>
<b>Summary</b>	<b>viii</b>
<b>Author Publications</b>	<b>ix</b>
<b>List of Figures</b>	<b>xii</b>
<b>List of Tables</b>	<b>xiii</b>
<b>1 Introduction</b>	<b>1</b>
1.1 Quantum Computers . . . . .	3
1.2 Quantum Chemistry . . . . .	5
1.3 Quantum Computational Chemistry . . . . .	8
1.4 Scope and Thesis Outline . . . . .	12
<b>2 Background</b>	<b>15</b>
2.1 Electronic Structure Problem . . . . .	16

2.2	One-electron Wavefunction and Slater Determinant . . . . .	19
2.3	Hartree-Fock Theory . . . . .	22
2.4	Exact Electronic Wavefunction and Correlation Energy . . . . .	26
2.5	Qubit Representation of Electronic Wavefunction . . . . .	28
<b>3</b>	<b>Variational Quantum Algorithm for Estimating Correlation Energies using Perturbation Theory</b>	<b>31</b>
3.1	Introduction . . . . .	31
3.2	Quantum Computational Techniques for Electronic Structure . . . . .	34
3.2.1	Hartree-Fock Method and Unitary Orbital Rotation . . . . .	34
3.2.2	Post Hartree-Fock Methods . . . . .	40
3.2.3	Hamiltonian Factorization for Efficient Energy Measurements . . . . .	44
3.3	Variational Quantum Algorithm using Perturbation Theory . . . . .	47
3.3.1	Idea: Perturbing Hamiltonian then Optimizing Orbitals . . . . .	47
3.3.2	Estimating Correlation Energy Using Linear Depth Quantum Circuits . . . . .	49
3.3.3	Examples and Results . . . . .	55
3.4	Discussion and Conclusion . . . . .	70
<b>4</b>	<b>Shallow Circuits for Efficient Correlated State Preparation</b>	<b>73</b>
4.1	Introduction . . . . .	73
4.2	Preparing Fermionic Wavefunctions Efficiently . . . . .	77
4.2.1	Slater determinants . . . . .	77
4.2.2	Idea: Linear Combinations of Anti-Commuting Operators . . . . .	78
4.2.3	Extension to Correlated States . . . . .	82
4.2.4	Resource Analysis . . . . .	85

4.2.5	Example and Results . . . . .	88
4.3	Summary and Outlook . . . . .	88
<b>5</b>	<b>Resource-Efficient Quantum-Assisted Simulation for Quantum Dynamics</b>	<b>91</b>
5.1	Introduction . . . . .	91
5.2	Existing Approaches for Quantum Time-Propagation . . . . .	94
5.2.1	Hamiltonian Simulation . . . . .	94
5.2.2	Variational Quantum Simulator . . . . .	95
5.2.3	Quantum-Assisted Simulator . . . . .	97
5.3	Resource-Efficient Quantum-Assisted Simulation . . . . .	102
5.3.1	Idea: Linear Combinations of Time-Evolved States . . . . .	102
5.3.2	Resource Analysis . . . . .	104
5.3.3	Examples and Results . . . . .	106
5.4	Discussion and Outlook . . . . .	110
<b>6</b>	<b>Conclusion</b>	<b>113</b>
6.1	Research Summary . . . . .	113
6.2	Emerging Directions and Future Research . . . . .	116
	<b>References</b>	<b>119</b>
<b>A</b>	<b>Shallow Circuits for Efficient Correlated State Preparation</b>	<b>151</b>
A.1	Proof of Equivalence between Two Definitions of an Arbitrary Slater Determinant	151
A.2	Proof of Anti-Commutation Relations . . . . .	155
A.3	Slater Determinant and $L$ -wise Correlated Ansatz using Givens Rotations . . . .	156
A.4	Givens Rotation Gate Decomposition for the $L$ -wise Correlated Ansatz State . .	160

<b>B Resource-Efficient Quantum-Assisted Simulator</b>	<b>162</b>
B.1 Modified Hadamard Test for Parallel Gates . . . . .	162
B.2 Quantum Resource-Efficient Regime . . . . .	164
B.3 Sampling Basis State Overlaps, Hamiltonian and Observable Elements. . . . .	167
B.4 Energy Dynamics of Helium Atom and Hydrogen Molecule . . . . .	168
B.5 Variance of Observed Quantities against Number of Shots . . . . .	170
B.5.1 Helium Atom Case . . . . .	171
B.5.2 Hydrogen Molecule Case . . . . .	172
B.6 First Order Trotterized Time-Evolved Basis States . . . . .	173
B.7 Linear Dependence of the Time-Evolved Basis . . . . .	174

# Summary

Quantum computers promise to simulate chemical systems more efficiently than traditional numerical methods by avoiding the exponential computational complexity these numerical approaches encounter. However, existing quantum algorithms impose heavy demands on both quantum and classical computation, exceeding the current technological capabilities of quantum hardware and hindering their full potential. This thesis aims to address some of these challenges by proposing three resource-efficient quantum algorithms, targeting key problems in quantum chemistry, including ground state energy estimation, quantum state preparation and quantum dynamics. The proposed algorithms introduce new concepts and novel techniques that leverage existing quantum algorithms and numerical methods to optimize resource usage. Specific examples include variational perturbation methods that allow quantum computers to estimate correlation energies using mean-field quantum states, techniques for efficiently preparing fermionic states with specific many-body interactions, and innovative adaptations of quantum time-propagation algorithms for efficient estimation of dynamical quantities. Implemented on both numerical simulations and current quantum hardware, these proposed quantum algorithms demonstrate practical applicability and offer a foundation for future algorithmic innovations in quantum chemistry.

# Author Publications

The current thesis is based on the following manuscripts and publications:

- [1] C. H. Chee, A. M. Mak, D. Leykam, P. K. Barkoutsos, and D. G. Angelakis, “Computing electronic correlation energies using linear depth quantum circuits”, *Quantum Sci. Technol.* **9**, 025003 (2024).
- [2] C. H. Chee, D. Leykam, A. M. Mak, and D. G. Angelakis, “Shallow quantum circuits for efficient preparation of Slater determinants and correlated states on a quantum computer”, *Phys. Rev. A* **108**, 022416 (2023).
- [3] C. H. Chee, D. Leykam, A. M. Mak, K. Bharti, and D. G. Angelakis, *Resource-Efficient Hybrid Quantum-Classical Simulation Algorithm*, 2024, [arXiv:2405.10528](https://arxiv.org/abs/2405.10528).

# List of Figures

1.1	An illustrative overview of this thesis. . . . .	2
1.2	Minimum number of qubits required to simulate various chemical systems. . . . .	8
2.1	Diagrammatic model of Hydrogen molecule $H_2$ . . . . .	17
2.2	Probability density plots of atomic orbitals. . . . .	21
3.1	Standard quantum gate decomposition of a unitary orbital rotation operator. . . . .	36
3.2	QR decomposition of a unitary orbital rotation matrix. . . . .	38
3.3	QR quantum gate decomposition of unitary orbital rotation operator. . . . .	39
3.4	Quantum gate decomposition of 4-mode unitary orbital rotation matrix. . . . .	40
3.5	NISQ-OMP2 algorithm for ground state energy estimation. . . . .	50
3.6	Quantum circuits for NISQ-OMP2 algorithm. . . . .	54
3.7	Quantum gate symbols. . . . .	55
3.8	Molecular orbital diagrams of various molecules for NISQ-OMP2 demonstration. . . . .	56
3.9	CNOT gate depth comparison between NISQ-OMP2 and UCCSD-based approach. . . . .	58
3.10	Orbital-optimized MP2 energy for various molecules at various bond distances on a classically-emulated NISQ computer. . . . .	64

3.11	Orbital-optimized first and second order perturbation energies for various molecules at various bond distances on a classically-emulated NISQ computer. . . . .	66
3.12	Orbital-optimized MP2 energy for Hydrogen molecule at various bond distances on cloud-provided NISQ computer. . . . .	67
3.13	Orbital-optimized first and second order perturbation energies for Hydrogen molecule at various bond distances on cloud-provided NISQ computer. . . . .	69
4.1	Comparison of two approaches of preparing Slater determinants on a quantum computer: fermionic basis rotation and Clifford loaders via Givens rotations . . . . .	75
4.2	Quantum gate decomposition of Clifford loader via Givens rotations. . . . .	79
4.3	Example of 8-qubit Givens rotation angle decomposition. . . . .	80
4.4	Replacement of CNOT ladder by a logarithmic-depth CNOT circuit. . . . .	82
4.5	Quantum gate decomposition of $L$ -wise correlated Clifford loader. . . . .	85
4.6	Two-qubit gate depth per occupied mode estimation of preparing Slater determinant and correlated states using Clifford loaders. . . . .	87
4.7	Fraction of electronic correlation energy of Hydrogen chains captured using Clifford loaders. . . . .	89
5.1	Standard method of simulating quantum dynamics. . . . .	92
5.2	Quantum-Assisted Simulator (QAS) for efficient quantum dynamics simulation. . . . .	103
5.3	Atomic orbital population dynamics of Helium atom using QAS. . . . .	108
5.4	Molecular orbital population dynamics of Hydrogen molecule using QAS. . . . .	109
A.1	Quantum gate decomposition of pairwise correlated Givens rotation gate. . . . .	161
B.1	Standard Hadamard Test. . . . .	162

B.2	Modified Hadamard test with two ancilla qubits for maximising gate parallelism.	163
B.3	Quantum circuit preparation of $N$ -qubit Greenberger–Horne–Zeilinger (GHZ) state.	164
B.4	Hadamard test for estimating real and complex parts of overlap and Pauli elements.	167
B.5	Energy dynamics for Helium atom. . . . .	168
B.6	Energy dynamics for Hydrogen molecule. . . . .	170
B.7	Atomic orbital population variance of the independent QAS samples runs for Helium Atom. . . . .	171
B.8	Energy variance of the independent QAS samples runs for Helium Atom. . . . .	171
B.9	Molecular orbital population variance of the independent QAS samples runs for Hydrogen molecule. . . . .	172
B.10	Energy variance of the independent QAS samples runs for Hydrogen molecule. . . . .	172
B.11	State infidelity of the trotterized QAS-simulated wavefunction. . . . .	173

# List of Tables

1.1	Basic quantum computational chemistry algorithms. . . . .	10
3.1	Quantum resource estimates of NISQ-OMP2 against UCCSD-based approach. . .	57
3.2	Optimized variational parameters for NISQ-OMP2 demonstration. . . . .	59
3.3	Qubit-averaged noise parameters of cloud-provided NISQ computers. . . . .	61
3.4	Average post-selected fraction and state fidelities of NISQ-OMP2 implemented on a classically-emulated NISQ computer for various molecules. . . . .	62
3.5	Average post-selected fraction and state fidelities of NISQ-OMP2 implemented on various cloud-accessed quantum processors for Hydrogen molecule. . . . .	63
B.1	Quantum gate complexity of various algorithms simulating $e^{-i\hat{H}t}$ . . . . .	165

# Chapter 1

## Introduction

Quantum mechanics lies at the foundation of all modern chemistry, but we have yet to efficiently use it to accurately predict chemical properties of compounds. As Dirac noted, atoms or molecules containing more than one electron have resulted in equations too complicated to be solved by analytical means [1]. The advent of modern computers allows these equations to be numerically solved up to a desired precision, given sufficient resources [2]. However, the computational complexity of simulating such chemical systems scales exponentially with system size, limiting the efficient simulation of quantum mechanics to small chemical systems [3, 4].

Quantum computers hold promise for solving complex many-body problems in quantum chemistry more efficiently than classical computers. This potential is driven by two core motivations. First, the size of the quantum computer required to store the wavefunction of a chemical system can be shown to scale at most linearly with the chemical system size. Thus, quantum computing overcomes the problem of requiring exponential amounts of classical storage in ordinary computers [5, 6]. Second, quantum algorithms have been shown to provide a provable

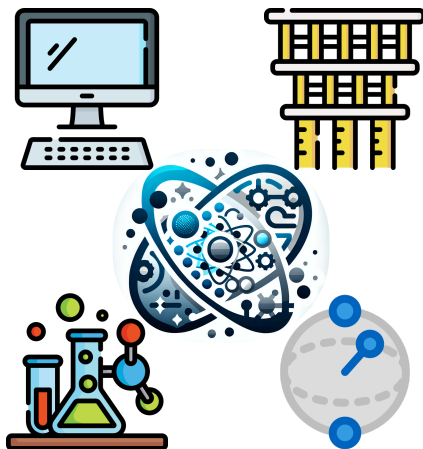


Figure 1.1: An illustrative overview of this thesis, highlighting the elements of classical and quantum computing, quantum physics and chemistry. Central to the graphic is an amalgamation symbolizing the synergistic interplay among these disciplines in the development of quantum algorithms for quantum chemistry applications, the core focus of this thesis. Corners: Flaticon.com, Center: DALL-E 3, *A smooth, quantum mechanical intelligence icon*, easy-peasy.ai.

exponential speedup in performing quantum time evolution over its classical counterparts [7–10]. These motivations foster confidence in quantum computing to overcome the limitations of classical computers, enabling potential applications in solving many-body problems in quantum chemistry [11]. As a result, many quantum algorithms have recently emerged as alternatives to traditional computational chemistry methods, aiming to efficiently solve quantum dynamics and eigen-structure of chemical systems [12–16].

Before discussing the development of quantum algorithms for quantum chemistry, this chapter provides an overview of this thesis in four sections. Section 1.1 summarizes the current technological capabilities of quantum computers. Section 1.2 briefly introduces fundamental computational problems and traditional tools in quantum chemistry. Section 1.3 reviews development of quantum algorithms in solving the quantum dynamics and eigen-structure of chemical systems. Finally, Section 1.4 details the scope and outline of this thesis, setting the stage for my research work. Fig 1.1 illustrates the core elements of this thesis.

## 1.1 Quantum Computers

Between the 1980s and 1990s, there was an emerging radical idea of developing a specialized and controllable quantum system, or a quantum computer, to simulate other kinds of quantum systems [7, 17–19]. Inspired by the discovery of quantum algorithms offering speedups not only in quantum simulation [8–10], but also in prime factorization [20], database search [21], and solving linear equations [22], there has been a long-standing effort to create a fully operational quantum computer [23–26]. Quantum computers can be broadly classified into analogue and digital types. An analogue quantum computer is a special-purpose quantum system that accurately simulates specific quantum models, such as the Ising or Hubbard models, through precise control of its natural quantum evolution [10, 18, 27, 28]. Conversely, a digital quantum computer implements arbitrary operations using a universal set of well-engineered quantum operations, quantum gates, that can simulate various quantum systems and run arbitrary quantum algorithms [8, 29]. So far, analogue quantum computers have had limited applications in quantum chemistry due to engineering challenges in simulating Coulomb interactions [30–32]. This thesis shall describe work done using digital quantum computers, which provides greater suitability in simulating arbitrary chemical systems [33, 34]. The term ‘digital’ will be omitted henceforth for brevity unless clarity necessitates its use.

Since the early 1990s, many quantum computing hardware systems have emerged with a strong focus on scalable platforms capable of controlling hundreds of qubits and beyond. These platforms includes utilizing superconducting circuits [35, 36], trapped ions [37, 38], neutral atoms [39–41], silicon [42, 43], photonics [44–48] as physical implementation of qubits. To protect the quantum information against noise, numerous Quantum Error Correction (QEC) methods have been devised to detect and correct phase and bit-flip qubit errors using multiple

sets of entangled physical qubits [49–53]. A Fault-Tolerant Quantum Computing (FTQC) [54] device featuring a full implementation of QEC would enable the implementation of any quantum circuit with arbitrary quantum gate depth [55–57].

In recent years, rapid development in quantum hardware has culminated in several intermediate-scale demonstrations of QEC using superconducting circuit [58, 59], neutral-atom [60], trapped-ion [61] and silicon [62] platforms. Although these demonstrations have shown promising scaling capabilities to have more error-corrected qubits and gates, however, it remains a challenging engineering endeavor to build a large-scale practical quantum computer [63].

Quantum computers without any implementation of QEC are known as Noisy Intermediate-Scale Quantum (NISQ) devices [64]. They are highly susceptible to quantum noise from their external environment leading to decoherence or the loss of quantum information. To mitigate the effects of quantum noise, two primary strategies are available [65–67]. The first strategy focuses on minimising the usage of noisy quantum resources. This includes reducing the number of qubits needed by exploiting system symmetries [68–70], decreasing the number of noisy quantum measurements by grouping observables into sets of commuting observables [71–78] or employing the method of classical shadows [79–81], and minimizing the number of noisy quantum gates and gate depth through efficient quantum circuit compilation techniques tailored to specific quantum platforms [82–86]. The second strategy involves mitigating quantum errors by recovering the noiseless results from the noisy measurement data via classical post-processing [87–89].

## 1.2 Quantum Chemistry

Quantum chemistry is the study of chemical systems that models atoms and molecules as a collection of nuclei and electrons within the framework of quantum mechanics. Its goal is to accurately calculate and predict chemical properties, such as equilibrium geometries, reaction energies, vibrational frequencies, reaction rates, solubility, acidity or basicity, just to name a few, without relying on empirical measurements. To achieve this, one needs to solve for quantum time-evolution of the wavefunction of the chemical system  $|\Psi(t)\rangle$  which is governed by the non-relativistic Time-Dependent Schrödinger Equation (TDSE),

$$i \partial_t |\Psi(t)\rangle = \hat{H}_m |\Psi(t)\rangle, \quad (1.1)$$

where  $\hat{H}_m$  is the Hamiltonian of the chemical system, with atomic units  $\hbar = 1$  used throughout this thesis. Then, any property of the chemical system can be calculated as a dynamical expectation value  $\langle \Psi(t) | \hat{O} | \Psi(t) \rangle$  of a corresponding observable  $\hat{O}$  representing the quantity of interest.

There are generally two main approaches to solving TDSE. The first approach involves propagating the wavefunction in time from an initial state. This approach encompasses various numerical methods including those that approximate the formal solution  $e^{-i\hat{H}t} |\Psi(0)\rangle$  [90] and those that transform the TDSE into a soluble system of linear equations or coupled linear Ordinary Differential Equations (ODE) via finite difference approximation [91–94]. As well as perturbation methods [95], time-dependent variational methods [96–99] and time-dependent variational Monte Carlo [100, 101]. While the first approach is effective for simulating low-dimensional systems in condensed matter, the second approach, which solve for eigenstructure

of the chemical system, is more appealing. It allows for a more comprehensive interrogation of the quantities of interest mentioned earlier. The stationary states or eigenstates  $|\Psi\rangle$  and eigenenergies  $E$  of the chemical system are governed by the Time-Independent Schrödinger Equation (TISE),

$$\hat{H}_m |\Psi\rangle = E |\Psi\rangle, \quad (1.2)$$

The time-evolved solution can then be constructed by taking an appropriate linear combination of the eigenstates.

A widely used approximation to reduce computation complexity in solving TISE of the chemical system is the Born-Oppenheimer (BO) approximation [102]. Based on the observation that the nuclei are much heavier than the electrons, the BO approximation treats the chemical system as a separable system between the nuclei and electrons. As a result, the method of obtaining full chemical eigenstates becomes a two-step process. In the first step, the nuclei are assumed stationary at a fixed set of spatial coordinates and the TISE of electrons is solved to obtain the electronic eigen-energies and eigen-states. This first step is then repeated for different nuclei coordinates that correspond to various spatial configurations of the chemical system. The resulting set of electronic eigen-energies then forms the potential energy surface for the system of nuclei. In the second step, this potential is used in solving the TISE of nuclei which yields the full chemical eigen-solutions.

In quantum chemistry, significant attention is devoted to solving the TISE of electrons, known as the electronic structure problem [13, 15]. This is because the efficiency and accuracy of any chemical simulation hinge on the many-body treatment of electronic system [103]. The incomplete treatment of the instantaneous Coulomb interaction between any two electrons, or

electron correlations, have been attributed to be the largest source of error in all quantum chemical calculations [104, 105]. While many-body methods such as mean-field Hartree-Fock (HF) theory [106], Coupled-Cluster (CC) [107], Configuration Interaction (CI) [108, 109] exist, they often yield inaccurate results due to poor treatment of electronic correlations [110, 111]. For instance, HF theory wrongly predicts that noble gas atoms do not attract each other at any temperature and should not be able to liquefy [112]. Nonetheless, HF theory provides a fundamental starting point to systematically capture electronic correlation through post-HF methods [113].

The most accurate post-HF approach is Full Configuration Interaction (FCI), which exactly represents the electronic wavefunction as a linear combination of all possible excited electronic configurations generated from the HF wavefunction [108]. However, the factorial computational scaling of FCI with the system size renders it computationally intractable except for very small molecular systems. The largest FCI calculation attempted on a classical computer to date is an electronic ground state energy estimation of an isolated propane molecule  $C_3H_8$ , requiring at least 20 terabytes of memory size and 5 days of calculation runtime [114]. In quantum computing terms, modeling the propane electronic wavefunction corresponds to about 46 qubits minimally.

To put this into perspective, the commonly touted “killer” quantum chemistry application for quantum computers requires a minimum of roughly 200 qubits to model the electronic wavefunction of catalytic sites of nitrogenase enzyme [34]. Understanding how nitrogenase converts nitrogen to ammonia is crucial, as it may lead to an improvement in the energy efficiency of fertilizer production which currently consumes 2% of the world’s annual energy supply [115, 116]. Unfortunately, simulating nitrogenase is beyond the reach of classical

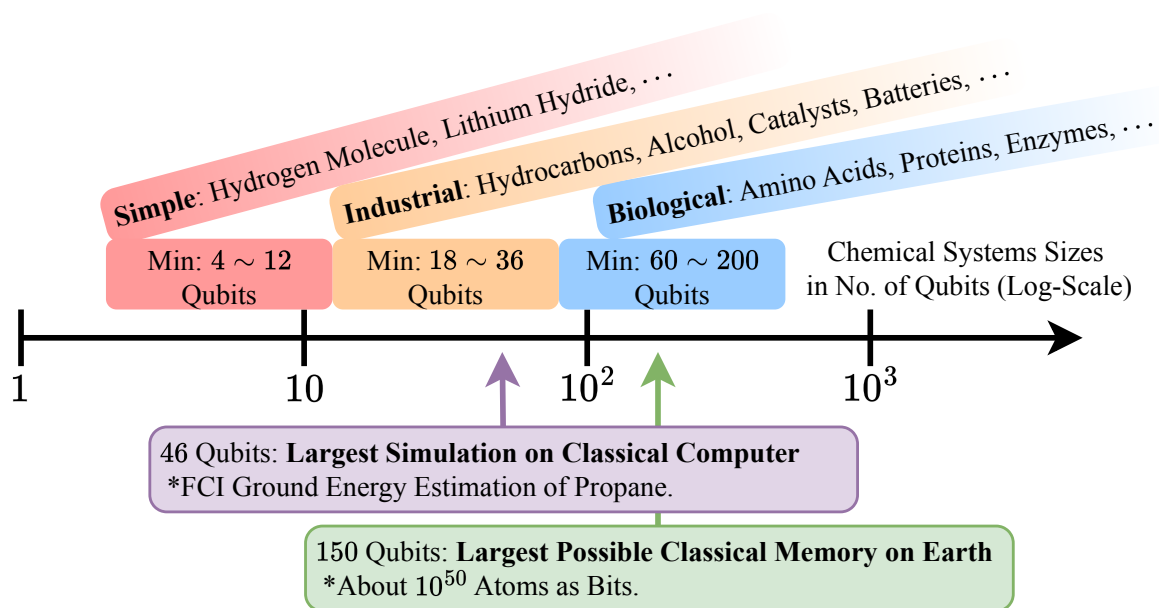


Figure 1.2: The typical minimum range of chemical system sizes of various types, measured in the number of qubits required for quantum computation, assuming minimal basis set and without considering any spatial or spin symmetries. The scale spans from simple chemical systems, to industrial chemicals, and extends to complex biological systems. The largest simulation on a classical computer to date involves estimating the FCI ground state energy of a propane molecule with 46 qubits [114]. The theoretical maximum classical memory capacity on Earth is about 150 qubits, where approximately all  $10^{50}$  atoms are treated as bits.

computing as it exceeds the hard limit of about 150 qubits or roughly  $10^{32}$  terabytes of memory when all  $10^{50}$  atoms available on earth are used as bits for classical memory. Fig 1.2 depicts typical minimum range of chemical system sizes of various types, measured in the number of qubits required for quantum computation.

### 1.3 Quantum Computational Chemistry

Quantum computing promises to overcome the limitations of classical computing by naturally simulating TDSE using Hamiltonian simulation algorithms [8, 10, 117–119]. These algorithms aim to propagate an input wavefunction with a quantum circuit that approximates the quantum time propagator  $e^{-i\hat{H}t}$ . Notable examples of Hamiltonian simulation includes

the Trotter-Suzuki decomposition [8, 9, 120–124], Split-Operator method [125–127], linear combination of unitaries [128, 129], quantum walks [130, 131], quantum signal processing [132], qubitization [133]. Thus, Hamiltonian simulation is widely considered to have many practical applications in solving the quantum dynamics of complex many-body systems in physics and chemistry [13–16], such as simulating fermion or electron dynamics [134, 135] and chemical reactions [127, 136].

TISE can also be solved on the quantum computer via Quantum Phase Estimation (QPE) [134, 137]. QPE utilizes qubit-controlled versions of the time propagator  $e^{-i\hat{H}t}$  from Hamiltonian simulation algorithms and inverse quantum Fourier transformation to estimate the eigen-phases  $e^{2\pi i \theta_j}$  with high probability, offering an exponential speedup in estimating eigen-energies compared to its classical counterparts [29]. Therefore, QPE is useful for predicting electronic structure of chemical system, with broad applications in quantum chemistry [138]. However, QPE relies on a quantum state preparation subroutine that reliably generates good quantum ansatz with high overlaps with the corresponding eigenstate  $|j\rangle$  such as Adiabatic State Preparation (ASP) [138–140] and Quantum Imaginary-Time Evolution (QITE) [141]. This requirement represents a significant bottleneck, as generating quantum eigenstates without prior knowledge of their structure is a fundamentally hard problem [4]. This implies that ASP will require deep circuits in the adiabatic limit to obtain accurate solutions [138–140], whereas QITE will require a substantial number of measurements [141], thereby negating the exponential speedups provided by QPE [142]. Additionally, both QPE and Hamiltonian simulation algorithms assume the use of a FTQC device, as the quantum circuit depth grows polynomially with system size, requiring QEC to ensure accurate results. Thus, these algorithms are currently unsuitable for NISQ devices, even for modest sized molecules [143].

	<b>For Solving Quantum Time-Evolution</b>	<b>For Solving Eigenvalues / Eigenstates</b>
<b>Requires FTQC Devices</b>	Hamiltonian Simulation	Quantum Phase Estimation (QPE)
<b>Suitable for NISQ Devices</b>	Variational Quantum Simulator (VQS)	Variational Quantum Eigensolver (VQE)

Table 1.1: Basic quantum algorithms for general quantum computational chemistry tasks.

Major efforts in developing NISQ-friendly algorithms for quantum chemistry have largely relied on a hybrid quantum-classical framework [144]. This approach flexibly allocates computation between quantum and classical computers, leveraging various NISQ strategies to minimize noise effects. Variational Quantum Algorithms (VQA) represent a popular hybrid method, with numerous experimental demonstrations on NISQ devices [88, 145–159]. VQAs generally involve a parameterized quantum ansatz that is easily prepared on a quantum computer, with the ansatz parameters optimized using a classical computer based on variational principles to obtain the desired quantum state. Two prototypical examples of VQAs are Variational Quantum Simulator (VQS) [160–166] and Variational Quantum Eigensolver (VQE) [167, 168]. While VQS aims to approximate the quantum time-evolution solution using quantum dynamical variational principles [96, 97, 117], VQE seeks to approximate the system eigenstate using a variational energy function to estimate the corresponding eigenenergy [144, 167–169]. Tab. 1.1 presents basic quantum algorithms for quantum computational chemistry.

Efficient preparation of high-quality ansatz states is crucial for many-body applications of quantum computing [66, 142]. Widely-used fermionic ansatzes typically fall into two broad classes: hardware-efficient ansatzes and problem-inspired ansatzes. The first class employs hardware-native gates to minimize the quantum circuit depth of the quantum circuit [149], but is

challenging to optimize [170] and may not accurately represent the desired electronic state [169]. The second class incorporates the system’s physics explicitly. For instance, the shallowest problem-inspired ansatz for electronic structure problems to date is the mean-field HF state. This state can be prepared using a linear depth circuit with a linear qubit chain connectivity [171, 172] and has seen successful NISQ demonstrations in evaluating HF energies of hydrogen chains and the diazene cis-trans isomerization barrier [157]. While HF states fail to capture electronic correlation and are efficiently simulatable on classical computers, they serve as useful starting points for preparing classically-intractable correlated electronic ansatzes inspired by post-HF methods in traditional computational chemistry. Examples of post-HF ansatzes include Unitary Coupled Cluster (UCC) [173–178] and Local Unitary Cluster Jastrow (LUCJ) ansatz [179] which are prepared by applying number-conserving multi-electronic excitation operators to an initial reference HF state.

However, problem-inspired correlated ansatzes often require deep entangling circuits that scale polynomially with system size. This exacerbates quantum noise effects and leads to the barren plateaus problem [180, 181] where gradients of the parameter optimization landscape become exponentially flat as problem size increases, making optimization difficult. A popular approach to mitigate this issue is the Adaptive, Problem-Tailored Variational Quantum Eigensolver (ADAPT-VQE) [182]. ADAPT-VQE dynamically grows the ansatz by adding one electronic excitation operator at a time, thereby modifying the parameter landscape to avoid local minimas and vanishing gradients [183]. Despite these advancements, the preparation and optimization of correlated ansatz in VQA remain challenging on NISQ devices due to the need for deep entangling circuits [157, 171–173, 175–178]. As a result, state-of-the-art NISQ demonstrations are limited to shallow problem-inspired circuit ansatzes with fewer than one

hundred qubits [184, 185]. This limitation makes it currently impossible to study chemically-relevant molecular systems, which often require hundreds of qubits and beyond [143, 186].

Moreover, while NISQ strategies that mitigate the effects of quantum noise have enabled many NISQ demonstrations of quantum simulation of simple chemical systems [88, 145–159], scaling them up for larger, chemically-relevant systems may not be feasible with NISQ devices [14, 143]. This infeasibility is often due to the heavy problem approximations and the unsustainable use of classical computing resources undertaken such strategies when mitigating quantum noise, thus compromising simulation accuracy and efficiency. Nevertheless, developing NISQ quantum applications remain crucial, even in the absence of FTQC devices, as they can be valuable in other aspects of quantum chemistry that do not require high simulation accuracy and precision, thereby motivating further research in quantum computational chemistry [187]. For example, recent NISQ demonstrations have shifted focus from exact chemistry calculations to more manageable tasks such as quantum benchmarking using small molecules [154, 188], modeling a chain of hydrogen atoms as half-filled Hubbard chain [189], and calculating upper electronic ground energy bounds of Iron-Sulfur cluster [190]. These approaches accommodate larger chemical systems while working within the limitations of NISQ devices.

## 1.4 Scope and Thesis Outline

This thesis aims to address several quantum computational chemistry challenges for both FTQC and NISQ algorithms by proposing three new quantum algorithms and demonstrate their potential on various electronic chemical systems. Chapter 2 briefly reviews fundamental quantum chemistry concepts and introduces basic methods to represent electronic wavefunctions as qubits and manipulate them to imbue electronic correlations, which will be used throughout

this thesis. The subsequent paragraphs describe the challenges and the proposed algorithms for the subsequent chapters of this thesis.

First, implementing VQA on NISQ devices to estimate electronic correlation energy of chemical systems is challenging due to the need for deep entangling circuits ansatz, where the circuit depth scales polynomially. Chapter 3 proposes a new VQA algorithm, the NISQ Orbital-Optimised Second-order Møller-Plesset Perturbation (NISQ-OMP2), which uses multiple NISQ-friendly linear-depth HF ansatzes to estimate ground state electronic correlation energies via perturbation theory up to the second order. This enables NISQ devices to reproduce equilibrium molecular energies and capture perturbative electronic correlation effects at longer molecular bond distances.

Second, existing problem-inspired correlated ansatzes that aim to capture electronic or fermionic correlations often have deeper circuits than HF ansatzes. Chapter 4 proposes an alternate paradigm for correlated state preparation using Givens rotations, which perform rotations within a two-dimensional fermionic subspace of a larger Hilbert space. This approach provides a shallower, yet scalable approach to prepare correlated states with an overall polylogarithmic two-qubit gate depth scaling in the number of qubits.

Third, despite exponential speedups in quantum time-evolution tasks, there remains a computational bottleneck in extracting desired quantum properties at intermediate time steps due to wavefunction collapse [191] and no-fast-forwarding theorem [9, 192]. Chapter 5 introduces a hybrid quantum-classical simulator, the Resource-Efficient Quantum-Assisted Simulator (QAS), enabling classical computers to leverage FTQC devices to overcome this bottleneck. This approach is more resource-efficient in simulating large systems initialized in

an unknown superposition of a few system eigenstates.

Finally, Chapter 6 concludes this thesis with a summary of the proposed quantum algorithms and their results. Emerging research opportunities in quantum computational chemistry are discussed in light of the rapid progress in quantum computing hardware.

## Chapter 2

# Background

Quantum chemistry explores the behavior of electrons in atoms and molecules through the principles of quantum mechanics. Central to this field are electronic wavefunctions, which describe the probability amplitude distribution of electronic states in a chemical system, and the electronic Hamiltonian, which represent the sum of all energy operators affecting the electrons. To delve deeper into the electronic structure of chemical systems, methods such as Hartree-Fock (HF) and post-HF methods are employed to approximate the electronic wavefunction with various levels of electronic correlation effects. Recently, quantum computing has emerged as a promising tool to tackle these complex problems more efficiently by representing electronic wavefunctions as qubit states. Quantum algorithms can be utilized to simulate time-evolution of electrons and electronic correlations in the electronic wavefunction.

This background chapter has five sections that review the fundamental quantum chemistry concepts and methods. Section 2.1 formally describes the electronic structure problem. Section 2.2 introduces spin-orbitals, which are one-electron wavefunctions used to

construct approximate electronic wavefunctions. Section 2.3 reviews the HF method, which best approximates the electronic wavefunction while neglecting electronic correlations. Section 2.4 discusses the exact form of electronic wavefunction and the correlation energy neglected by the HF method. Finally, Section 2.5 explores techniques for mapping electronic wavefunctions and observables into qubit wavefunctions and Pauli operators for quantum computation.

## 2.1 Electronic Structure Problem

Electrons are the primary focus in the study of atoms and molecules, as the accuracy of any quantum chemical simulation heavily depends on the many-body treatment of electronic interactions. The focus is on solving the Time-Dependent Schrödinger Equation (TDSE) and the Time-Independent Schrödinger Equation (TISE) of the electrons in the chemical system, which will enable the estimation of its quantum dynamic properties.

Atoms and molecules are simply modelled as a system of  $d$  electrons and  $d_{\text{nuc}}$  nuclei. Fine structure effects including relativistic effects, spin-orbit coupling, Lamb shift due to quantization of the electric field, and hyperfine splitting due to proton-electron spin interactions are assumed absent for all discussion in this thesis. Such assumptions are good approximations for light systems up to size of a sodium atom, where fine structure effects have negligible corrections on electronic structure. Using Hartree atomic units, which shall be assumed throughout this thesis, the Planck constant, electron charge, electron mass and the Bohr radius are set to unity,  $\hbar = q_{\text{ele}} = m_{\text{ele}} = a_0 = 1$ . Let  $\hat{\mathbf{r}} = \{\hat{\mathbf{r}}_\mu : \mu = 1, \dots, d\}$  and  $\hat{\mathbf{R}} = \{\hat{\mathbf{R}}_J : J = 1, \dots, d_{\text{nuc}}\}$  be the position operators of the corresponding electrons and nuclei, respectively,  $q_J$  be the  $J^{\text{th}}$  nuclear charge and  $m_{\text{nuc},J}$  be the  $J^{\text{th}}$  nuclear mass. A diagrammatic model of a Hydrogen molecule  $\text{H}_2$  is shown in Fig. 2.1

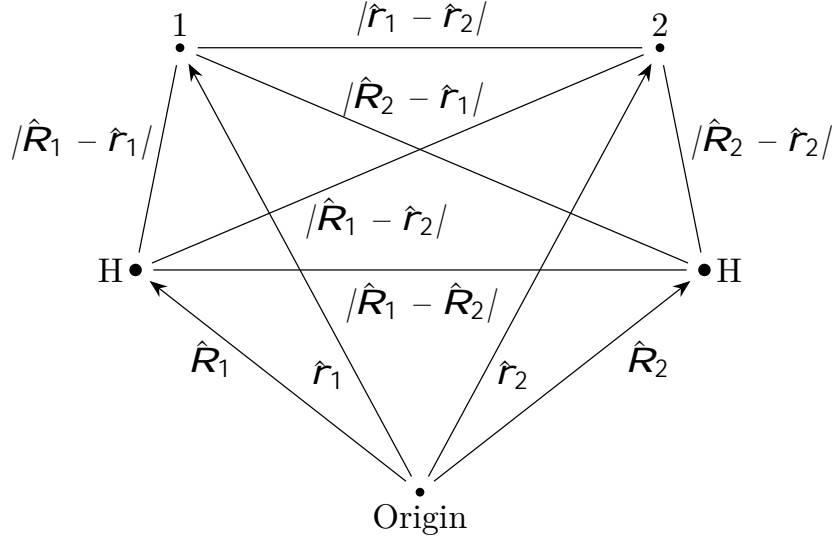


Figure 2.1: Diagrammatic model of Hydrogen molecule  $H_2$  with two protons labelled as “H” and two electrons labelled as “1” and “2”.  $\hat{\mathbf{r}}_1$ ,  $\hat{\mathbf{r}}_2$ ,  $\hat{\mathbf{R}}_1$  and  $\hat{\mathbf{R}}_2$  are the position operators of the corresponding electrons and nuclei.

The atomic/molecular Hamiltonian  $\hat{H}_m(\hat{\mathbf{r}}, \hat{\mathbf{R}})$  is expressed as the sum of the kinetic energy operators of the electrons  $\hat{K}_{\text{ele}}$ , nuclei  $\hat{K}_{\text{nuc}}$  and the Coulomb potential operators between pairs of electrons  $\hat{V}_{\text{e-e}}(\hat{\mathbf{r}})$ , pairs of a electron and a nucleus  $\hat{V}_{\text{e-n}}(\hat{\mathbf{r}}, \hat{\mathbf{R}})$  and pairs of nuclei  $\hat{V}_{\text{n-n}}(\hat{\mathbf{R}})$ , that is

$$\hat{H}_m(\hat{\mathbf{r}}, \hat{\mathbf{R}}) = \hat{K}_{\text{nuc}} + \hat{K}_{\text{ele}} + \hat{V}_{\text{e-e}}(\hat{\mathbf{r}}) + \hat{V}_{\text{e-n}}(\hat{\mathbf{r}}, \hat{\mathbf{R}}) + \hat{V}_{\text{n-n}}(\hat{\mathbf{R}}), \quad (2.1)$$

$$\hat{K}_{\text{nuc}} = - \sum_{J=1}^{d_{\text{nuc}}} \frac{1}{2m_{\text{nuc},J}}, \quad (2.2)$$

$$\hat{K}_{\text{ele}} = - \sum_{\mu=1}^d \frac{1}{2}, \quad (2.3)$$

$$\hat{V}_{\text{e-e}}(\hat{\mathbf{r}}) = \frac{1}{2} \sum_{\mu, \nu=1}^d \frac{1}{|\hat{\mathbf{r}}_\mu - \hat{\mathbf{r}}_\nu|}, \quad (2.4)$$

$$\hat{V}_{\text{e-n}}(\hat{\mathbf{r}}, \hat{\mathbf{R}}) = - \sum_{\mu, J=1}^{d, d_{\text{nuc}}} \frac{q_J}{|\hat{\mathbf{r}}_\mu - \hat{\mathbf{R}}_J|}, \quad (2.5)$$

$$\hat{V}_{\text{n-n}}(\hat{\mathbf{R}}) = \frac{1}{2} \sum_{J, K=1}^{d_{\text{nuc}}} \frac{q_J q_K}{|\hat{\mathbf{R}}_J - \hat{\mathbf{R}}_K|}. \quad (2.6)$$

Simulating both the electrons and nuclei together presents significant challenges. A common approximation to simplify this problem is the Born-Oppenheimer approximation, which enables nuclei and electrons to be treated independently [102]. This approximation is justified by the observation that protons and neutrons are roughly 1800 times heavier than electrons. Thus, in a chemical system with momentum distributed equally among its constituents, the nuclei – which consist of many protons and neutrons – move much slower relative to electrons. Therefore, the atomic/molecular wavefunction  $\psi_m(\hat{\mathbf{r}}, \hat{\mathbf{R}})$  can be approximated as a separable wavefunction, represented as a Kronecker product of the nuclei  $\psi_{\text{nuc}}(\hat{\mathbf{R}})$  and electronic  $\psi_{\text{ele}}(\hat{\mathbf{r}}, \hat{\mathbf{R}})$  wavefunctions,

$$\psi_m(\hat{\mathbf{r}}, \hat{\mathbf{R}}) = \psi_{\text{nuc}}(\hat{\mathbf{R}}) \psi_{\text{ele}}(\hat{\mathbf{r}}, \hat{\mathbf{R}}) . \quad (2.7)$$

As a result, the atomic/molecular Hamiltonian  $\hat{H}_m(\hat{\mathbf{r}}, \hat{\mathbf{R}}) = \hat{K}_{\text{nuc}} + \hat{H}_{\text{ele}}(\hat{\mathbf{r}}, \hat{\mathbf{R}})$  is effectively split into two separate parts: the kinetic energy of the nuclei  $\hat{K}_{\text{nuc}}$  and the electronic Hamiltonian

$$\hat{H}_{\text{ele}}(\hat{\mathbf{r}}, \mathbf{R}) = \hat{K}_{\text{ele}} + \hat{V}_{\text{e-e}}(\hat{\mathbf{r}}) + \hat{V}_{\text{e-n}}(\hat{\mathbf{r}}, \mathbf{R}) + \hat{V}_{\text{n-n}}(\mathbf{R}), \quad (2.8)$$

for a fixed set of nuclear coordinates  $\mathbf{R}$  and the TISE of the chemical system in Eq. (1.2) decouples into two independent eigen-equations, simplifying the simulation of chemical systems,

$$\hat{H}_{\text{ele}}(\hat{\mathbf{r}}, \mathbf{R}) \psi_{\text{ele}}(\hat{\mathbf{r}}, \mathbf{R}) = \epsilon_{\text{ele}}(\mathbf{R}) \psi_{\text{ele}}(\hat{\mathbf{r}}, \mathbf{R}) , \quad (2.9)$$

$$\hat{K}_{\text{nuc}} \psi_{\text{nuc}}(\hat{\mathbf{R}}) = \epsilon_{\text{nuc}}(\hat{\mathbf{R}}) \psi_{\text{nuc}}(\hat{\mathbf{R}}) . \quad (2.10)$$

The problem of finding the electronic eigenstates  $\psi_{\text{ele}}(\hat{\mathbf{r}}, \mathbf{R})$  and eigenenergies  $\epsilon_{\text{ele}}(\mathbf{R})$

in Eq. (2.9) is commonly referred to as the Electronic Structure Problem. In this context, the Coulomb potential between nuclei  $\hat{V}_{n-n}(\mathbf{R})$  in the electronic Hamiltonian  $\hat{H}_{\text{ele}}(\hat{\mathbf{r}}, \mathbf{R})$  effectively becomes a constant value, which can be omitted in actual electronic structure calculations as it only amounts to a constant shift in the final electronic eigenenergies. The solved electronic eigenenergies  $\epsilon_{\text{ele}}(\mathbf{R})$  for various nuclei coordinates  $\mathbf{R}$  form a Potential Energy Surface (PES)  $\epsilon_{\text{ele}}(\hat{\mathbf{R}})$  for the nuclear system. This PES is then used in the TISE of the nuclei to describe the vibrational, rotational and translational eigenmodes of the chemical system. For a rigorous discussion of the Born-Oppenheimer approximation, readers may refer to Sutcliffe [193] and Mayer [194].

## 2.2 One-electron Wavefunction and Slater Determinant

The electronic wavefunction  $\psi_{\text{ele}}(\hat{\mathbf{r}})$  describes the probability amplitude of the electronic states in the chemical system. Typical approaches of describing electronic wavefunction include using position or momentum basis or using the eigen-energy basis of the electronic Hamiltonian. However, these descriptions can be cumbersome and impractical to describe larger, complex chemical systems, especially those lacking spatial symmetries. Instead, the electronic wavefunction is often expressed in terms of spin-orbitals, which are one-electron wavefunctions in quantum chemistry terminology. This approach allows for a systematic manipulation electronic correlations in electron wavefunction, facilitating practical and manageable calculations for chemical systems.

The spin-orbitals  $\psi(\hat{\mathbf{x}})$  can be described as a Kronecker product of the spatial wavefunction  $\psi(\hat{\mathbf{r}})$ , also referred to as the orbital, and the electron spin  $\psi(\hat{s})$ , where the operator  $\hat{\mathbf{x}}$  denotes both the position  $\hat{\mathbf{r}}$  and spin- $\frac{1}{2}$   $\hat{s}$  operators of an electron. Let

$\rho, q, r, s \in \{1, \dots, N\}$  be the indices denoting generic spin-orbitals

$$\begin{aligned} \chi_{\rho}(\hat{\mathbf{x}}) &= \begin{cases} \chi_{\rho}(\hat{\mathbf{r}}) \chi_{\rho}(\hat{\sigma}) & \text{even } \rho, \\ \chi_{\rho}(\hat{\mathbf{r}}) \chi_{\rho}(\hat{\sigma}) & \text{odd } \rho, \end{cases} \end{aligned} \quad (2.11)$$

These spin-orbitals  $\chi_{\rho}(\hat{\mathbf{x}})$  are always assumed normalised but are generally not orthogonal, that is their inner product  $\langle \chi_{\rho} | \chi_q \rangle$  is described as follows,

$$\begin{aligned} \langle \chi_{\rho} | \chi_q \rangle &= 1 \quad \rho = q, \\ 0 < \langle \chi_{\rho} | \chi_q \rangle < 1 & \rho \neq q, \end{aligned} \quad (2.12)$$

where the position-spin operator  $\hat{\mathbf{x}}$  has been dropped for brevity.

The orbitals  $\chi_{\rho}(\hat{\mathbf{r}})$  used to describe a single electron in an atom or a molecule are referred to as atomic and molecular orbitals, respectively. Atomic orbitals, as illustrated in Fig 2.2, are typically expressed as a separable product of the spherical and radial wavefunctions. The wavefunction separability is possible due to spherical symmetry of the attractive nuclear potential and the absence of electronic interactions. The spherical part is composed of linear combinations of spherical harmonics special functions which generates the standard “s, p, d, f” sub-shells in chemistry. The radial part consists of linear combinations of parameterized analytical functions, such as Hydrogenic, Slater [195] or Gaussian-type functions [196]. Considerable efforts in early days of quantum chemistry were dedicated to developing useful atomic orbitals sets for various elements, basis sets sizes and purposes. These sets are now readily available for advanced quantum chemistry calculations [186]. Readers interested in techniques used to develop these atomic orbitals may refer to Helgaker et al. [197].

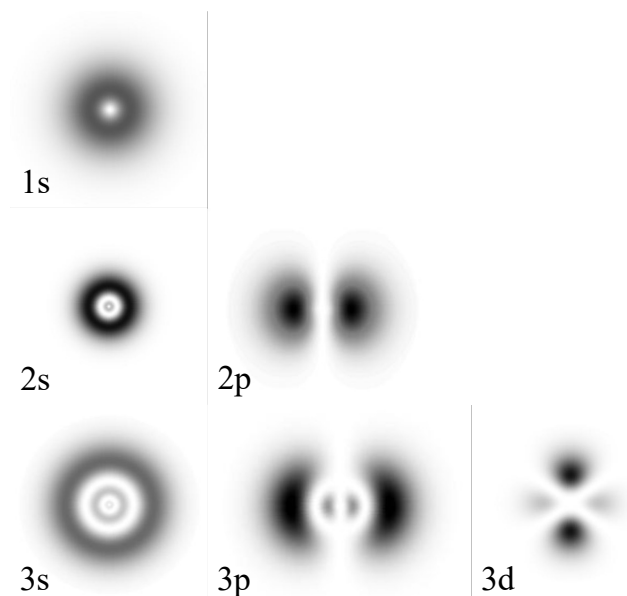


Figure 2.2: Probability density plots of atomic orbitals up to the third principal quantum number. Darker regions indicate higher probability of finding an electron and vice versa. Orbitals: BotRejectsInc, *Mathematical plots of hydrogen atomic orbitals*, cronodon.com, 2023.

Compared to atomic orbitals, molecular orbitals are relatively more challenging to describe because the quantum problem of an electron in three or more attractive nuclear potentials has no analytical solution. Thus, molecular orbitals are approximated as Linear Combination of Atomic Orbitals (LCAO). Given an atomic basis set  $\{|\psi_p^A\rangle : p = 1, 2, \dots, S\}$  of size  $S$ , a set of molecular orbitals  $\{|\psi_q^M\rangle : q = 1, \dots, N\}$  of size  $N$  can be constructed as follows,

$$|\psi_q^M\rangle = \sum_{p=1}^S C_{pq} |\psi_p^A\rangle, \quad (2.13)$$

where  $C_{pq}$  are the LCAO coefficients to be determined.

Electrons are indistinguishable particles, thus the electronic wavefunction  $\psi_{\text{ele}}$  obeys electron exchange symmetry, where the electronic probability density function  $|\psi_{\text{ele}}|^2$  remains invariant under the exchange of the spatial and spin coordinates of any two electrons. According

to the spin-statistic theorem, which shows that half-integer spin particles are fermions with anti-symmetric wavefunctions under particle exchange. This means that electronic wavefunction changes sign upon the exchange of two electrons. This leads to the Pauli-Exclusion Principle (PEP) that maintains the anti-symmetric nature of the electronic wavefunction that are expressed in terms of spin-orbitals. PEP states that no two electrons with the same spin state can occupy the same orbital state simultaneously.

For example, the simplest electronic wavefunction that describes a system of non-interacting electrons, which satisfies PEP, is an anti-symmetrized Kronecker product of  $d$ -occupied out of the  $N$  spin-orbitals, known as the Slater determinant / SD [198],

$$\begin{aligned} \psi_{\text{SD}} &= \frac{1}{d!} \begin{vmatrix} \phi_1(\hat{\mathbf{x}}_1) & \cdots & \phi_d(\hat{\mathbf{x}}_1) \\ \vdots & \ddots & \vdots \\ \phi_1(\hat{\mathbf{x}}_d) & \cdots & \phi_d(\hat{\mathbf{x}}_d) \end{vmatrix} \end{aligned} \quad (2.14)$$

$$= \frac{1}{d!} \begin{vmatrix} d & & & & \\ & d-1 & & & \\ & & \ddots & & \\ & & & 2 & \\ & & & & 1 \end{vmatrix} \quad (2.15)$$

## 2.3 Hartree-Fock Theory

Hartree-Fock (HF) theory is a fundamental method in quantum chemistry and often serves as the first step towards more accurate methods that capture electronic correlations. It aims to optimise all  $N$  spin-orbitals such that the corresponding Slater determinant is the most dominant in a desired exact electronic eigenstate [199]. While HF methods for approximating excited eigenstate exist [200], this section will focus on the traditional HF method for electronic ground state.

The HF method aims to variationally optimize a set of spin-orbitals  $\{|\rho\rangle : \rho = 1, \dots, N\}$  such that the  $d$  spin-orbitals with the lowest energy form a Slater determinant  $|\text{SD}\rangle$  as in Eq. (2.15). This optimization minimizes the expectation value of the electronic Hamiltonian  $\langle \text{SD} | \hat{H}_{\text{ele}} | \text{SD} \rangle$ , subject to the orthonormality constraints on the chosen spin-orbitals. The minimum expectation value achieved and the corresponding single Slater determinant are referred to as the Hartree-Fock energy  $E_{\text{HF}}$  and the reference Hartree-Fock ground state  $|\phi_0\rangle$ , respectively.

The expectation value  $\langle \text{SD} | \hat{H}_{\text{ele}} | \text{SD} \rangle$  can be compactly written in terms of the spin-orbitals using Slater-Condon rules [198, 201] that express integrals in the coefficients of one and two-body operators using an orthonormal set of spin-orbitals,

$$\langle \text{SD} | \hat{H}_{\text{ele}} | \text{SD} \rangle = E^H + E^J + E^K, \quad (2.16)$$

where  $E^H$  is the core energy that contains kinetic and attractive Coulombic nuclear potential energy, mainly described by the one-electron core integral  $h_q^p$ ,

$$E^H = \sum_{j \text{ occ}} h_j^j, \quad (2.17)$$

$$h_q^p = \int d\hat{\mathbf{r}} \rho_p(\hat{\mathbf{r}}) \left[ -\frac{1}{2} \nabla^2 - \sum_{J=1}^{d_{\text{nuc}}} \frac{q_J}{|\mathbf{R}_J - \hat{\mathbf{r}}|} \right] \rho_q(\hat{\mathbf{r}}). \quad (2.18)$$

with indices  $i, j$  denoting occupied orbitals.  $E^J$  is the Coulombic repulsion potential energy between two electrons occupying two spin-orbitals.  $E^K$  is the electron exchange energy correction to Coulombic repulsion due to the anti-symmetry of the electronic wavefunction.

Both  $E^J$  and  $E^K$  contain the two-electron repulsion integral  $h_{rs}^{pq}$ ,

$$E^J = \frac{1}{2} \sum_{i,j \text{ occ}} h_{ij}^{ij}, \quad (2.19)$$

$$E^K = -\frac{1}{2} \sum_{i,j \text{ occ}} h_{ji}^{ij}, \quad (2.20)$$

$$h_{rs}^{pq} = \int d\hat{\mathbf{r}} d\hat{\mathbf{r}}' \rho_p(\hat{\mathbf{r}}) \rho_r(\hat{\mathbf{r}}') \frac{1}{|\hat{\mathbf{r}} - \hat{\mathbf{r}}'|} q(\hat{\mathbf{r}}) s(\hat{\mathbf{r}}'). \quad (2.21)$$

Using the method of Lagrange multipliers, consider the following Lagrangian  $L$  with varying spin-orbitals  $\rho = \rho + \rho'$ ,

$$L = \langle \text{SD} | \hat{H}_{\text{ele}} | \text{SD} \rangle - \sum_{i,j \text{ occ}} \lambda_{ij} (\langle i | j \rangle - \delta_{ij}), \quad (2.22)$$

where the orthonormality constraint on the spin-orbitals is imposed in the second term. Setting the first variation in the Lagrangian in Eq. (2.22) to zero,

$$L = 0, \quad (2.23)$$

yields the condition for optimization. However, the solution to Eq. (2.23) is not unique, as there is a degree of flexibility in the spin-orbitals. There exist mixtures of spin-orbitals up to a unitary transformation which do not change the energy of the Slater determinant  $\langle \text{SD} | \hat{H}_{\text{ele}} | \text{SD} \rangle$ . By allowing both unitary and orthogonal transformation on all  $N$  spin-orbitals, a unique set of transformed spin-orbitals can be found. As such, Eq. (2.23) results in the following canonical Hartree-Fock eigenvalue equation

$$\hat{F} | \rho(\hat{\mathbf{x}}) \rangle = \epsilon | \rho(\hat{\mathbf{x}}) \rangle, \quad (2.24)$$

where the Lagrange multiplier matrix becomes diagonal with eigenvalues  $\epsilon_p$ , which are the optimized orbital energies corresponding to the optimized transformed spin-orbitals  $\phi_p(\hat{\mathbf{x}})$ .  $\hat{F}$  is an effective one-electron Hamiltonian, also called the Fock operator. The Fock operator  $\hat{F}$  can then be expressed as the sum of the core operator  $\hat{h}_{\text{core}}$  and the Hartree-Fock potential operator  $\hat{V}_{\text{HF}}$ ,

$$\hat{F} = \hat{h}_{\text{core}} + \hat{V}_{\text{HF}}, \quad (2.25)$$

where  $\hat{h}_{\text{core}}$  represents the sum of kinetic and nuclear potential operator of each electron and  $\hat{V}_{\text{HF}}$  represents the averaged Coulombic potential of all other electrons or a mean-field of all electronic interaction experienced by each electron, that is,

$$\hat{h}_{\text{core}} = -\frac{1}{2} \nabla^2 - \sum_{J=1}^{d_{\text{nuc}}} \frac{q_J}{|\hat{\mathbf{r}} - \mathbf{R}_J|}, \quad (2.26)$$

$$\hat{V}_{\text{HF}} = \sum_{j \text{ occ}} \int d\hat{\mathbf{r}}_j \frac{1 - \hat{P}_{\hat{\mathbf{x}}, \hat{\mathbf{x}}}}{|\hat{\mathbf{r}} - \hat{\mathbf{r}}_j|}. \quad (2.27)$$

where  $\hat{P}_{\hat{\mathbf{x}}, \hat{\mathbf{x}}}$  is an exchange operator that swaps the spatial and spin coordinates of any two electrons.

The Hartree-Fock potential  $\hat{V}_{\text{HF}}$  depends on the occupied spin-orbitals that need to be determined, making the Hartree-Fock equation in Eq. (2.24) a non-linear eigenvalue equation. There are generally two approaches to solving the Hartree-Fock equation. The traditional approach is an iterative method known as the Self-Consistent-Field (SCF) method [202]. The second approach forgoes the method of Lagrange multipliers and instead implements a unitary transformation on an initial orthonormal set of spin-orbitals to directly minimize the expectation value and find the Hartree-Fock energy [202, 203]. While the direct minimization approach appears straightforward and provides mathematical guarantees of convergence to extremal

points, the traditional SCF method is usually preferred in practice. There exist efficient SCF methods that can quickly converge to a good solution in many practical cases given a good initial guess for the spin-orbitals, often guided by chemist’s intuition [204–207]. As such, the direct minimization approach is typically employed as a last resort for complex electronic structures where SCF methods generally fail.

## 2.4 Exact Electronic Wavefunction and Correlation Energy

Slater determinants serve as the basis for the exact description of the electronic wavefunction. To obtain a complete orthonormal set of Slater determinants  $\{ | \rho \rangle \}$ , one starts with the reference Hartree-Fock ground state  $| 0 \rangle$ . Recall that  $| 0 \rangle$  is a Slater determinant formed by  $d$ -occupied spin-orbitals with the lowest orbital energies that is obtained using the Hartree-Fock method discussed in Section 2.3. Then, one generates new Slater determinants by systematically replacing the occupied spin-orbitals in  $| 0 \rangle$  with any remaining unoccupied or virtual spin-orbitals. The generated Slater determinants are called excited determinants as the replacement of occupied spin-orbitals with virtual ones is analogous to electron excitation. They can be grouped based on the number of spin-orbitals replaced: singly-excited  $| j^a \rangle$ , doubly-excited  $| ij^{ab} \rangle$ , and so forth, where indices  $a, b$  denote virtual orbitals. Using these Slater determinants as basis, the exact electronic wavefunction  $| \text{ele} \rangle$  can be expressed as follows,

$$| \text{ele} \rangle = c_0 | 0 \rangle + \sum_{\substack{j \text{ occ,} \\ a \text{ vir}}} c_j^a | j^a \rangle + \sum_{\substack{i < j \text{ occ,} \\ a < b \text{ vir}}} c_{ij}^{ab} | ij^{ab} \rangle + \dots \quad (2.28)$$

Since each Slater determinant is defined by the “configuration” of the spin-orbitals it consists of, this approach of constructing the exact electronic wavefunction  $| \text{ele} \rangle$  using various Slater determinants as a basis is known as Configuration Interaction (CI) [109].

Correspondingly, the Hamiltonian operator can be discretized into a Hamiltonian matrix  $\mathbf{H}$  with elements  $\langle p | \hat{H}_{\text{ele}} | q \rangle$ , where  $| p \rangle = | 0 \rangle, | j^a \rangle, | ij^{ab} \rangle, \dots$ . Suppose the Hamiltonian matrix  $\mathbf{H}$  is diagonalized such that it yields the electronic eigenenergies, the difference between the exact ground electronic energy  $E_0$  and the Hartree-Fock energy  $E_{\text{HF}}$  is known as the correlation energy

$$E_{\text{corr}} = E_0 - E_{\text{HF}}, \quad (2.29)$$

which represents the energy due to the electronic correlation neglected by the Hartree-Fock method. As the spin-orbitals set size  $N$  is finite, both the exact ground electronic energy  $E_0$  and the Hartree-Fock energy  $E_{\text{HF}}$  values can only be approximated, with a larger  $N$  generally leading to a better approximation of the correlation energy  $E_{\text{corr}}$ .

In the CI approach, there are a total of  $\binom{N}{d}$  possible Slater determinants for a basis. If all Slater determinants are considered in the CI approach, it is referred to as Full CI (FCI) and the corresponding correlation energy  $E_{\text{corr}}$  calculation will be the best possible approximation to the exact electronic correlation for the corresponding spin-orbitals set. However, since the total number of Slater determinants scales exponentially with the number of spin-orbitals  $N$ , both the classical computational runtime and memory requirements for the FCI approach to estimate the correlation energy  $E_{\text{corr}}$  also scales exponentially. As a result, only a tiny fraction out of the  $\binom{N}{d}$  determinants can be considered within resource limitations, restricting accurate studies of large atoms and molecules.

## 2.5 Qubit Representation of Electronic Wavefunction

Quantum computing provides an alternative to classical computing by physically manipulating wavefunctions of multiple qubits to generate desired quantum states for measurement. However, qubits are distinguishable quantum systems with two-definite energy levels, which differ from electrons that are indistinguishable particles with spin and position coordinates. Therefore, it is necessary to map an electronic wavefunction and its observables to the wavefunction of multiple qubits and Pauli operators for quantum computation.

Before various mapping techniques can be described, the electronic wavefunction must first be re-expressed in a suitable form that can be algebraically manipulated similarly to how qubit wavefunctions are manipulated using Pauli operators. This can be accomplished using the second quantization formalism, where creation  $\hat{a}_p^\dagger$  and annihilation  $\hat{a}_p$  operators with the following anti-commuting relations

$$\{\hat{a}_p^\dagger, \hat{a}_q^\dagger\} = \{\hat{a}_p, \hat{a}_q\} = 0, \quad (2.30)$$

$$\{\hat{a}_p^\dagger, \hat{a}_q\} = \delta_{pq}. \quad (2.31)$$

are defined to act on arbitrary Slater determinants to create and annihilate spin-orbitals  $|p\rangle$ , respectively. For example, the reference Hartree-Fock ground state  $|0\rangle$  can be obtained by applying the corresponding creation operators onto a fermionic vacuum state  $|\text{vac}\rangle$  that contains no electrons,

$$|0\rangle = \prod_{j \text{ occ}} \hat{a}_j^\dagger |\text{vac}\rangle, \quad (2.32)$$

The singly-excited  $|j^a\rangle$  and doubly-excited  $|ij^{ab}\rangle$  determinants can also be obtained by applying one-body  $\hat{a}_p^\dagger \hat{a}_q$  and two-body  $\hat{a}_p^\dagger \hat{a}_q^\dagger \hat{a}_r \hat{a}_s$  fermionic operators to the reference Hartree-Fock ground

state  $|0\rangle$ , respectively,

$$|j^a\rangle = \hat{a}_j^\dagger \hat{a}_a |0\rangle, \quad (2.33)$$

$$|ij^{ab}\rangle = \hat{a}_i^\dagger \hat{a}_j^\dagger \hat{a}_a \hat{a}_b |0\rangle. \quad (2.34)$$

In addition, the electronic Hamiltonian  $\hat{H}_{\text{ele}}$  can be expressed using the one and two-body fermionic operators,

$$\hat{H}_{\text{ele}} = \sum_{p,q=1}^N h_q^p \hat{a}_p^\dagger \hat{a}_q + \frac{1}{2} \sum_{p,q,r,s=1}^N h_{rs}^{pq} \hat{a}_p^\dagger \hat{a}_q^\dagger \hat{a}_r \hat{a}_s, \quad (2.35)$$

where  $h_q^p$  and  $h_{rs}^{pq}$  are one-electron core integrals and two-electron repulsion integrals defined in Eq. (2.18) and Eq. (2.21), respectively.

These fermionic operators can be then constructed by the Pauli operators using any desired fermion-to-qubit mapping, thereby enabling the qubit representation of the electronic wavefunction. A popular fermion-to-qubit mapping is the Jordan-Wigner (JW) transformation [5], where the fermionic operators are mapped accordingly as

$$\begin{aligned} \hat{a}_p &= -\frac{1}{2} \prod_{q=1}^{p-1} \hat{Z}_q \quad \hat{X}_p + i\hat{Y}_p, \\ \hat{a}_p^\dagger &= -\frac{1}{2} \prod_{q=1}^{p-1} \hat{Z}_q \quad \hat{X}_p - i\hat{Y}_p, \end{aligned} \quad (2.36)$$

where  $\hat{Z}_p, \hat{X}_p, \hat{Y}_p$  are Pauli operators acting on the  $p^{\text{th}}$  qubit. As a result, the electronic Hamiltonian  $\hat{H}_{\text{ele}}$  transforms into a Pauli Hamiltonian

$$\hat{H}_p = \epsilon_0 + \sum_{\substack{p=1 \\ \{Z,X,Y\}}} \hat{\sigma}_p + \sum_{\substack{p,q=1 \\ \{Z,X,Y\}}} \hat{\sigma}_p \hat{\sigma}_q + \dots \quad (2.37)$$

where  $\hat{\rho} = \{\hat{Z}_\rho, \hat{X}_\rho, \hat{Y}_\rho\}$ .

Intuitively, JW transformation allows each qubit to represent the occupancy level of a spin-orbital, with the  $p^{\text{th}}$  Pauli-Z eigenstates  $|0_p\rangle$  and  $|1_p\rangle$  representing the unoccupied and occupied  $p^{\text{th}}$  spin-orbital, respectively. As a result, each computational basis state can roughly correspond to a Slater determinant, which is advantageous for quantum computational chemistry. [15, 16]. A disadvantage of JW is that parallel fermionic operators may no longer be implemented in concurrently on a quantum circuit, increasing circuit depth. This disadvantage is due to the extensive strings of Pauli-Z operators in the JW mapping that serve to maintain the parity of the fermionic operator. Alternative fermion-to-qubit mappings such as Parity and Bravyi-Kitaev [6, 208] aim to minimize the length of these Pauli strings, which can help reduce circuit depth of the fermionic operators [209]. However, these alternatives sacrifice the intuitive representation, as the computational basis will no longer directly correspond to a Slater determinant, which makes manipulating correlation difficult. Therefore, JW mapping will be used throughout this thesis in the interest of clarity.

## Chapter 3

# Variational Quantum Algorithm for Estimating Correlation Energies using Perturbation Theory

This chapter adapts the material published in:

- C. H. Chee, A. M. Mak, D. Leykam, P. K. Barkoutsos, and D. G. Angelakis, “Computing electronic correlation energies using linear depth quantum circuits”, [Quantum Sci. Technol.](#) **9**, 025003 (2024).

### 3.1 Introduction

The efficient computation of molecular energies is an exciting application of quantum computing for quantum chemistry. A popular quantum algorithm is the Variational Quantum Eigensolver

(VQE) algorithm, which aims to prepare a quantum circuit ansatz that minimizes a variational function dependent on a set of predefined ansatz parameters [167, 168]. State-of-the-art VQE algorithms use deep entangling quantum circuit ansatzes to accurately represent electronic wavefunctions and capture electronic correlations.

However, current quantum computers are susceptible to quantum noise and decoherence, thus they are known as Noisy Intermediate-Scale Quantum (NISQ) devices. This restricts many NISQ demonstrations of VQE algorithms to small, hardware-efficient quantum circuits, limiting their application to small molecules [145, 147, 149, 157]. Scaling up these successful NISQ demonstrations to larger molecular systems presents significant challenges. Firstly, capturing the electronic correlations in wavefunctions often requires deep and entangling quantum circuits. Such circuits have two-qubit gate depths that typically scale polynomially with  $N$  the number of qubits representing the molecular system, making them prohibitive on NISQ devices [173, 175]. Secondly, the number of classical parameters required to accurately estimate electronic correlation energies can be massive, complicating the ansatz optimization process. Thirdly, the number of non-commuting observables that need to be measured to estimate molecular energies scales quartically  $O(N^4)$  with system size, rendering quantum measurements highly impractical for sizeable molecules [14]. Although recent advances have aimed at mitigating these issues by reducing the number of ansatz parameters [178, 182] and measurements needed for energy estimation [210, 211], NISQ implementations of VQE still suffer from quantum noise, which affects the accuracy of electronic correlation energy estimations for larger molecular systems.

To overcome these challenges, this chapter proposes a novel NISQ-friendly algorithm that variationally estimates the ground electronic correlation energy perturbatively up to the second order. This approach employs multiple shallow parameterized Hartree-Fock (HF) states,

with quantum circuit depth scaling linearly with the number of qubits, and is locally optimized using a classical optimizer. The algorithm will be demonstrated on various small molecules, using both numerical simulations with incorporated quantum noise models and commercially available cloud NISQ devices. The results show that NISQ devices have the potential to accurately reproduce equilibrium molecular energies and capture the perturbative electronic correlation effects at longer bond distances. Although total number of shallow circuits required for the proposed NISQ-friendly algorithm scales  $O(N^5)$ , they can be implemented in parallel on many NISQ devices available on cloud platforms. In addition, the use of shallow circuits facilitates the study of larger molecular systems compared to other alternative variational quantum approaches, where deep quantum circuit depth required would typically exceed the constraints of NISQ devices.

Before detailing the proposed approach, several basic quantum computational techniques useful for solving the electronic structure of chemical systems will be introduced and reviewed. Section 3.2.1 describes the Hartree-Fock Method implemented on a quantum computer using unitary orbital rotation operators. Section 3.2.2 describes various quantum computational Post Hartree-Fock methods including the Full Configuration Interaction, Unitary Coupled Cluster and Many-Body Perturbation Theory. Lastly, Section 3.2.3 describes a method of efficient estimating electronic energy on a quantum computer. Techniques introduced in this section will be useful for the NISQ-friendly algorithm proposed in this chapter.

## 3.2 Quantum Computational Techniques for Electronic Structure

### 3.2.1 Hartree-Fock Method and Unitary Orbital Rotation

The HF wavefunction, introduced in Section 2.3, is a single Slater determinant approximation to an electronic wavefunction. The HF method optimises the HF wavefunction to best approximate an exact eigenstate of the electronic system. For instance, the reference HF ground state  $|0\rangle$  in Eq. (2.32) is a single Slater determinant approximation to the exact ground state. Using the Jordan-Wigner (JW) fermion-to-qubit mapping described in Section 2.5, the reference HF ground state  $|0\rangle$  with  $N$  optimized molecular orbitals and  $d$  electrons can be prepared on a quantum computer with  $N$  qubits initialized in the zero state  $|0\rangle$  as,

$$|0\rangle = \prod_{j=1}^d \frac{1}{2} \left( \sum_{q=1}^{j-1} \hat{Z}_q + \hat{X}_j - i\hat{Y}_j \right) |0\rangle \quad (3.1)$$

$$\prod_{j=1}^d \hat{X}_j |0\rangle, \quad (3.2)$$

where  $\approx$  denotes equality up to an overall unobserved global phase. The Pauli-Z eigenstates of each qubit represents the occupation of the optimized molecular orbitals, and the qubit number is ordered by their respective orbital energies, starting with the lowest.

This representation is flexible; using any other set of molecular orbitals would not change the qubit state in Eq. (3.2), as long as consistency is maintained throughout the computation. This flexibility is useful in quantum computational chemistry, where the initial set of orthonormal molecular orbitals may not be optimized. If so, an orbital optimization can

be performed on the HF wavefunction  $|\Psi_{\text{HF}}\rangle$  that minimizes the total electronic energy,

$$|\Psi_{\text{HF}}\rangle = \hat{U}(\boldsymbol{\theta})|\Psi_0\rangle \quad \text{s.t.} \quad \min_{\boldsymbol{\theta}} \langle \Psi_{\text{HF}} | \hat{H}_{\text{elec}} | \Psi_{\text{HF}} \rangle, \quad (3.3)$$

using a general unitary orbital rotation  $\hat{U}(\boldsymbol{\theta})$  for a complex skew-Hermitian parameter matrix

$$\boldsymbol{\theta} = -\boldsymbol{\theta}^\dagger,$$

$$\hat{U}(\boldsymbol{\theta}) = \exp \sum_{p,q=1}^N \theta_{pq} \hat{a}_p^\dagger \hat{a}_q. \quad (3.4)$$

This generates singly-excited determinants in the electronic wavefunction, which according to the Brillouin's theorem, do not contribute to electronic correlation [199]. This approach is similar to the direct minimization from the numerical HF methods described in Section 2.3.

The shallowest quantum gate decomposition of unitary orbital rotation  $\hat{U}(\boldsymbol{\theta})$  consists of  $N + 1$  layers of single and two-qubit gates,

$$\hat{U}(\boldsymbol{\theta}) = \prod_{p=1}^N \prod_{\text{odd}, r=1}^N \hat{P}_r(\theta_r^{(p)}) \hat{P}_{r+1}(\theta_{r+1}^{(p)}) \hat{U}_{r+1}^r(\theta_{r,r+1}^{(p)}) \prod_{q=1}^N \hat{P}_q(\theta_q^{(0)}), \quad (3.5)$$

as shown in Fig. 3.1, with real rotation angles  $\theta_{r,q}^{(p)}$  and  $\theta_r^{(p)}$ . The quantum gates are the single-qubit phase gates  $\hat{P}_r(\theta_r)$  that act on the  $r^{\text{th}}$  qubit, with the following matrix representation in computational basis  $\{|0\rangle, |1\rangle\}$

$$\hat{P}_r(\theta_r) = \begin{pmatrix} 1 & 0 \\ 0 & \exp(i\theta_r) \end{pmatrix}, \quad (3.6)$$

and the general fermionic single-excitation rotation gates  $\hat{U}_q^p(\theta_{pq})$ , that act on all qubits between  $p$  and  $q$  including the  $p^{\text{th}}$  and  $q^{\text{th}}$  qubits, represent a simple rotation mixture of the  $p^{\text{th}}$  and  $q^{\text{th}}$

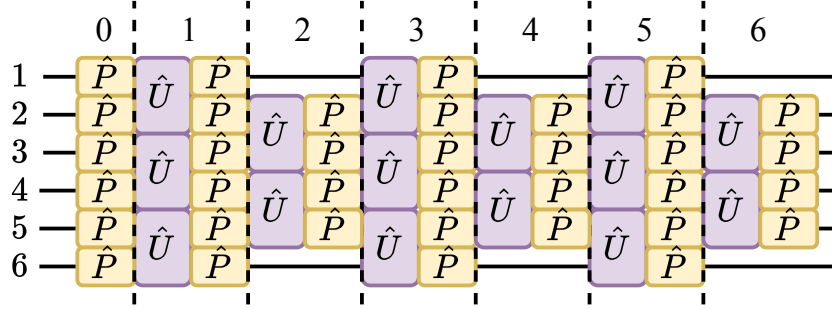


Figure 3.1: Standard quantum gate decomposition of a 6-qubit example of unitary orbital rotation  $\hat{U}(\ )$  in Eq. (3.4). Gate qubit labels and the angles are omitted to improve readability. Yellow  $\hat{P}$  and purple  $\hat{U}$  gates refers to the single-qubit phase gate and two-qubit neighbouring fermionic single-excitation rotation gate in Eqs. (3.6) and (3.8), respectively. Numbers on the left and top of the circuit are the qubit and gate layer indexes, respectively.

molecular orbitals,

$$\hat{U}_q^p(\ ) = \exp \left[ \sum_{r=q+1}^{p-1} \hat{a}_p^\dagger \hat{a}_q - \hat{a}_q^\dagger \hat{a}_p \right] \quad (3.7)$$

$$= \exp \left[ -i \frac{\rho q}{2} \sum_{r=q+1}^{p-1} \hat{X}_p \hat{Y}_q - \hat{Y}_p \hat{X}_q \right] \hat{Z}_r \quad (3.8)$$

If the skew-Hermitian parameter matrix  $\rho$  in the unitary orbital rotation  $\hat{U}(\ )$  were to be real-valued, then the phase gates  $\hat{P}$  would be redundant as there would be no complex values, allowing them to be removed from the quantum gate decomposition of the unitary orbital rotation in Fig. 3.1.

The shallow gate decomposition of  $\hat{U}(\ )$  in Eq. (3.5) follows from the optimal QR decomposition of its 2D matrix form  $\mathbf{U} = \exp(\ )$  represented in the fermionic single-excitation basis  $\hat{a}_p^\dagger \hat{a}_q$ . It decomposes  $\mathbf{U}$  into a unique product of neighbouring complex Givens rotation matrices  $\mathbf{G}(\ \rho_{r,r+1}, \ \theta_{r, \ r+1} )$  from linear algebra,

$$\mathbf{G}(\theta_{r,r+1}, \phi_{r,r+1}) = \begin{pmatrix} \exp(i\theta_r) \cos(\theta_{r,r+1}) & -\exp(i\theta_{r+1}) \sin(\theta_{r,r+1}) \\ \exp(i\theta_r) \sin(\theta_{r,r+1}) & \exp(i\theta_{r+1}) \cos(\theta_{r,r+1}) \end{pmatrix} \quad (3.9)$$

$$= \begin{pmatrix} \cos(\theta_{r,r+1}) & -\sin(\theta_{r,r+1}) & \exp(i\theta_r) & 0 \\ \sin(\theta_{r,r+1}) & \cos(\theta_{r,r+1}) & 0 & \exp(i\theta_{r+1}) \end{pmatrix}. \quad (3.10)$$

This can be recognized as a quantum gate sequence  $\hat{G}(\theta_{r,r+1}, \phi_{r,r+1})$  that represents a complex Givens rotation  $\mathbf{G}(\theta_{r,r+1}, \phi_{r,r+1})$  in the fermionic single-excitation basis,

$$\hat{G}(\theta_{r,r+1}, \phi_{r,r+1}) = \hat{U}_{r+1}^r(\theta_{r,r+1}) \hat{P}_r(\phi_r) \hat{P}_{r+1}(\phi_{r+1}). \quad (3.11)$$

Applying  $\hat{G}(\theta_{r,r+1}, \phi_{r,r+1})$  on the left of  $\hat{U}(\theta)$  effectively performs a Givens rotation  $\mathbf{G}$  that mixes the  $r^{\text{th}}$  and  $r+1^{\text{th}}$  rows of matrix  $\mathbf{U}$ . Similarly, applying  $\hat{G}^\dagger$  on the right of  $\hat{U}(\theta)$  effectively performs a conjugate-transposed Givens rotation  $\mathbf{G}^\dagger$  that mixes the  $r^{\text{th}}$  and  $r+1^{\text{th}}$  columns of  $\mathbf{U}$ . Thus, by carefully zeroing out the lower triangle elements of  $\mathbf{U}$  in a zig-zag manner as shown in Fig. 3.2, and alternating between mixing rows and columns for each diagonal line, until the  $\hat{U}(\theta)$  eventually diagonalizes. This results in a sequence of multiple  $\hat{G}$ s which represents an inverse gate decomposition of  $\hat{U}(\theta)$  as shown in Eq. (3.5).

The QR decomposition starts by zeroing out the bottom-left most element  $U_{N,1}$  by mixing the 1<sup>st</sup> and 2<sup>nd</sup> columns with a conjugated-transposed Givens rotation  $\mathbf{G}^\dagger$  with angles  $\theta_{1,2} = \tan^{-1} \frac{|U_{N,1}|}{|U_{N,2}|}$ ,  $\phi_1 = -\arg(U_{N,1})$  and  $\phi_2 = -\arg(U_{N,2})$ . This corresponds to applying  $\hat{P}_1^\dagger(-\arg(U_{N,1}))$ ,  $\hat{P}_2^\dagger(-\arg(U_{N,2}))$  and  $\hat{U}_2^{1,\dagger} \tan^{-1} \frac{|U_{N,1}|}{|U_{N,2}|}$  on the right of  $\hat{U}(\theta)$  in order.

Next, move up to the next element  $U_{N-1,1}$ . Note that this element is different from the initial value as it was mixed by other elements in the previous step. We zero out this element

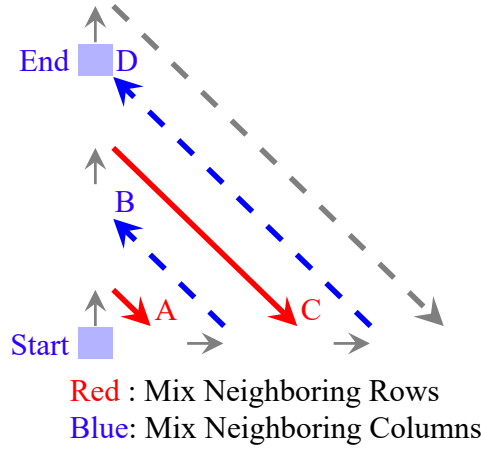


Figure 3.2: The optimal QR decomposition zig-zag route of zeroing elements along the diagonal lines A,B,C,D of the 6-qubit unitary orbital rotation matrix  $\mathbf{U}$  in the fermionic single-excitation basis  $\hat{a}_p^\dagger \hat{a}_q$ .

$U_{N-1,1}$  by mixing the  $N-1^{\text{th}}$  and  $N-2^{\text{th}}$  rows with the Given rotation  $\mathbf{G}$  with angles  $\theta_{N-2,N-1} = \tan^{-1} \frac{|U_{N-1,1}|}{|U_{N-2,1}|}$ ,  $\theta_{N-2} = -\arg(U_{N-2,1})$  and  $\theta_{N-1} = -\arg(U_{N-1,1})$ . This corresponds to applying  $\hat{P}_{N-1}(-\arg(U_{N-1,1}))$ ,  $\hat{P}_{N-2}(-\arg(U_{N-2,1}))$ ,  $\hat{U}_{N-1}^{N-2} \tan^{-1} \frac{|U_{N-1,1}|}{|U_{N-2,1}|}$  on the left of  $\hat{U}$  in order.

Then, repeat the steps above for all matrix elements along the zig-zag path, alternating mixing of the row and column for every diagonal line, until all the lower triangle matrix elements of  $\mathbf{U}$  are zeroed out. In the end, operator  $\hat{U}(\ )$  and corresponding matrix  $\mathbf{U}$  become a complex diagonal matrix with a unit magnitude, which can be represented as a single layer of phase gates, and the QR decomposition is complete. Finally, the gate decomposition of the unitary orbital rotation in Eq. (3.5) is obtained by unravelling the gate sequence in order, which results in the quantum circuit shown in Fig. 3.3.

As a simple example, consider a 4-mode complex unitary orbital rotation  $\hat{U}(\ )$  such that the  $\mathbf{U}$  matrix in the fermionic operator basis  $\hat{a}_p^\dagger \hat{a}_q$  happens to be a  $4 \times 4$  normalized Hadamard matrix,

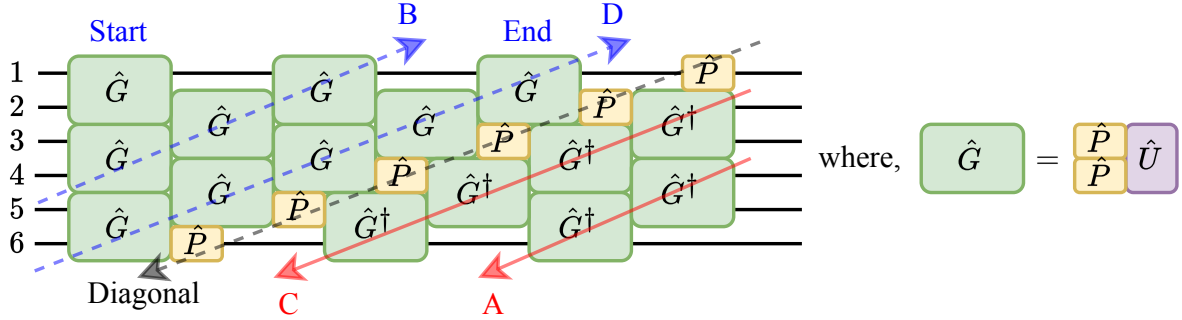


Figure 3.3: Quantum gate decomposition of a 6-qubit unitary orbital rotation operator  $\hat{U}(\ )$  after QR decomposition as shown in Fig. 3.2. Green  $\hat{G}$  gate represents the quantum gate sequence given in Eq. (3.11). Note that this quantum circuit is exactly equivalent to that in Fig. 3.1.

$$\mathbf{U} = \frac{1}{2} \begin{pmatrix} 1 & 1 & 1 & 1 \\ 1 & -1 & 1 & -1 \\ 1 & 1 & -1 & -1 \\ 1 & -1 & -1 & 1 \end{pmatrix}. \quad (3.12)$$

Then, applying the QR decomposition approach described in Section 3.2.1, the unitary orbital rotation can be decomposed into the following quantum circuit as shown in Fig. 3.4.

While the QR decomposition described above yields the shallowest possible circuit with a two-qubit fermionic single-excitation rotation gate depth of exactly  $N$  [212], the amount of classical preprocessing required to obtain the gate rotation angles scales quadratically  $O(N^2)$ . The reason is that every element in the lower triangle of  $\mathbf{U}$  along the aforementioned zig-zag path is zeroed serially, which can be a significant bottleneck if  $N$  is large. This bottleneck can be resolved by adopting a different zeroing route in QR decomposition that allows for parallel Givens rotations, that is by considering mixing only columns or mixing only rows without alternating between them. This alternative approach reduces the classical preprocessing scaling to linear scaling  $O(N)$ , but at the cost of doubling the overall two-qubit fermionic single-excitation rotation gate depth [172, 213]. This method was recently demonstrated on

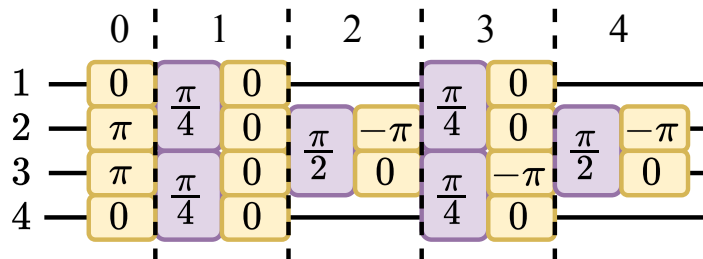


Figure 3.4: Quantum gate decomposition of 4-mode complex unitary orbital rotation matrix in Eq. (3.12). The yellow and purple gates are the phase and fermionic single excitation rotation in Eqs. (3.6) and (3.8), respectively

a superconducting NISQ device to evaluate HF energies of hydrogen chains and the diazene cis-trans isomerization barrier on NISQ hardware [157]. In this proposal, the shallow QR decomposition is preferred for preparing HF states to minimizing the overall gate depth for NISQ computation, thereby minimize the effects of quantum noise.

### 3.2.2 Post Hartree-Fock Methods

#### Full Configuration Interaction

Post Hartree-Fock methods encompass various approaches developed to accurately compute the electronic correlation energy, typically following a HF calculation. As mentioned in Section 2.4, the exact electronic wavefunction can be represented as a linear combination of all possible excited electron configurations generated from the HF wavefunction, referred to as Full Configuration Interaction (FCI). The FCI wavefunction  $|\Psi_{\text{FCI}}\rangle$  can be prepared on a quantum computer by applying specific sequence of fermionic single  $\hat{U}_q^p(\theta)$  and double-excitation gates  $\hat{U}_{rs}^{pq}(\theta)$  are denoted as  $\hat{U}_\mu = \{\hat{U}_q^p, \hat{U}_{rs}^{pq}\}$ ,

$$|\Psi_{\text{FCI}}\rangle = \prod_{\mu=1}^{\binom{N}{d}} \hat{U}_\mu(\theta_\mu) |0\rangle. \quad (3.13)$$

For the proof and construction of the sequence order to parameterize the exact electronic wavefunction, interested readers are referred to [175, 214]. Crucially, the source of electronic correlation lies in the use of the fermionic double-excitation rotation gate

$$\hat{U}_{rs}^{pq}(\theta) = \exp \left[ \theta (\hat{a}_p^\dagger \hat{a}_q^\dagger \hat{a}_r \hat{a}_s - \hat{a}_s^\dagger \hat{a}_r^\dagger \hat{a}_q \hat{a}_p) \right] \quad (3.14)$$

$$\begin{aligned} &= \exp \left[ -i \frac{\theta}{8} (\hat{X}_r \hat{Y}_s \hat{X}_p \hat{X}_q + \hat{Y}_r \hat{X}_s \hat{X}_p \hat{X}_q + \hat{Y}_r \hat{Y}_s \hat{Y}_p \hat{X}_q + \hat{Y}_r \hat{Y}_s \hat{X}_p \hat{Y}_q - \hat{X}_r \hat{X}_s \hat{Y}_p \hat{X}_q \right. \\ &\quad \left. - \hat{X}_r \hat{X}_s \hat{X}_p \hat{Y}_q - \hat{Y}_r \hat{X}_s \hat{Y}_p \hat{Y}_q - \hat{X}_r \hat{Y}_s \hat{Y}_p \hat{Y}_q \right] \prod_{j=r+1}^{s-1} \hat{Z}_j \prod_{k=p+1}^{q-1} \hat{Z}_k, \quad (3.15) \end{aligned}$$

assuming  $1 \leq s < r < p < q \leq N$ , to generate doubly and higher excited determinants in the electronic wavefunction. Unfortunately, the factorial number of fermionic excitation gates in the FCI state Eq. (3.13) is required to exactly represent an electronic wavefunction. Thus, it becomes computationally costly for both quantum and classical devices except for very small molecular systems.

### Unitary Coupled Cluster

An alternative approach is to truncate the sequence in Eq. (3.13) down to a manageable size that is polynomial in the number of qubits, known as the trotterized Unitary Coupled Cluster Singles and Double excitation (UCCSD) approach. The term Coupled Cluster (CC) refers to a numerical post-HF method of solving for electronic eigenstates expressed in an exponential ansatz / CC ,

$$| \text{CC} \rangle = \exp(\hat{T}) | 0 \rangle, \quad (3.16)$$

with a so-called cluster operator  $\hat{T}$ ,

$$\hat{T} = \prod_{k=1}^{n_{\text{exc}}} \hat{T}_k, \quad (3.17)$$

$$\hat{T}_k = \frac{1}{(k!)^2} \sum_{\substack{j_1, j_2, \dots, j_k \\ b_1, b_2, \dots, b_k}} t_{j_1, j_2, \dots, j_k}^{b_1, b_2, \dots, b_k} \hat{a}_{b_1}^\dagger \hat{a}_{b_2}^\dagger \dots \hat{a}_{b_k}^\dagger \hat{a}_{j_k} \dots \hat{a}_{j_2} \hat{a}_{j_1}, \quad (3.18)$$

where  $t_{j_1, j_2, \dots, j_k}^{b_1, b_2, \dots, b_k}$  are amplitude coefficients to be solved, and  $| \text{CC} \rangle$  converges to FCI state  $| \text{FCI} \rangle$  with an increasing number of excitations  $n_{\text{exc}}$  [107].

The Unitary Coupled Cluster (UCC) is a unitary extension of the CC approach, where the ansatz is modified as follows,

$$| \text{UCC} \rangle = \exp(\hat{T} - \hat{T}^\dagger) | 0 \rangle, \quad (3.19)$$

which can be prepared on a quantum computer using the first-order Trotterization approximation. This approximation decomposes  $\exp(\hat{T} - \hat{T}^\dagger)$  into fermionic  $n_{\text{exc}}$ -excitation operators, in a heuristic order, to create a trotterized UCC ansatz. Truncating to single and double-excitation operator produces a trotterized UCCSD ansatz, which requires at least  $O(N^3 \text{ }^5)$  two-qubit gate depth, posing a challenge for implementation on currently NISQ devices [173]. Various strategies have been proposed to reduce overall circuit depth of the trotterized UCCSD ansatz including the use of shallower non-fermionic qubit excitation operators [152, 215] and adaptive generation techniques that builds the ansatz from a pool of excitation operators [182]. However, these heuristic strategies lack a systematic approach to approximate electronic correlation, making it difficult to interpret and predict results for similar chemical systems. Additionally, they often lack rigorous convergence guarantees and quantum resource estimates, making them unreliable for simulating larger chemical systems.

## Many-Body Perturbation Theory

This section demonstrates how the deep, entangling quantum circuits and heuristic methods employed by the UCC ansatz in the previous section can largely be avoided by employing many-body perturbation theory. As first proposed by Møller and Plesset [216–218], the exact ground state energy can be expressed in terms of orders of the HF states and energies, allowing the use HF quantum circuits to estimate correlation energy. Formally, in many-body perturbation theory, the electronic Hamiltonian  $\hat{H}_{\text{ele}}$  in Eq. (2.35) is partitioned into two parts: an unperturbed mean-field Hamiltonian  $\hat{F}$  and the remaining perturbation term, referred to as the correlation operator  $\hat{V}$ ,

$$\hat{H}_{\text{ele}} = \hat{F} + \hat{V}. \quad (3.20)$$

The mean-field Hamiltonian  $\hat{F}$  is second quantization of the Fock operator in Eq. (2.25),

$$\hat{F} = \sum_{p,q=1}^N \sum_{pq} h_{pq} \hat{a}_p^\dagger \hat{a}_q. \quad (3.21)$$

Indices  $p, q$  denote the general molecular orbitals, which are eigenstates of Fock operator obtained after applying the HF method introduced in Section 2.3. The eigenvalues of the Fock operator are the orbital energies

$$\epsilon_p = h_p^p + \sum_{j \text{ occ}} h_{pj}^{jp} - h_{pj}^{pj}, \quad (3.22)$$

where the  $h_q^p$  and  $h_{rs}^{pq}$  are the one-electron core and two-electron repulsion integral from Eqs. (2.18) and (2.21), respectively. Indices  $i, j$  denote the occupied molecular orbitals.

The perturbation expansion for the exact ground state energy up to second order gives

the second-order Møller-Plesset (MP2) energy

$$E_{\text{MP2}} = E^{(0)} + E^{(1)} + E^{(2)}, \quad (3.23)$$

$$E^{(0)} = \langle 0 | \hat{F} | 0 \rangle, \quad (3.24)$$

$$E^{(1)} = \langle 0 | \hat{V} | 0 \rangle, \quad (3.25)$$

$$E^{(2)} = \sum_{a < b, i < j} \frac{\langle 0 | \hat{V} | ij^{ab} \rangle^2}{\epsilon_i + \epsilon_j - \epsilon_a - \epsilon_b}, \quad (3.26)$$

where indices  $a, b$  denote virtual orbitals. The zeroth-order energy  $E^{(0)}$  in Eq. (3.23) is numerically calculated as the sum of all occupied orbital energies  $\epsilon_i$ . The first-order energy  $E^{(1)}$  in Eq. (3.23) is the mean-field electron interaction energy of the reference HF ground state  $|0\rangle$ . The sum of the zeroth and first-order energies constitutes the HF energy. The second-order energy  $E^{(2)}$  in Eq. (3.23) is the first perturbative approximation to the electronic correlation energy, expressed in terms of the off-diagonal elements of the perturbation  $\hat{V}$  with respect to the reference ground  $|0\rangle$  and the doubly-excited  $|ij^{ab}\rangle$  HF states. Third and higher-order perturbative terms can be obtained using higher-order corrected wavefunctions which are, however, more difficult to realize than HF wavefunctions on NISQ devices [219]. Such higher-order terms provide no guarantee of convergent behavior and may yield oscillatory or erratic corrections to the correlation energy [217, 220]. It is notable that other works have used MP2 as a classical pre-processing step for quantum algorithms [144, 169, 174, 176, 221].

### 3.2.3 Hamiltonian Factorization for Efficient Energy Measurements

Measuring the electronic energy of the quantum ansatz is accomplished by estimating the expectation value of the electronic Hamiltonian. However, applying the JW fermion-to-qubit mapping results in  $O(N^4)$  Pauli strings of quantum measurements, making direct energy

estimation impractical beyond the smallest molecules [71]. To resolve this bottleneck, it was proposed to use a low-rank tensor factorized form of the electronic Hamiltonian [222–225] to effectively reduce the  $O(N^4)$  down to  $O(N)$  number of Pauli measurements [210],

$$\hat{H}_{\text{ele}} = \hat{U}^{(0)} \sum_{p=1}^N g_p \hat{n}_p \hat{U}^{\dagger(0)} + \sum_{l=1}^{O(N)} \hat{U}^{(l)} \sum_{p,q=1}^N g_{pq}^{(l)} \hat{n}_p \hat{n}_q \hat{U}^{\dagger(l)}, \quad (3.27)$$

where  $\hat{n}_p = \hat{a}_p^\dagger \hat{a}_p$  are the fermionic number operators and  $\hat{U}^{(l)}$  are the unitary orbital rotations as given in Eq. (3.4). Each summation term in Eq. (3.27) is a linear combination of orbital-transformed number operators  $\hat{U}^{(0)} \hat{n}_p \hat{U}^{\dagger(0)}$  and  $\hat{U}^{(l)} \hat{n}_p \hat{n}_q \hat{U}^{\dagger(l)}$ . Under the JW mapping, the number operators become a linear combination of Pauli-Z strings as  $\hat{n}_p = \frac{1}{2} (1 + \hat{Z}_p)$ . Thus, all number operators within each summation term in Eq. (3.27) can be simultaneously estimated on a quantum computer using a single set of bitstring measurements. This effectively reduces the number of quantum measurements from  $O(N^4)$  to  $O(N)$  and is referred to as the Basis Rotation Grouping scheme [210].

To obtain the low-rank tensor factorized form of electronic Hamiltonian, the electronic Hamiltonian  $\hat{H}_{\text{ele}}$  in Eq. (2.35) needs to be rewritten into the so-called chemist notation,

$$\hat{H}_{\text{ele}} = \sum_{p,q=1}^N T_q^p \hat{a}_p^\dagger \hat{a}_q + \frac{1}{2} \sum_{p,q,r,s=1}^N V_{rs}^{pq} \hat{a}_p^\dagger \hat{a}_q \hat{a}_r^\dagger \hat{a}_s, \quad (3.28)$$

where the fermionic operators are rearranged from  $\hat{a}^\dagger \hat{a}^\dagger \hat{a} \hat{a}$  to  $\hat{a}^\dagger \hat{a} \hat{a}^\dagger \hat{a}$  in the second term. As a result of this reordering of the fermionic operators, the usual one-electron integrals  $h_q^p$  and two-electrons integrals  $h_{rs}^{pq}$  change slightly to become  $T_q^p$  and  $V_{rs}^{pq}$ , respectively. Here, it is assumed

that real orbitals are used, such that  $V_{rs}^{pq}$  possesses an eight-fold permutational symmetry,

$$V_{rs}^{pq} = V_{qp}^{sr} = V_{sr}^{pq} = V_{rs}^{qp} = V_{sr}^{qp} = V_{qp}^{rs} = V_{pq}^{rs} = V_{pq}^{sr}, \quad (3.29)$$

which enable a symmetric factorization of  $V_{rs}^{pq}$  under a Cholesky decomposition [226],

$$V_{rs}^{pq} = \sum_{l=1}^{O(N)} w_l v_{pq}^{(l)} v_{rs}^{(l)}, \quad \text{s.t.} \quad v_{pq}^{(l)} = v_{rs}^{(l)}. \quad (3.30)$$

Thus, the two-body Coulomb term can be rewritten in terms of one-body fermionic terms  $\hat{a}_p^\dagger \hat{a}_q$ ,

$$\frac{1}{2} \sum_{p,q,r,s=1}^N V_{rs}^{pq} \hat{a}_p^\dagger \hat{a}_q \hat{a}_r^\dagger \hat{a}_s = \frac{1}{2} \sum_{l=1}^{O(N)} w_l \sum_{p,q=1}^N v_{pq}^{(l)} \hat{a}_p^\dagger \hat{a}_q. \quad (3.31)$$

Finally, a QR decomposition is performed on the matrices  $T$  and  $v^{(l)}$ , which is akin to performing a unitary orbital rotation  $\hat{U}(\cdot)$  to diagonalize the sum of one-body fermionic terms

$\sum_{p,q=1}^N v_{pq}^{(l)} \hat{a}_p^\dagger \hat{a}_q$  into a diagonal sum of number operators  $\hat{n}_q$ . Thus,

$$\frac{1}{2} \sum_{l=1}^{O(N)} w_l \sum_{p,q=1}^N v_{pq}^{(l)} \hat{a}_p^\dagger \hat{a}_q = \sum_{l=1}^{O(N)} \hat{U}^{(l)} \sum_{p,q=1}^N g_{pq}^{(l)} \hat{n}_p \hat{n}_q \hat{U}^{\dagger (l)}, \quad (3.32)$$

$$\sum_{p,q=1}^N T_q^p \hat{a}_p^\dagger \hat{a}_q = \hat{U}^{(0)} \sum_{p=1}^N g_p \hat{n}_p \hat{U}^{\dagger (0)}, \quad (3.33)$$

where the coefficients  $w_l$  are absorbed into  $g_{pq}^{(l)}$  which contains the diagonalized elements of  $v^{(l)}$ .

Interested readers may refer to [224] for a more detailed derivation.

### 3.3 Variational Quantum Algorithm using Perturbation Theory

#### 3.3.1 Idea: Perturbing Hamiltonian then Optimizing Orbitals

This section proposes a variational NISQ-friendly algorithm for estimating the ground state energy based on minimizing the MP2 energy through the optimization of the molecular orbitals (MO), also known as orbital-optimized MP2 (OMP2) in quantum chemistry parlance [227, 228].

In OMP2, the total MP2 energy becomes parameterized as  $E_{\text{MP2}}(\theta)$  and it is locally minimized by optimizing the molecular orbitals using the unitary orbital rotation  $\hat{U}(\theta)$  in Eq. (3.4) where

$\theta$  is a real-valued anti-Hermitian parameter matrix such that  $\theta_{pq} = -\theta_{qp}^*$ . Applying this orbital transformation to the reference HF ground state  $|0\rangle$  and doubly-excited state  $|ij^{ab}\rangle$  yields,

$$|0(\theta)\rangle = \hat{U}(\theta)|0\rangle, \quad (3.34)$$

$$|ij^{ab}(\theta)\rangle = \hat{U}(\theta)|ij^{ab}\rangle. \quad (3.35)$$

After introducing this orbital transformation to the mean-field Hamiltonian  $\hat{F}$ , it becomes parameterized as,

$$\hat{F}(\theta) = \hat{U}(\theta)\hat{F}\hat{U}^\dagger(\theta). \quad (3.36)$$

Thus, the perturbation term can be written as,

$$\hat{V}(\theta) = \hat{H}_{\text{ele}} - \hat{F}(\theta). \quad (3.37)$$

Inserting these parameters into the MP2 energy  $E_{\text{MP2}}$  in Eq. (3.23) yields the parameterized MP2 energy

$$E_{\text{MP2}}(\boldsymbol{\theta}) = E^{(0)} + E^{(1)}(\boldsymbol{\theta}) + E^{(2)}(\boldsymbol{\theta}), \quad (3.38)$$

$$E^{(0)} = \langle \phi_0(\boldsymbol{\theta}) | \hat{F}(\boldsymbol{\theta}) | \phi_0(\boldsymbol{\theta}) \rangle \quad (3.39)$$

$$= \langle \phi_0 | \hat{F} | \phi_0 \rangle, \quad (3.40)$$

$$E^{(1)}(\boldsymbol{\theta}) = \langle \phi_0(\boldsymbol{\theta}) | \hat{V}(\boldsymbol{\theta}) | \phi_0(\boldsymbol{\theta}) \rangle, \quad (3.41)$$

$$E^{(2)}(\boldsymbol{\theta}) = \sum_{a < b, i < j} \frac{\langle \phi_0(\boldsymbol{\theta}) | \hat{V}(\boldsymbol{\theta}) | \phi_{ij}^{ab}(\boldsymbol{\theta}) \rangle^2}{\epsilon_i + \epsilon_j - \epsilon_a - \epsilon_b}. \quad (3.42)$$

Note that the unitary orbital rotation  $\hat{U}(\boldsymbol{\theta})$  only mixes the eigenstates of the mean-field Hamiltonian  $\hat{F}$  into new ones, while the corresponding orbital energies  $\epsilon_\rho$  remain unaffected. Therefore,  $E^{(0)}$  in Eq. (3.39) is independent of  $\boldsymbol{\theta}$  and is still equal to the sum of all occupied orbital energies  $\epsilon_i$ .

For a general many-body system, a truncated parameterized perturbation energy expansion is usually not variational, as the parameterization scheme can be arbitrary. As a result, it might lead to an unbounded energy expansion in the parameter domain [229, 230]. Thus, it is typical to optimize the parameterized MP2 energy  $E_{\text{MP2}}(\boldsymbol{\theta})$  based on the principle of least sensitivity [230, 231], where the gradient magnitude  $\|\nabla_{\boldsymbol{\theta}} E_{\text{MP2}}(\boldsymbol{\theta})\|$  is minimized. However, the focus of OMP2 is on the HF solution close to  $\boldsymbol{\theta} = \mathbf{0}$ , where  $\boldsymbol{\theta} = \mathbf{0}$  represents the reference HF ground state  $|\phi_0\rangle$ , which is the global minimum of the unperturbed Hartree-Fock energy. A small correlation energy perturbation transforms the curvature of the energy landscape around  $\boldsymbol{\theta} = \mathbf{0}$  into a local minimum where the minimum point is close to but not at  $\boldsymbol{\theta} = \mathbf{0}$ . As a result, the parameterized MP2 energy  $E_{\text{MP2}}(\boldsymbol{\theta})$  becomes locally variational around

$\mathbf{0}$ . The OMP2 energy  $E_{\text{OMP2}}$  can be obtained by variationally minimizing parameterized MP2 energy  $E_{\text{MP2}}(\mathbf{c})$  with respect to  $\mathbf{c}$  within a small region of radius  $r$  that represents the small perturbative correction to the HF energy due to electronic correlation,

$$E_{\text{OMP2}} = \min [E_{\text{MP2}}(\mathbf{c})] \quad \text{s.t.} \quad \|\mathbf{c}\| \leq r. \quad (3.43)$$

As a result, OMP2 is tractable using local optimization methods such as gradient-descent. In addition, OMP2 also avoids the barren plateaus problem by ignoring the parameter landscape beyond the small region of radius  $r$  about the origin, as the global optimum is not the correct solution.

Indeed, OMP2 computationally scales  $O(N^5)$  on classical computers, and the proposed OMP2 quantum algorithm will thus require the preparation of  $O(N^5)$  parameterized ansatzes with classical pre-processing such as low-rank tensor decomposition and QR matrix decomposition. While the preparation of multiple parameterized ansatzes has been implemented in other variational algorithms [232, 233], it is noteworthy that the proposed algorithm employs only linear-depth circuit ansatzes to estimate electronic energies, which include contributions from electron correlation. This scaling is more favourable than other quantum algorithms that require polynomial-depth circuits.

### 3.3.2 Estimating Correlation Energy Using Linear Depth Quantum Circuits

This section describes four main innovations that are incorporated to estimate the OMP2 energy  $E_{\text{OMP2}}$  with linear-depth circuits using a NISQ device as depicted in Fig. 3.5. As such, this proposed algorithm will be called NISQ-OMP2.

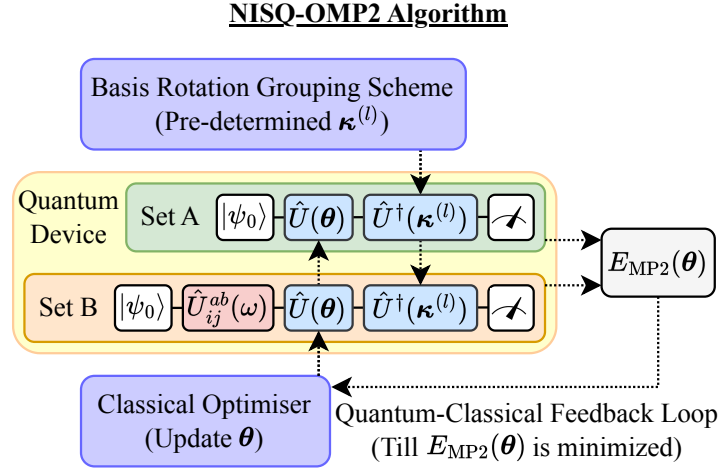


Figure 3.5: Overview of the NISQ-OMP2 algorithm using only quantum circuits whose two-qubit gate depth scales linearly in the number of qubits. The quantum circuits denoted as set A and B are further detailed in Fig. 3.6.

First, the off-diagonal terms in the parameterized second order energy  $E^{(2)}(\ )$  in Eq. (3.42) can be avoided by re-expressing it into ordinary expectation values of the parameterized perturbation term  $\hat{V}(\ )$ . This can be accomplished using a technique from Projective Quantum Eigensolver method [234]. As will be shown in Section 3.3.2, the expectation values  $\hat{V}(\ )$  are with respect to the parameterized reference HF ground  $| \psi_0(\ ) \rangle$  and doubly-excited  $| \psi_{ij}^{ab}(\ ) \rangle$  states.

Second, the expectation values  $\hat{V}(\ )$  are efficiently estimated by implementing the Basis Rotation Grouping scheme on the parameterized perturbation term  $\hat{V}(\ )$ . This reduces the  $O(N^4)$  number of Pauli measurements down to  $O(N)$ , as described earlier in Section 3.2.3.

Third, the required doubly-excited states  $| \psi_{ij}^{ab} \rangle$  are efficiently generated by applying fermionic double excitation rotation  $\hat{U}_{ij}^{ab}(\ )$  in Eq. (3.15) on the reference HF ground state  $| \psi_0(\ ) \rangle$ . The rotation  $\hat{U}_{ij}^{ab}(\ )$  has an efficient gate decomposition [235] that scales linearly in two-qubit gate depth, as will be shown in Section 3.3.2.

Fourth, two independent unitary orbital rotations  $\hat{U}$  are employed for two separate purposes: Orbital-optimization and Basis Rotation Grouping scheme. Each unitary orbital rotation  $\hat{U}$  can be efficiently implemented using the QR decomposition scheme that scales linearly in two-qubit gate depth, as described earlier in Section 3.2.1.

In addition, an active space approach is adopted for larger molecules to isolate relevant molecular orbitals of interest for the calculation of the OMP2 energy. This further reduces the number of qubits and circuit depth needed to represent the parameterized orbital basis transformation, as will be shown in Section 3.3.3.

### Measuring Correlation Energy

Evaluating the off-diagonal elements of  $\hat{V}(\ )$  which determine the second order energy  $E^{(2)}(\ )$  in Eq. (3.42) typically requires the use of a modified Quantum Hadamard test [236] or Swap test [237]. This poses a challenge for NISQ devices as both quantum subroutines require additional ancillary qubits and controlled-quantum gate operations, resulting deep quantum circuits. This section shall demonstrate that this problem can be addressed by building upon the effective measurement of residual elements in the Projective Quantum Eigensolver approach [234] to evaluate the off-diagonal elements of  $\hat{V}(\ )$ .

To simplify the discussion, consider the application of the unitary double excitation rotation  $\hat{U}_{ij}^{ab}(\ )$  with a fixed angle  $\theta$  as in Eq. (3.14) on a reference HF ground state  $| \phi_0 \rangle$  without any orbital transformation,

$$\hat{U}_{ij}^{ab}(\theta) | \phi_0 \rangle = \cos(\theta) I + \sin(\theta) (\hat{a}_a^\dagger \hat{a}_b^\dagger \hat{a}_i \hat{a}_j - \hat{a}_j^\dagger \hat{a}_i^\dagger \hat{a}_b \hat{a}_a) | \phi_0 \rangle \quad (3.44)$$

$$= \cos(\theta) | \phi_0 \rangle + \sin(\theta) | \phi_{ij}^{ab} \rangle. \quad (3.45)$$

Setting the fixed angles  $\theta = \frac{\pi}{2}$  and  $\phi = \frac{\pi}{4}$  in Eq. (3.45), yields the doubly-excited HF states  $|ij^{ab}\rangle$  and the equal superposition with reference HF ground state, respectively,

$$\hat{U}_{ij}^{ab}(\frac{\pi}{2})|0\rangle = |ij^{ab}\rangle, \quad (3.46)$$

$$\hat{U}_{ij}^{ab}(\frac{\pi}{4})|0\rangle = \frac{1}{\sqrt{2}}|0\rangle + |ij^{ab}\rangle. \quad (3.47)$$

Then, the off-diagonal elements  $\langle 0|\hat{V}|ij^{ab}\rangle$  can be expressed in terms of ordinary expectation values as follows,

$$\langle 0|\hat{V}|ij^{ab}\rangle = E_{ij}^{ab,(1)} - \frac{1}{2}E_{ij}^{ab} - \frac{1}{2}E^{(1)}, \quad (3.48)$$

$$E_{ij}^{ab,(1)} = \frac{1}{2}\langle 0| + \langle ij^{ab}| \hat{V} |0\rangle + |ij^{ab}\rangle, \quad (3.49)$$

$$E_{ij}^{ab} = \langle ij^{ab}|\hat{V}|ij^{ab}\rangle, \quad (3.50)$$

$$E^{(1)} = \langle 0|\hat{V}|0\rangle, \quad (3.51)$$

where  $E_{ij}^{ab}$  and  $E_{ij}^{ab,(1)}$  are expectation values of  $\hat{V}$  with respect to the doubly-excited state  $|ij^{ab}\rangle$  and the equal superposition, respectively, and  $E^{(1)}$  is the first order energy term in Eq. (3.25). By reintroducing the orbitals transformation via unitary orbital rotation  $\hat{U}(\theta, \phi)$ , the corresponding parameterized off-diagonal elements  $\langle 0(\theta, \phi)|\hat{V}(\theta, \phi)|ij^{ab}(\theta, \phi)\rangle$  in Eq. (3.42) can be straightforwardly estimated as follows,

$$\langle 0(\theta, \phi)|\hat{V}(\theta, \phi)|ij^{ab}(\theta, \phi)\rangle = E_{ij}^{ab,(1)}(\theta, \phi) - \frac{1}{2}E_{ij}^{ab}(\theta, \phi) - \frac{1}{2}E^{(1)}(\theta, \phi), \quad (3.52)$$

$$E^{(1)}(\theta, \phi) = \langle 0|\hat{U}^\dagger(\theta, \phi)\hat{V}(\theta, \phi)\hat{U}(\theta, \phi)|0\rangle, \quad (3.53)$$

$$E_{ij}^{ab}(\theta, \phi) = \langle 0|\hat{U}_{ij}^{ab,\dagger}(\frac{\pi}{2})\hat{U}^\dagger(\theta, \phi)\hat{V}(\theta, \phi)\hat{U}(\theta, \phi)\hat{U}_{ij}^{ab}(\frac{\pi}{2})|0\rangle, \quad (3.54)$$

$$E_{ij}^{ab,(1)}(\theta, \phi) = \langle 0|\hat{U}_{ij}^{ab,\dagger}(\frac{\pi}{4})\hat{U}^\dagger(\theta, \phi)\hat{V}(\theta, \phi)\hat{U}(\theta, \phi)\hat{U}_{ij}^{ab}(\frac{\pi}{4})|0\rangle. \quad (3.55)$$

For an efficient quantum measurement of the perturbation term  $\hat{V}(\lambda)$ , a Basis Rotation Grouping scheme, as described in Section 3.2.3, is applied to  $\hat{V}(\lambda)$  to obtain,

$$\hat{V} = \hat{U}^{(0)} \sum_p d_q \hat{n}_p \hat{U}^{\dagger (0)} + \sum_{l=1}^{O(N)} \hat{U}^{(l)} \sum_{pq} d_{pq}^{(l)} \hat{n}_p \hat{n}_q \hat{U}^{\dagger (l)}, \quad (3.56)$$

where  $\hat{U}^{(0)}$  is dropped to reduce verbosity, so that the number of Pauli measurements per expectation value estimate of  $\hat{V}(\lambda)$  reduces down to  $O(N)$ .

### Preparing Orbital-Transformed Hartree-Fock Ansatz

Two collections of quantum circuits, set A and B, have been constructed to calculate  $E_{\text{OMP2}}$  as shown in Fig. 3.6(a). For  $l = 0, 1, 2, \dots, O(N)$ , the quantum circuits in set A prepare the orbital-transformed reference HF ground state

$$\hat{U}^{\dagger (l)} \hat{U}(\lambda) | \phi_0 \rangle \quad (3.57)$$

to directly estimate the first order  $E^{(1)}(\lambda)$  in Eq. (3.41). Meanwhile the quantum circuits in set B prepare the orbital-transformed doubly-excited HF state and the equal superposition states,

$$\hat{U}^{\dagger (l)} \hat{U}(\lambda) \hat{U}_{ij}^{ab}(\frac{\lambda}{2}) | \phi_0 \rangle \quad \text{and} \quad \hat{U}^{\dagger (l)} \hat{U}(\lambda) \hat{U}_{ij}^{ab}(\frac{\lambda}{4}) | \phi_0 \rangle \quad (3.58)$$

to directly estimate the expectation values  $E_{ij}^{ab}(\lambda)$  and  $E_{ij}^{ab,(1)}(\lambda)$  in Eqs. (3.54) and (3.55), respectively. The quantum circuit for Unitary orbital rotation for the orbital optimization  $\hat{U}(\lambda)$  and Basis Rotation Grouping scheme  $\hat{U}^{\dagger (l)}$  is depicted in Fig. 3.6(b). The quantum gate decomposition for the fermionic single neighboring excitation  $\hat{U}_{p+1}^p(\lambda)$  that makes up the entire unitary orbital rotation and double excitation rotation  $\hat{U}_{ij}^{ab}(\lambda)$  that generates the doubly-

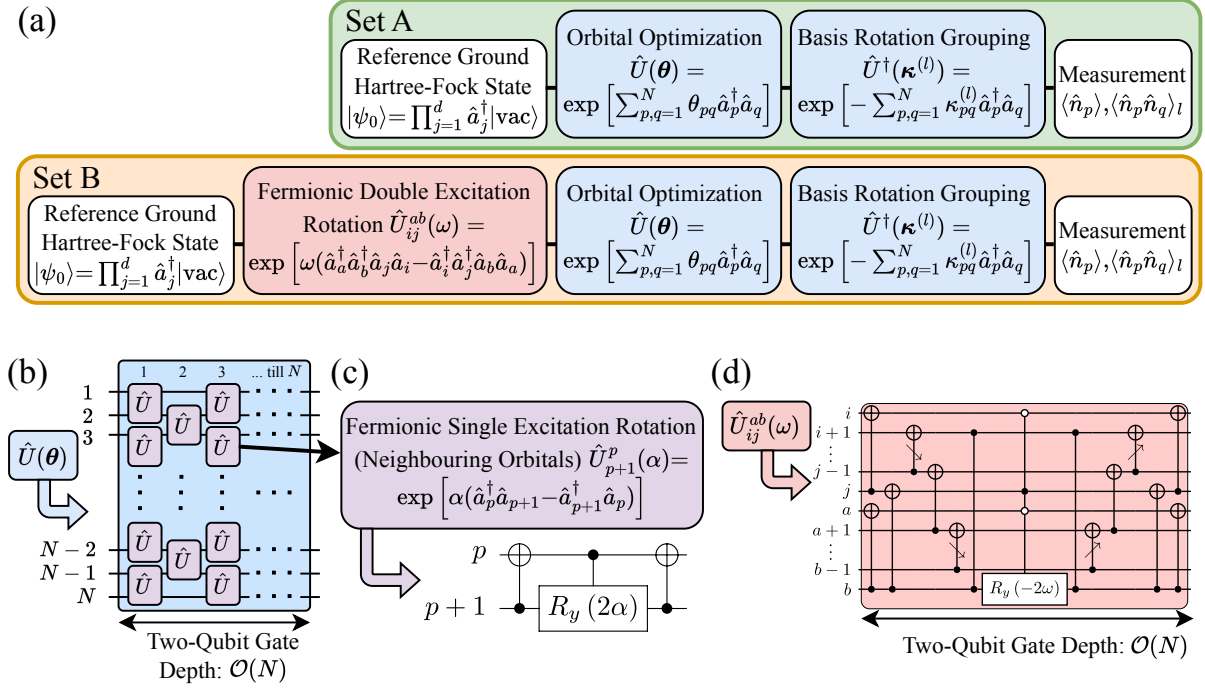


Figure 3.6: (a) NISQ-OMP2 quantum circuits sets A and B in second quantization form. (b) The gate decomposition of unitary orbital rotation  $\hat{U}(\theta)$  for orbital optimization and Basis Rotation Grouping with  $N$  layers of parallel fermionic single-excitation rotation (neighboring orbitals)  $\hat{U}_{p+1}^p(\alpha)$  (c-d) Quantum gate decomposition of the fermionic single  $\hat{U}_{p+1}^p(\alpha)$  and double  $\hat{U}_{ij}^{ab}(\omega)$  excitation rotation gates under the Jordan-Wigner (JW) Mapping [235]. The gate decomposition of CNOTs with diagonal pointing arrows denote CNOT ladders and the multi-controlled rotation Pauli-Y gate are given in Fig. 3.7.

excited HF states, whose circuit depth scales linearly  $\mathcal{O}(N)$  in the number of qubits, are shown in Figs. 3.6(c) and (d), respectively [235].

For  $N_e = \mathcal{O}(N)$  electrons, these two sets of quantum circuits combined will generate  $\mathcal{O}(NN_e^2(N - N_e)^2) = \mathcal{O}(N^5)$  quantum states on a quantum processor. The corresponding measurement results will be used to estimate the parameterized MP2 energy  $E_{\text{MP2}}(\theta, \kappa)$ , which will be fed into a classical optimizer that will generate a new set of parameters  $(\theta, \kappa)$  for the next optimization iteration. This iterative cycle creates a quantum-classical feedback loop that will eventually terminate upon the minimization of  $E_{\text{MP2}}(\theta, \kappa)$  up to a predetermined level of tolerance, thereby outputting OMP2 energy  $E_{\text{OMP2}}$ .

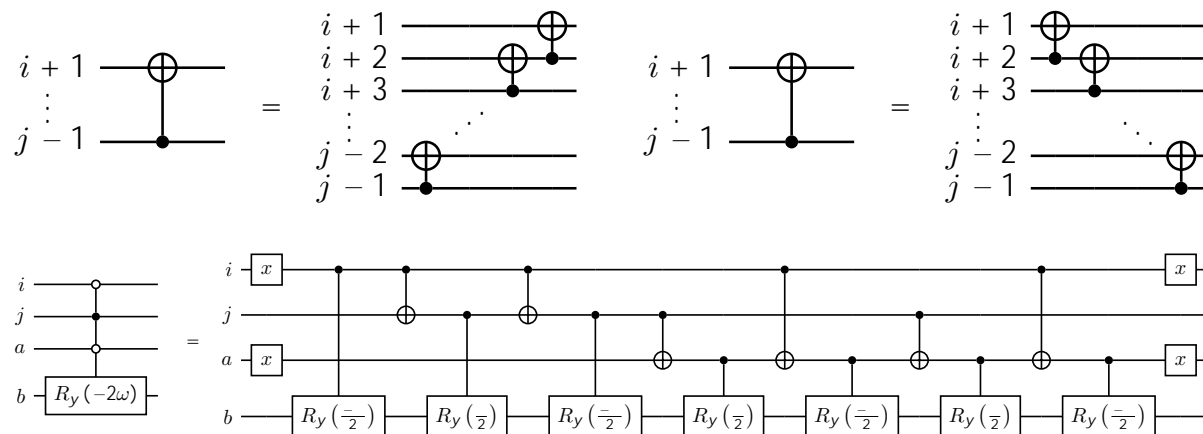


Figure 3.7: Representation of CNOT ladders and explicit quantum circuit decomposition of multi-controlled rotation Pauli-Y gate [238].

### 3.3.3 Examples and Results

For a NISQ demonstration, four molecules are considered: ( $\text{H}_2$ , linear  $\text{H}_3^+$ , LiH and linear  $\text{H}_4$ ) in the minimal STO-3G atomic orbital basis set. This results in the number of spin orbitals, ( $N = 4, 6, 12, 8$ ) and number of electrons ( $N_e = 2, 2, 4, 4$ ) electrons, respectively. A schematic diagram of the index-labelled molecular orbitals of the four molecules is shown in Fig. 3.8.

To reduce the number of orbitals required for the LiH, an active space of 2 occupied valence spin-orbitals and 4 unoccupied virtual spin-orbitals is defined. Thus, the reduced LiH system has  $N_e = 2$  active electrons with  $N = 6$ , instead of the usual  $N = 12$ , active spin-orbitals for OMP2, making its problem size identical to that of linear  $\text{H}_3^+$ .

As a result, under the JW mapping, these molecular cases will require ( $N = 4, 6, 6, 8$ ) qubits, respectively. The corresponding electronic Hamiltonian  $\hat{H}_{\text{ele}}$  is obtained by generating the one- and two-electron integrals using the Psi4 program [239]. The Basis Rotation Grouping scheme is then performed on  $\hat{V}(\ )$  in Eq. (3.56) using the Google’s OpenFermion library [240]. This scheme only needs to be performed once, as the two-electron Coulomb terms

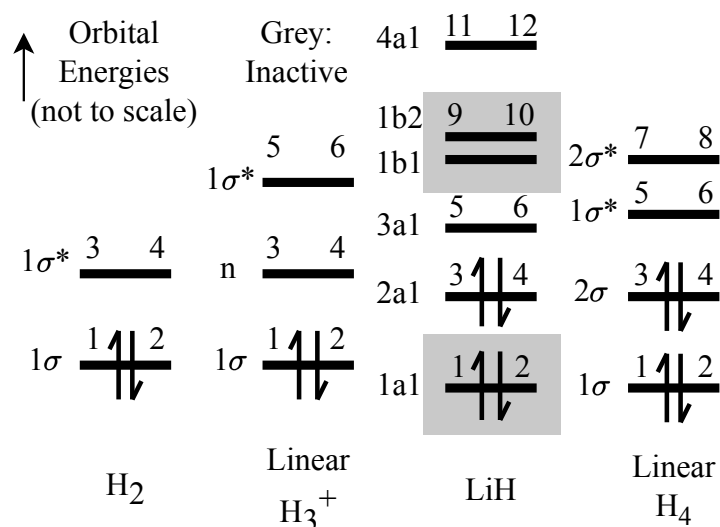


Figure 3.8: Schematic HF molecular orbital (MO) diagrams for various molecules, using the STO-3G atomic orbital basis, with their symmetry labels on the left.  $\sigma$ ,  $\sigma^*$ , and  $n$  orbitals are bonding, antibonding, and nonbonding MOs, respectively. For LiH, the symmetry labels for  $C_{2v}$  point group, which was utilized by the Psi4 code, are shown. Labelled in grey are inactive orbitals that are specified in the construction of an active space, with a frozen-core Hamiltonian scheme for LiH, namely those for the core 1a1 MO, and virtual MOs that have differing symmetry with the 2a1 MO. The remaining active MOs for LiH are studied using the OMP2 method.

are independent of the parameter  $\lambda$ .

### Resource Estimates

For simplicity, all types of two-qubit gates are treated as CNOTs, and no circuit compilation is assumed. Under the JW mapping, the fermionic single neighboring excitation rotation  $\hat{U}_{\rho+1}^{\rho}(\lambda)$  can be decomposed in a circuit with a depth of 3 CNOT gates, as shown in Fig. 3.6(c). Thus, the CNOT circuit depth of every quantum circuit in set A is exactly  $6N$ .

The fermionic double excitation rotation  $\hat{U}_{ij}^{ab}(\lambda)$  can be decomposed using 2 CNOT ladders and a multi-controlled Rotation Pauli-Y [235], as shown in Fig. 3.6(d), which is an 8-fold CNOT depth reduction over the traditional 16 sequential CNOT ladders [241]. The multi-controlled Rotation Pauli-Y is decomposed using the standard technique, which requires a 13

NISQ-OMP2	Scaling	H <sub>2</sub>	H <sub>3</sub> <sup>+</sup>	LiH	H <sub>4</sub>
No. of Qubits	$N$	4	6	6	8
No. of Variational Parameters	$O(N^2)$	1	2	2	4
Max CNOT Depth in Set A	$O(N)$	24	36	36	48
Max CNOT Depth in Set B	$O(N)$	41	55	55	69
No. of Set A Circuits	$O(N)$	4	7	7	11
No. of Set B Circuits	$O(N^5)$	8	84	84	792
Total No. of Circuits (Set A & B)	$O(N^5)$	12	91	91	803
UCCSD					
Max CNOT Depth for UCCSD	$O(N^5)$	40	100	100	600

Table 3.1: Quantum resource estimates of NISQ-OMP2 against 1st Order Trotterised UCCSD approach (One Trotter Repetition), assuming all-to-all qubit connectivity on a quantum processor, for molecules considered in this chapter.

CNOT circuit depth [238] as shown in Fig. 3.7. A more CNOT-efficient gate decomposition of multi-controlled rotation Pauli-Y requiring 5 fewer CNOTs was discovered [235] around the time of this work, but it was not included in the NISQ-OMP2 implementation and thus excluded from the resource analysis. As a result, the fermionic double excitations evolutions have a CNOT gate depth of  $17 + 2(1 - j, i+1) + 2\max\{0, j - i - 2, b - a - 2\}$ , assuming all-to-all qubit connectivity. For a molecule with  $N$  spin-orbitals with  $d$  electrons, the maximum CNOT gate depth possible in set B is

$$6N + 17 + 2(1 - d, 2) + 2\max\{0, d - 3, N - d - 3\} \quad O(N)$$

which corresponds to the double excitation index  $i = 1, j = d, a = d + 1, b = N$ .

The quantum resources required by the NISQ-OMP2 algorithm are estimated and compared against a state-of-the-art VQA that employs standard UCCSD ansatzes. The CNOT circuit depth required for NISQ-OMP2 is compared against the 1st Order Trotterized-UCCSD approach [173] in Tab. 3.1.

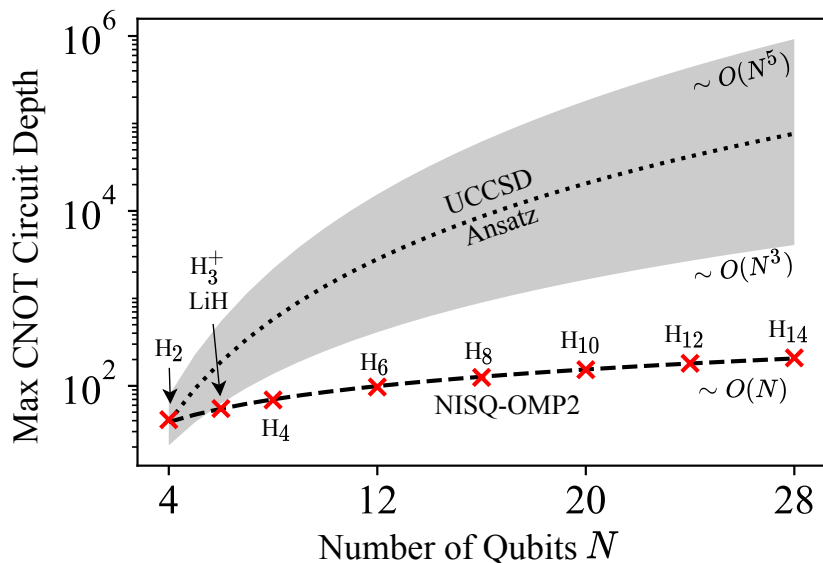


Figure 3.9: Maximum CNOT gate depth required by NISQ-OMP2 and compared against UCCSD ansatz for various molecules in STO-3G atomic basis. Since an active space with 2 electrons and 6 spin orbitals is considered for the LiH molecule only 6 qubits are required.

For the molecules (H<sub>2</sub>, linear H<sub>3</sub><sup>+</sup>, LiH and linear H<sub>4</sub>), the maximum CNOT circuit depth used in NISQ-OMP2 are estimated to be (41, 55, 55, and 69), respectively, which are generally shallower than that of UCCSD approximately (40, 100, 100, 600). The number of circuits in Set A and Set B in NISQ-OMP2 for the four molecules are (4, 7, 7, 11) and (8, 84, 84, 792), respectively, with a combined total of (12, 91, 91, 803) correspondingly.

Additionally, a comparison of the required CNOT gate circuit depths between both algorithms is plotted in Fig. 3.9 for various molecules used in this study and larger hydrogen chains up to H<sub>14</sub> in the STO-3G atomic basis. This comparison shows that the circuit depth required by NISQ-OMP2 scales linearly in number of qubits  $N$ , which represents a polynomial improvement of  $O(N^2)$  compared to the UCCSD approach, in exchange for  $O(N^4)$  times more quantum circuit evaluations under Basis Rotation Grouping scheme. Thus, while NISQ-OMP2 requires more circuit evaluations, it is anticipated to handle larger systems than currently feasible using UCCSD due to the exponential loss of fidelity for deeper circuits.

Optimized Parameters (Unique $(\rho, q)$ odd index)										
$\text{H}_3^+$			LiH			$\text{H}_4$				
Bond (Bohr)	(1,3)	(1,5)	Bond (Bohr)	(3,5)	(3,11)	Bond (Bohr)	(3,5)	(1,5)	(3,7)	(1,7)
1.0	9.59E-09	-3.27E-03	1.9	-9.96E-03	-1.00E-03	1.0	-2.76E-08	3.03E-03	-7.36E-04	7.95E-09
1.2	1.19E-08	-5.10E-03	2.1	-1.08E-02	-1.40E-03	1.2	3.48E-08	3.52E-03	-1.24E-03	6.74E-08
1.4	1.93E-08	-7.48E-03	2.3	-1.17E-02	-1.83E-03	1.4	7.02E-08	3.66E-03	-1.63E-03	-5.25E-08
1.6	1.70E-08	-1.04E-02	2.5	-1.26E-02	2.25E-03	1.6	1.67E-08	3.31E-03	-1.74E-03	1.67E-08
1.8	2.63E-08	-1.40E-02	2.7	-1.35E-02	2.64E-03	1.8	1.98E-08	2.33E-03	-1.40E-03	1.79E-08
2.0	7.46E-09	-1.82E-02	2.9	-1.47E-02	3.03E-03	2.0	2.21E-08	4.01E-04	-5.14E-04	2.21E-08
2.2	8.39E-09	-2.32E-02	3.1	-1.61E-02	3.41E-03	2.2	2.74E-08	-2.15E-03	1.49E-03	1.37E-08
2.4	3.70E-08	-2.90E-02	3.3	-1.78E-02	3.82E-03	2.4	-4.74E-08	-6.00E-03	4.66E-03	-3.15E-09
2.6	1.01E-08	-3.56E-02	3.5	-1.99E-02	4.28E-03	2.6	1.03E-07	-1.14E-02	9.36E-03	5.81E-08
2.8	2.17E-08	-4.30E-02	3.7	-2.25E-02	4.82E-03	2.8	8.91E-08	-1.82E-02	1.56E-02	-2.47E-08
3.0	1.74E-08	-5.11E-02	3.9	-2.56E-02	5.51E-03	3.0	-6.83E-08	-2.64E-02	2.35E-02	-4.07E-08
3.2	-1.22E-08	-5.97E-02	4.1	-2.93E-02	6.41E-03	3.2	-6.75E-08	-3.61E-02	3.30E-02	4.70E-08
3.4	1.90E-08	-6.88E-02	4.3	-3.37E-02	7.62E-03	3.4	1.28E-08	-4.58E-02	4.26E-02	1.84E-08
3.6	-6.56E-09	-7.82E-02	4.5	-3.87E-02	9.27E-03	3.6	-2.25E-08	-5.49E-02	5.19E-02	3.70E-08
3.8	-4.04E-08	-8.78E-02	4.7	-4.44E-02	1.15E-02	3.8	-6.03E-08	-6.28E-02	6.00E-02	4.08E-08
4.0	1.55E-11	-9.76E-02	4.9	-5.10E-02	1.46E-02	4.0	-1.12E-07	-6.90E-02	6.65E-02	1.64E-07
4.2	7.02E-09	-1.07E-01	5.1	-5.80E-02	1.86E-02	4.2	-1.72E-08	-7.33E-02	7.11E-02	4.34E-08
4.4	-3.58E-08	-1.17E-01	5.3	-6.54E-02	2.38E-02	4.4	5.76E-08	-7.56E-02	7.37E-02	-6.88E-08
4.6	2.91E-08	-1.27E-01	5.5	-7.28E-02	3.03E-02	4.6	8.68E-09	-7.62E-02	7.46E-02	-4.94E-09
4.8	6.88E-08	-1.38E-01	5.7	-7.96E-02	3.81E-02	-	-	-	-	-

Table 3.2: Unique L-BFGS-B optimized variational parameters elements as defined above for linear  $\text{H}_3^+$ , LiH and linear  $\text{H}_4$  at various bond distances.

### Orbital Optimization

For the orbital parameterization scheme of [3.1](#), a restricted HF case is assumed, which enforces equal orbital transformation between both spins of the same spatial orbital. Thus, only mixing between occupied and unoccupied spatial orbitals is required. As a result, the parameter matrix

is a  $N \times N$  matrix with  $\frac{N_e(N-N_e)}{4} = O(N^2)$  number of unique variational parameters, such that  $pq = -qp = \rho_{p+1,q+1} = -q_{p+1,p+1}$ ,  $p = \text{odd } i$  and  $q = \text{odd } a$ , and  $pq = 0$  if otherwise.

The unique molecular orbital indices  $\rho, q$  pairs are summarized in respective column headers of Tab. [3.2](#). For example, the parameter matrix of hydrogen molecule  $\text{H}_2$  will be a  $4 \times 4$

matrix and it will be described by one unique parameter such that  $t_{13} = -t_{31} = t_{24} = -t_{42}$  and  $t_{pq} = 0$  if otherwise.

To show the best possible result achievable using the NISQ-OMP2 method, the variational parameters are pre-optimized on a quantum statevector numerical simulator with a classical quasi-Newton L-BFGS-B optimizer using SciPy [242]. The variational parameters are initialized at the origin  $\theta = \mathbf{0}$  and it is found that the optimal parameter matrix for the hydrogen molecule  $H_2$  case remains  $\theta = \mathbf{0}$  for all bond distances, while the optimal parameters for linear  $H_3^+$ , LiH and linear  $H_4$  molecules are given in Tab. 3.2. The average number of L-BFGS-B iterations for  $H_2$ , linear  $H_3^+$ , LiH and linear  $H_4$  are (1, 4, 4, 5), respectively.

### **Benchmarking on NISQ Hardware on the Cloud**

The pre-optimized NISQ-OMP2 algorithm is implemented on two types of quantum computing platforms. The first is on FakeAuckland, a numerical emulation of the noisy IBM-Auckland device via IBM-Qiskit [243]. FakeAuckland will be used to compute the ground state OMP2 energy of all four molecules ( $H_2$ , linear  $H_3^+$ , LiH and linear  $H_4$ ). It is implemented to understand the ideal performance on a NISQ device. The second is on cloud-accessed quantum processors: superconducting 27-qubit IBM-Auckland, superconducting 5-qubit IBM-Lima and ion trap 11-qubit IonQ [244], all of which are provided by quantum cloud service platforms: IBMQ and Amazon Braket, to compute the ground state OMP2 energy of  $H_2$  molecule. The noise parameters of these quantum processors at the time of execution are summarized in Tab. 3.3.

Due to the use of Basis Rotation Grouping, all measurement operators in NISQ-OMP2 are commuting Pauli-Z strings. Thus, each circuit is implemented and sampled to generate a collection of bitstrings measurements or shots, which will be used to estimate all expectation

Cloud Quantum Processors	IBM Auckland	IBM Lima	IonQ
One Qubit Gate Times (s)	3.55E-8	3.55E-8	1.00E-5
One Qubit Gate Fidelity	1(3)E-3	3(2)E-4	4.50E-3
Two Qubit Gate Times (s)	5(3)E-7	4.1(9)E-7	2.00E-4
Two Qubit Gate Fidelity	1(1)E-2	9.51(3)E-3	3.86E-2
Qubit Reset Time (s)	9.4(5)E-7	5.74E-6	2.00E-5
T1 Thermal Relaxation (s)	1.7(5)E-4	1.0(4)E-5	1.00E4
T2 Dephasing (s)	1.4(9)E-4	1.1(7)E-5	2.00E-1
Measurement Error	1(1)E-2	3(2)E-2	1.30E-4
State-Preparation and Measurement (SPAM) Error	Not Given	Not Given	1.76E-3

Table 3.3: Qubit-averaged noise parameters. Values without brackets have no published variances and are thus given to 3 significant figures.

values of the Pauli-Z strings. The total number of shots sampled per circuit on FakeAuckland is set at  $10^5$ , while on the cloud-accessed IBM-Auckland, IBM-Lima and IonQ are set at  $10^5$ ,  $2 \times 10^4$  and  $10^3$ , respectively.

In addition, the bitstring measurements are post-selected so as to mitigate the readout measurement errors and improve the output state fidelity for both quantum computing platforms, respectively. The average post-selected fraction and the average state fidelity of quantum circuit sets are given in the upper and lower parts of Tabs. 3.4 and 3.5, where each table corresponding to each of the two computing platforms, respectively.

The post-selection protocol filters bitstrings with correct number of occupations, representing the conservation of the number of electrons throughout the NISQ-OMP2 algorithm. The output state fidelity between the exact output state  $|\psi_{\text{exact}}\rangle$  and measured output state  $|\psi_{\text{meas}}\rangle$  is defined as  $\langle \psi_{\text{exact}} | \psi_{\text{meas}} \rangle^2$ , that is the probability of obtaining the exact output state  $|\psi_{\text{exact}}\rangle$  from the measured output state  $|\psi_{\text{meas}}\rangle$ . As the

Platform 1: FakeAuckland

Molecules	H <sub>2</sub>	H <sub>3</sub> <sup>+</sup>	LiH	H <sub>4</sub>
Set	Average Post-Selected (PS) Fraction			
A	0.90(7)	0.63(1)	0.521(5)	0.34(1)
B	0.81(4)	0.61(2)	0.48(1)	0.37(2)
Set	Average State Fidelities			
A	0.88	0.56	0.46	0.24
A (after PS)	0.99	0.88	0.89	0.70
B	0.70	0.50	0.38	0.23
B (after PS)	0.86	0.81	0.79	0.63

Table 3.4: Average post-selected fraction and state fidelities of the quantum circuit sets A and B of NISQ-OMP2 implemented on FakeAuckland with 100k shots per circuit for molecules: H<sub>2</sub>, linear H<sub>3</sub><sup>+</sup>, LiH and linear H<sub>4</sub>.

quantum state amplitudes could not be directly accessed in a quantum computer, the state fidelity is estimated by taking the squared inner product of the square root of the state probabilities of the corresponding states in the computational basis.

Here, the results shows that set A generally has a larger post-selected fraction and better state fidelity than set B. This difference is likely due to the additional double-excitation gate in set B, resulting in a deeper circuit than set A. Also, the better set B results is observed on FakeAuckland than on cloud-accessed IBM Auckland, suggesting that the FakeAuckland noise model overestimates the noise performance of actual device at deeper depth of the quantum circuit.

Despite the low state fidelities with obtained in both quantum computing platforms, NISQ-OMP2 is able to reproduce the ground electronic energies around equilibrium internuclear distances and capture the electron correlation-induced energy shifts at longer distances. This

Platform 2: Cloud-Accessed Quantum Processors ( $H_2$  molecule)

Processors	IBM Auckland	IBM Lima	IonQ
No. of shots/circuit	100k	20k	1k
Set	Average Post-Selected (PS) Fraction		
A	0.88(8)	0.8(1)	0.9(1)
B	0.37(2)	0.41(2)	0.59(7)
Set	Average State Fidelities		
A	0.87	0.80	0.86
A (after PS)	0.98	0.97	0.97
B	0.18	0.24	0.46
B (after PS)	0.48	0.59	0.77

Table 3.5: Average post-selected fraction and state fidelities of the quantum circuit sets A and B of NISQ-OMP2 implemented on various cloud-accessed quantum processors with 100k shots per circuit for the  $H_2$  molecule.

effect is shown by the OMP2 energy  $E_{OMP2}$  plots of the various molecules as a function of the bond distance in Figs. 3.10 and 3.12 on the respective platforms. The corresponding first  $E^{(1)}$  and second order  $E^{(2)}$  energies are shown in Figs. 3.11 and 3.13 on the respective platforms.

Figure 3.10 compares the OMP2 energy  $E_{OMP2}$  obtained between the noiseless statevector simulator and FakeAuckland, with and without post-selection. In the absence of noise (green triangles in Fig. 3.10), there is good agreement with the exact OMP2 energy obtained numerically using Psi4, with small deviations arising due to shot noise from finite sampling (100k shots per distinct circuit). For all molecules, it is observed that OMP2 energy is consistently well-below the HF energy, which shows that NISQ-OMP2 recovers the correlation energy around the equilibrium and intermediate bond distances as expected.

The raw OMP2 energies obtained under FakeAuckland are plotted as blue ‘o’ markers

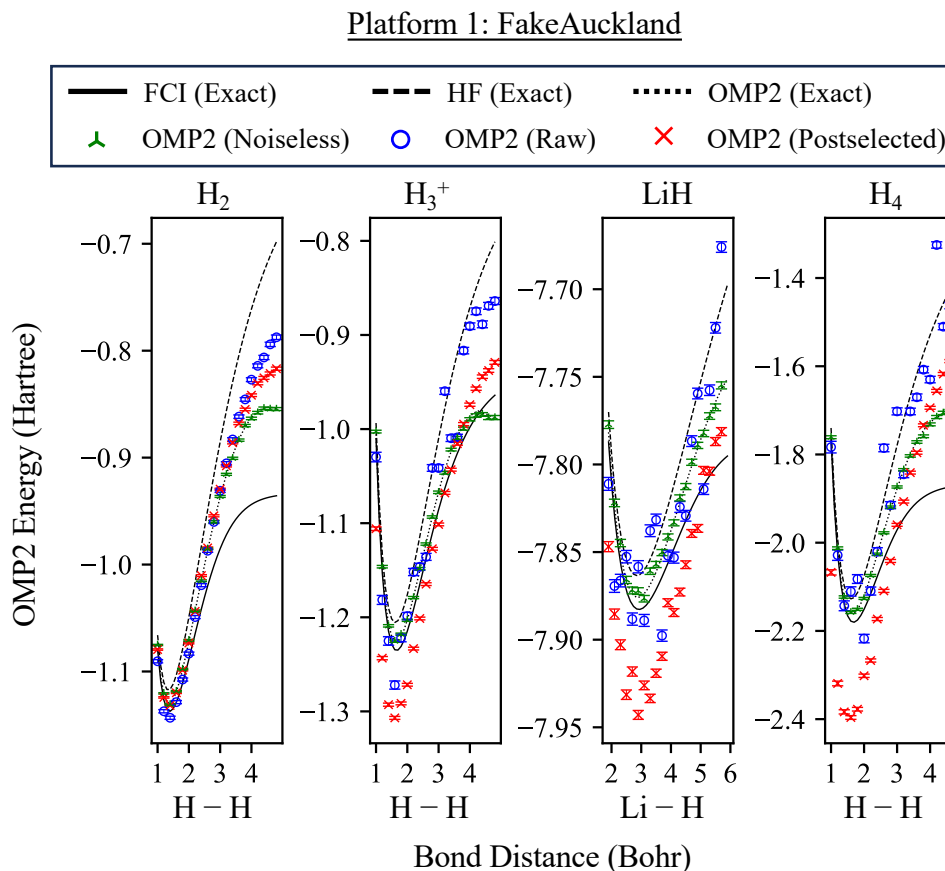


Figure 3.10: Orbital-optimized MP2 energy  $E_{OMP2}$  for  $H_2$ , linear  $H_3^+$ ,  $LiH$  and linear  $H_4$  at various bond distances obtained using noiseless statevector simulator (green tri-ups markers) and FakeAuckland, with (red ‘x’ markers) and without (blue ‘o’ markers) post-selection. The exact energies for HF, OMP2 and FCI calculated classically using Psi4 are plotted as dashed, dotted and solid black lines, respectively. The error bars are calculated from estimating the covariance matrix of the commuting Pauli-Z strings of the quantum measurements of the perturbation term  $\hat{V}$  based on 100,000 shots per circuit.

in Fig. 3.10. Generally, the raw results have significant deviations from the corresponding exact OMP2 energies at longer bond distances, due to the second order energy  $E^{(2)}$  becoming increasingly less accurate at longer bond distances, as shown in Fig. 3.11. As expected, it is found that these deviations are caused by low quantum state fidelity of the deeper set B circuits, shown in Tab. 3.4.

The corresponding post-selected OMP2 energies, shown in red ‘x’ markers in Fig. 3.10,

were found to have fewer random errors than the raw OMP2 plots. This improvement is likely due to the mitigation of the measurement readout errors as evidenced by the improved state fidelity, though it remains significantly less than 90%, which is very low as shown in Tab. 3.4. Interestingly, it is observed for  $\text{H}_3^+$ , LiH and  $\text{H}_4$  molecules that the post-selection energies are less accurate than that of raw ones. Analyzing the energy order terms shows that the systematic error of the first order energy increases while that of the second order energy decreases as given in Fig. 3.11 which might be caused by noise model used in FakeAuckland. Since the systematic error of the first order energy is larger in magnitude than of the second order, it therefore leads to worse post-selected OMP2 energies, indicating the presence of error cancellation during calculation.

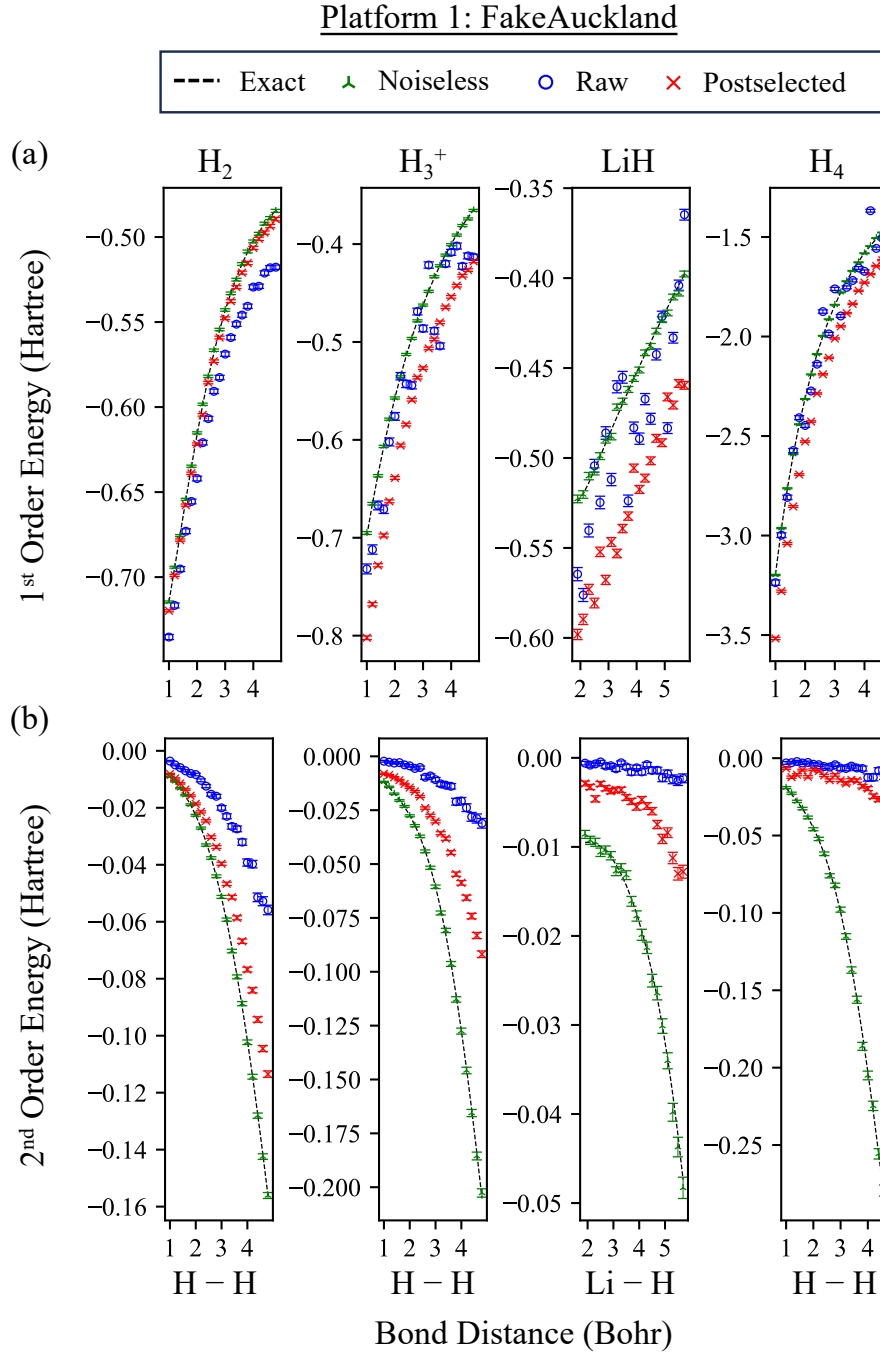


Figure 3.11: (a) First Order  $E^{(1)}(\mathbf{r})$  and (b) Second Order  $E^{(2)}(\mathbf{r})$  Energies in Eq. (3.38), where  $\mathbf{r}$  are the optimized parameters, for  $H_2$ , linear  $H_3^+$ ,  $LiH$  and linear  $H_4$  for various bond distances, implemented on FakeAuckland with 100,000 shots per circuit.

Platform 2: Cloud-Accessed Quantum Processors (H<sub>2</sub> Molecule)

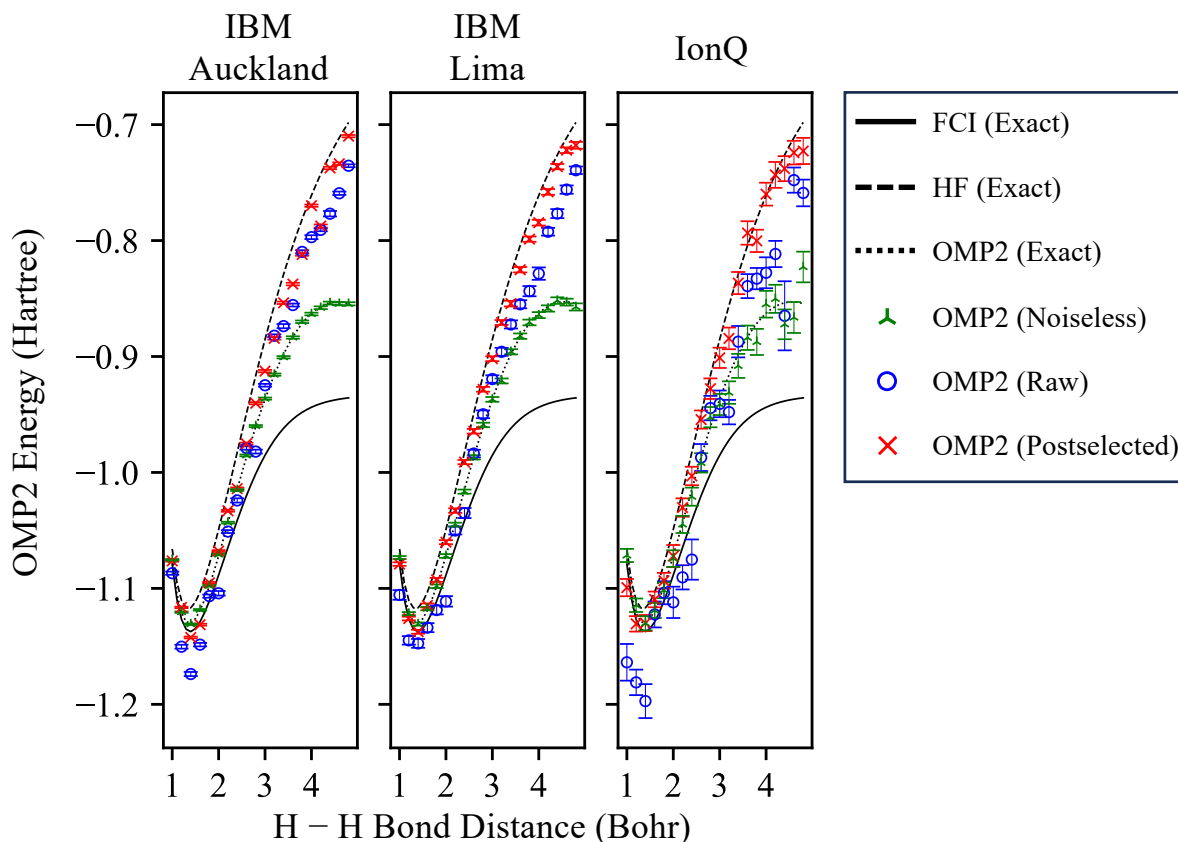


Figure 3.12: Orbital-optimized MP2 energy  $E_{\text{OMP2}}$  for H<sub>2</sub> at various bond distances evaluated using different cloud quantum processors with (red ‘x’ markers) and without (blue ‘o’ markers) post-selection: 27-qubit IBM Auckland (100,000 shots per circuit), 5-qubit IBM Lima (20,000 shots per circuit), and 11-qubit IonQ (1,000 shots per circuit). For comparison, the results of a noiseless statevector simulator are plotted in green triangles, and the exact energies for HF, OMP2 and FCI calculated classically using Psi4 are shown as dashed, dotted and solid black lines, respectively.

Next, the OMP2 energy  $E_{\text{OMP2}}$  for the H<sub>2</sub> molecule is evaluated on the cloud-accessed quantum devices: IBM Auckland, IBM Lima, and IonQ. The raw energies are shown as blue ‘o’ markers in Fig. 3.12. For all tested cloud quantum processors, the raw OMP2 energy plots show a clear qualitative description of electronic energy around equilibrium H<sub>2</sub> bond distance of 1.4 Bohr, with random errors decreasing with the number of shots used.

As expected, the corresponding post-selected OMP2 energy, as given in red ‘x’ markers

in Fig. 3.12, was observed to have fewer random errors than the raw results. Generally, post-selection also led to more accurate energies around the equilibrium bond distance, but deviations occur for longer bond distances. As mentioned above, these deviations are mainly due to the lower quantum state fidelity of the deeper set B circuits as shown in Tab. 3.5. This generally causes the post-selected first order energy  $E^{(1)}$  to be relatively more accurate than that of post-selected second order energy  $E^{(2)}$ , as shown in the Fig. 3.13. As a result, post-selected OMP2 energy data exhibit a closer match to classically obtained values around the equilibrium bond distance where, the first order energy  $E^{(1)}$  is most significant, while it deviates at longer bond distance where post-selected second order energy  $E^{(2)}$  is becomes more important.

Platform 2: Cloud-Accessed Quantum Processors (H<sub>2</sub> Molecule)

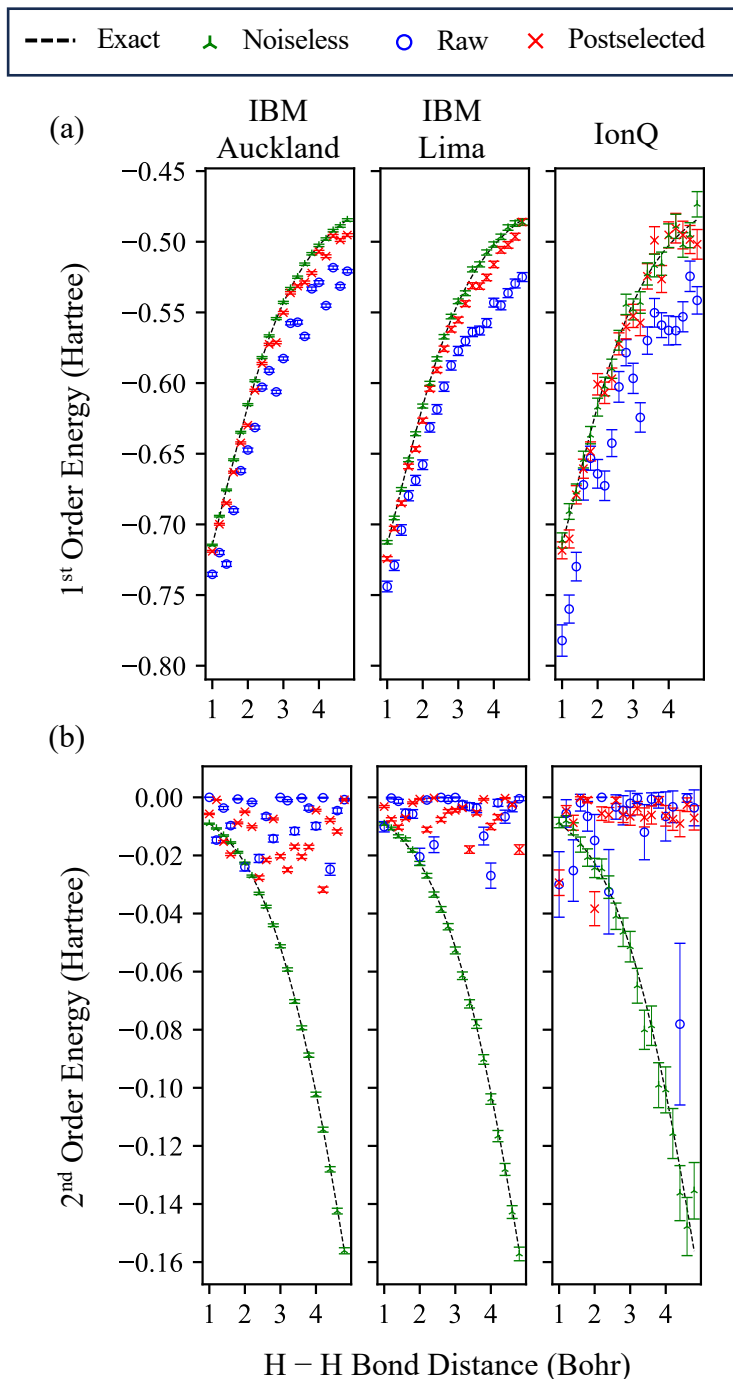


Figure 3.13: (a) First Order  $E^{(1)}(\ )$  and (b) Second Order  $E^{(2)}(\ )$  Energies in Eq. (3.38), where  $\theta$  are the optimized parameters, for H<sub>2</sub> for various bond distances, implemented on a various cloud quantum processors: 27-qubit IBM Auckland (100,000 shots per circuit), 5-qubit IBM Lima (20,000 shots per circuit), and 11-qubit IonQ (1,000 shots per circuit).

### 3.4 Discussion and Conclusion

Applications of NISQ-OMP2 algorithm beyond estimating electronic energies could involve solving other quantum chemistry problems where many-body perturbation theory has been fruitfully applied. These include the estimation of atomization energies, electron affinities, and ionization potentials of covalent systems, and other quantities that are difficult to obtain by experiment, such as the interaction energy between noble gas atoms. The NISQ-OMP2 algorithm could also serve as a quick benchmarking tool, where the fidelity of superposed HF states or the second-order correlation energy can be used as metrics to identify early-FTQC quantum computers most suitable for quantum computational chemistry algorithms that require Post-HF ansatzes.

To realize these potential applications, further improvements NISQ-OMP2 algorithm can be introduced to improve its practicality and accuracy. For example, instead of relying on the quantum cloud providers' circuit transpilers, which may be not depth-optimal, direct transpilation of the quantum circuit may be used to leverage NISQ hardware's native quantum gates to reduce the overall quantum circuit depth and improve the quantum fidelity of fermionic excitation rotation. NISQ-OMP2 can be sped up by executing multiple quantum circuits from set A and B in parallel on the same quantum device to reduce the total number of quantum circuit repetitions, in exchange for requiring more qubits. It will also be interesting to explore whether other fermion-to-qubit mappings such as Bravyi-Kitaev [6, 208] can be used to further reduce the number of qubits and circuit depth.

The post-selected results obtained using the cloud-accessed NISQ devices was observed to be worse than the raw results, despite the improved state fidelity. This due to the net increase

in the systematic error of the OMP2 energy, a symptom of error cancellation. This reveals the limitation of post-selection where mitigating a single error type, namely electron number, may ironically further worsen the final result. Therefore, it highlights the importance of identifying and suppressing potential sources of error so as to minimize all systematic errors evenly, thereby suppressing the effects of error cancellation. One major source of error is the quantum gate error which remains a difficult issue in the NISQ era as current quantum error correction (QEC) techniques have yet to become practical [245].

Therefore, an important direction for future work is to implement efficient error-mitigation techniques such as zero-noise extrapolation [87, 88, 161] that could help to improve the state fidelity and provide a more accurate energy estimate without incurring expensive numerical overheads. In addition, it would be useful to improve the quality of orbital optimization on real NISQ devices using noise-resilient classical optimization techniques such as simultaneous perturbation stochastic approximation [246] and particle swarm optimization [247]. Tangent to this direction, it would be beneficial to develop methods to determine precise parameter bounds for local optimization of OMP2 energy to improve the robustness of the noisy optimization.

NISQ-OMP2 algorithm provides a perturbative estimate of the ground state electronic energies that include explicit second-order correlation effects using NISQ-friendly linear-depth quantum circuits with minimal heuristics. It involves several innovations from multiple sources incorporated into NISQ-OMP2 to ensure that the required quantum states and correlated electronic energy could be practically prepared and measured in NISQ devices. Although such an approach is not completely superior to other VQE approaches such as UCC in the recovery of electron correlation, NISQ-OMP2 avoids exponentially lower state fidelities that

result from deep entangling circuits that requires at least  $O(N^3)$  circuit depth. As the fidelities of quantum processors improve, it is expected that NISQ-OMP2 will enable the study of moderately larger molecular systems without requiring full quantum error correction.

## Chapter 4

# Shallow Circuits for Efficient Correlated State Preparation

This chapter adapts the material published in:

- C. H. Chee, D. Leykam, A. M. Mak, and D. G. Angelakis, “Shallow quantum circuits for efficient preparation of Slater determinants and correlated states on a quantum computer”, *Phys. Rev. A* **108**, 022416 (2023).

### 4.1 Introduction

Fermionic ansatz state preparation is a critical subroutine in many quantum algorithms for quantum chemistry and condensed matter applications [142]. For example, the success probability of quantum phase estimation in determining eigenenergies of electronic systems relies on the overlap between the fermionic ansatz and the corresponding exact eigenstates [134,

137, 138]. Consequently, the efficient preparation of high-quality ansatz states is essential for many-body applications such as ground state energy estimation and quantum dynamics simulation [15, 16, 28].

Most current methods for preparing fermionic ansatzes use second quantization with Jordan-Wigner (JW) fermion-to-qubit mapping [5]. This approach efficiently represents the quantum many-body fermionic wavefunction as a qubit wavefunction, with a number of qubits that scales linearly with the system size [15, 16]. Common fermionic ansatzes generally fall into two main categories. The first category includes hardware-efficient ansatzes that utilize parameterized hardware-native gates to minimize the depth of the quantum circuit [149]. However, these ansatzes present significant optimization challenges [170] and often fail to ensure an accurate representation of the target quantum state after optimization [169]. The second category consists of problem-inspired ansatzes, which hold greater potential as they explicitly incorporate the physics of the system. Despite their promise, these ansatzes require deeper circuits that scale polynomially in system size, thereby increasing errors on Noisy Intermediate-Scale Quantum (NISQ) devices due to quantum noise and decoherence [157, 171–173, 175–178]. As a result, state-of-the-art NISQ demonstrations for quantum chemistry are limited to fewer than one hundred qubits [184, 185], rendering the studies of chemically-relevant molecular systems requiring more than  $10^2$ – $10^3$  qubits unattainable [143, 186].

The simplest general-purpose problem-inspired ansatz states currently available are the mean-field Hartree-Fock (HF) states [157, 171, 172], which are single Slater determinant wavefunctions, as described in Section 3.2.1. These states can be prepared by applying a fermionic basis transformation, specifically a unitary orbital rotation, to a reference HF state. The corresponding quantum circuit involves layers of two-qubit fermionic single-excitation

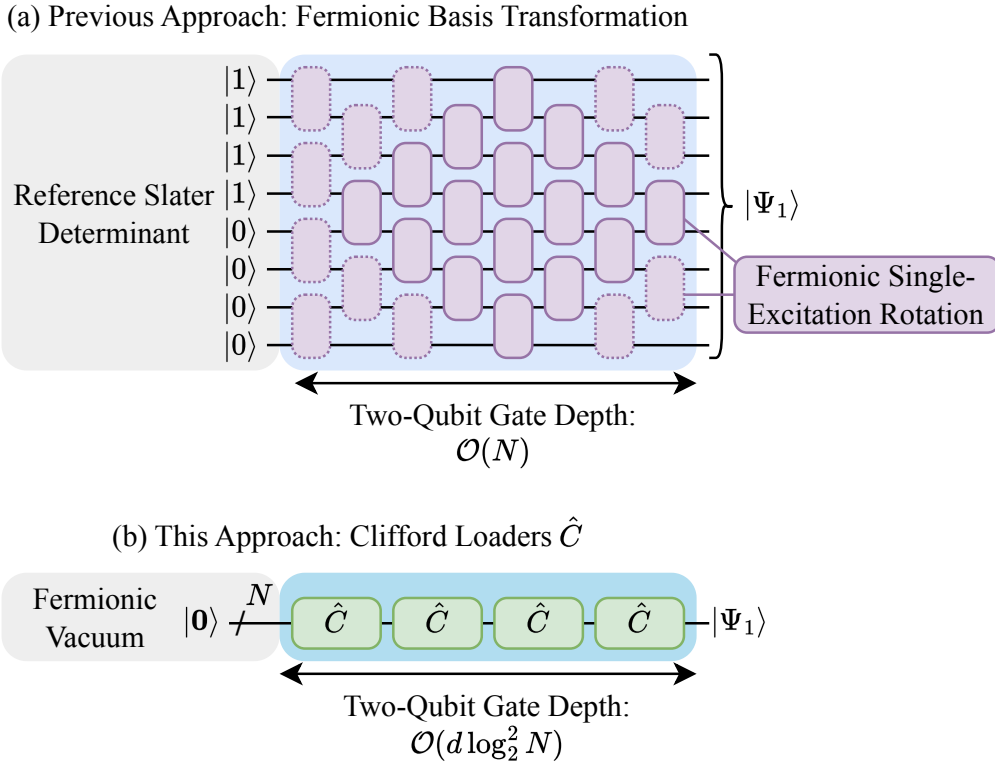


Figure 4.1: Different approaches for preparing  $d = 4$  occupied Slater determinant of  $N = 8$  modes on a quantum computer, assuming real orbitals and Jordan-Wigner mapping. (a) A fermionic basis transformation (blue region), equivalent to Fig 3.1, that consists layers of fermionic of single-excitation rotation (purple gates) applied on a reference Slater determinant. Using an alternative QR decomposition, gates with dotted outlines can be made redundant and removed to reduce gate counts and depth [157, 171, 172]. (b) The proposed method of applying a sequence of Clifford loaders  $\hat{C}$  gates  $d$  times to a fermionic vacuum state  $|\text{vac}\rangle$ .

rotation gates, resulting in an overall shallow two-qubit gate depth that scales linearly with the number of qubits  $N$ , as illustrated in Fig. 4.1(a). Although HF states are efficiently simulatable on classical computers, they provide a crucial foundation for quantum computers to construct more complex classically-intractable correlated quantum ansatzes. An example is the Unitary Coupled Cluster (UCC) ansatz, which incorporates electronic correlations by applying number-conserving multi-fermion excitation operators to a reference HF state [173–178] as elucidated in Section 3.2.2.

Fermionic excitation operators are examples of Givens rotations, which perform rotations

within a two-dimensional fermionic subspace of a larger Hilbert space. Along with their qubit controlled gate variants, these Givens rotations form a universal quantum gate set capable of realizing any particle-conserving unitaries [248, 249]. Thus, Givens rotations have proven invaluable for preparing various fermionic states in quantum chemistry and condensed matter applications [157, 171–173, 175, 235, 250, 251]. Recently, these gates have garnered interest in the field of quantum linear algebra, where they have been employed to construct shallow-depth “Clifford loaders” gates. These gates, which are linear combinations of anti-commuting operators, can efficiently encode  $d$ -dimensional subspaces of  $\mathbb{R}^N$  into an  $N$ -qubit state [252–255]. This capability enables potential end-to-end quantum speedups for several quantum machine learning and linear algebra tasks including determinant sampling and topological data analysis [252]. Therefore, it is pertinent to investigate the utility of implementing Clifford loaders via the Givens rotation for preparing of fermionic ansatz states.

This chapter develops an alternate paradigm for fermionic state preparation, offering shallower, yet scalable approach to prepare  $d$ -fermion Slater determinants and correlated fermionic states than existing problem-inspired approaches. Specifically, this chapter introduces a novel state preparation technique involving Clifford loaders  $\hat{C}$ , constructed from Givens rotations, as shown in Fig. 4.1(b). The quantum circuit implemented by this technique has an overall  $O(d \log_2^2 N)$  two-qubit gate depth under the JW mapping.

Additionally, this technique is extended to prepare  $L$ -wise correlated fermionic ansatz, which correlates between  $L$ -tuples of fermionic modes. This yields a quantum circuit that is shallower by a factor of  $L$  compared to the Slater determinant. This approach is then used to generate ( $L=2$ )-wise correlated ansatz to demonstrate its ability to capture a significant fraction of ground state correlation energy in Hydrogen chains up to  $N = 20$  qubits, where pairwise

electronic correlation ( $L = 2$ ) is likely to be significant. The results establish Clifford loaders as an efficient and scalable method for preparing of fermionic ansatz, offering a subexponential reduction in  $N$  over existing problem-inspired approaches such as UCC. This approach may enable high-accuracy quantum chemistry studies of sufficiently slow-growing  $d = O(N/\log_2^2 N)$  fermionic systems with larger basis sets on near-term quantum devices.

## 4.2 Preparing Fermionic Wavefunctions Efficiently

### 4.2.1 Slater determinants

An arbitrary Slater determinant  $|\Psi_1\rangle$  with  $d$  occupied and  $N - d$  unoccupied fermionic modes is defined as [171, 256–258]

$$|\Psi_1(\mathbf{A})\rangle := \sum_{l=1}^d \sum_{\mu=1}^N A_{\mu l} \hat{a}_\mu^\dagger |\text{vac}\rangle, \quad (4.1)$$

where  $\mathbf{A}$  is a  $N \times d$  real matrix such that all  $d$  columns are orthogonal and normalized,  $|\text{vac}\rangle$  is a vacuum state, and  $\hat{a}_\mu^\dagger$  is a fermionic creation operator acting on the  $\mu^{\text{th}}$  mode.

While the definition in Eq. (4.1) is pedagogically convenient, it requires non-unitary operators  $\sum_{\mu=1}^N A_{\mu l} \hat{a}_\mu^\dagger$  which cannot be directly implemented on a quantum circuit. Thus, a straightforward

method to prepare arbitrary Slater determinants is to perform a fermionic basis transformation

$\exp\left(\sum_{\mu=1}^N \sum_{r=1}^d \hat{a}_\mu^\dagger \hat{a}_r\right)$  on a reference Slater determinant state  $\prod_{r=1}^d a_r^\dagger |\text{vac}\rangle$ , as shown in Fig. 4.1.

This method results in a linear two-qubit quantum gate depth scaling in number of qubits  $N$  [157, 172], that is

$$|\Psi_1(\mathbf{A})\rangle = \exp\left(\sum_{\mu=1}^N \sum_{r=1}^d \hat{a}_\mu^\dagger \hat{a}_r\right) \prod_{r=1}^d a_r^\dagger |\text{vac}\rangle, \quad (4.2)$$

where the real-valued skew-Hermitian parameter matrix is such that the first  $d$  columns of the unitary matrix  $\exp(\cdot)$  is equal to  $\mathbf{A}$ .

### 4.2.2 Idea: Linear Combinations of Anti-Commuting Operators

Alternatively, the Slater determinant  $|\Psi_1(\mathbf{A})\rangle$  can be prepared using Clifford Loaders  $\hat{C}(A_l)$ , which are defined as a linear combination of the anti-commuting operators  $\hat{\rho}_\mu$  with linear coefficients  $A_{\mu l}$ ,

$$\hat{C}(A_l) = \sum_{\mu=1}^N A_{\mu l} \hat{\rho}_\mu, \quad (4.3)$$

where

$$\hat{\rho}_\mu = \hat{a}_\mu^\dagger + \hat{a}_\mu \quad \text{s.t.} \quad \{\hat{\rho}_\mu, \hat{\rho}_\nu\} = 2 \delta_{\mu\nu} \mathbf{I}, \quad (4.4)$$

where readers may refer to Appendix A.2 on the proof of anti-commuting relations in Eq. (4.4).

Applying the Clifford loaders  $\hat{C}(A_l)$  on a vacuum state  $|\text{vac}\rangle$ , for  $l = 1, \dots, d$  in succession, generates the desired Slater determinant, as shown in Fig. 4.1(b),

$$|\Psi_1(\mathbf{A})\rangle := \prod_{l=1}^d \hat{C}(A_l) |\text{vac}\rangle \quad (4.5)$$

$$= \sum_{\mu=1}^N \prod_{l=1}^d A_{\mu l} \hat{\rho}_\mu |\text{vac}\rangle. \quad (4.6)$$

Interested readers may refer to Appendix A.1 on the proofs of equivalence between two definitions of Slater determinants in Eq. (4.1) and the proposed one in Eq. (4.6).

This section consider the Givens rotation gate depth decomposition of the Clifford loader  $\hat{C}(A_l)$  in Eq. (4.3) described by Kerenidis and Prakash [252], as shown in Fig. 4.2,

$$\hat{C}(A_l) = \hat{D}(A_l) \hat{\rho}_1 \hat{D}^\dagger(A_l), \quad (4.7)$$

where it consists of an operator  $\hat{\rho}_1 = \hat{a}_1^\dagger + \hat{a}_1$  acting on the first mode sandwiched by  $\hat{D}$  and  $\hat{D}^\dagger$ ,

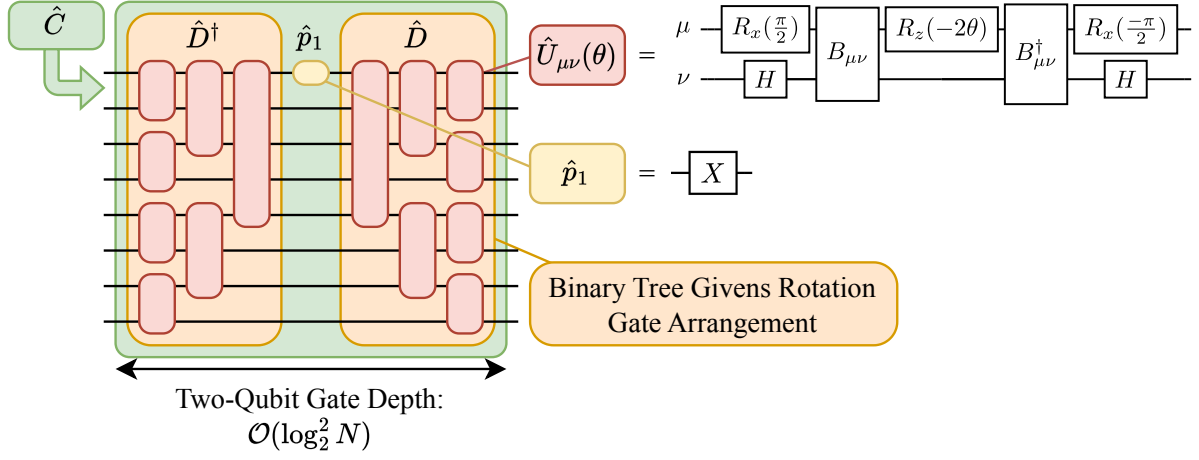


Figure 4.2:  $N = 8$  qubit example of a Clifford loader  $\hat{C}$  consisting of two sets of multiple Givens rotations  $\hat{D}$ ,  $\hat{D}^\dagger$  in a binary tree arrangement, each with  $\log_2 8 = 3$  sublayers, that sandwich the operator  $\hat{\rho}_1$ . Under the JW mapping, the Givens rotation  $\hat{U}_\mu$  is decomposed using Pauli rotation gates  $R_x$ ,  $R_z$  acting on qubit  $\mu$ , Hadamards  $H$  acting on qubit  $\nu$ , and CNOT ladders  $B_\mu$  acting on all qubits between  $\mu$  and  $\nu$  as shown in Fig. 4.4.  $\hat{\rho}_1$  is a Pauli-X operator.

known as unary data loaders [252, 255, 259],

$$\hat{D}^\dagger(A_I) = \prod_{s=1}^{\log_2 N} \prod_{\mu, \nu \in T_s} \hat{U}_\mu(\theta_\mu^{(s)}) . \quad (4.8)$$

Each unary data loader  $\hat{D}^\dagger(A_I)$  consist products of multiple Givens rotations

$$\hat{U}_\mu(\theta) = \exp[ -i \theta \hat{\rho}_\mu ], \quad (4.9)$$

such that

$$\begin{aligned} \hat{U}_\mu(\theta) \hat{\rho}_r \hat{U}_\mu^\dagger(\theta) &= \cos(2\theta) \hat{\rho}_r + \sin(2\theta) \hat{\rho}_\mu \quad r = \mu, \\ \hat{U}_\mu(\theta) \hat{\rho}_r \hat{U}_\mu^\dagger(\theta) &= \cos(2\theta) \hat{\rho}_r - \sin(2\theta) \hat{\rho}_\mu \quad r = \nu, \\ \hat{\rho}_r &= \hat{\rho}_\mu \quad r = \mu, \nu, \end{aligned} \quad (4.10)$$

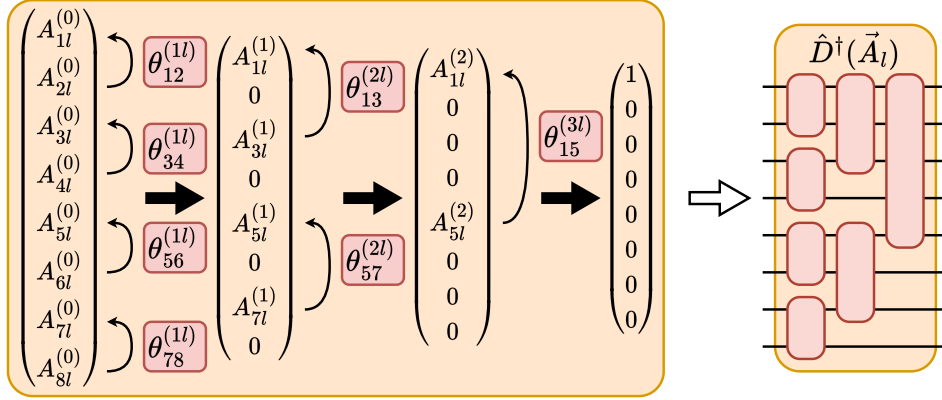


Figure 4.3: Example of  $N = 8$  qubit binary tree given rotation gate angle decomposition.

which are arranged in a binary tree arrangement according to the set of  $(\mu, )$  indices

$$\mathbb{T}_s = \{(\mu, ) / \mu = 2^s(k-1)+1, = 2^{s-1}(2k-1)+1, k \in \mathbb{Z}^+ \setminus \{0\}\}, \quad (4.11)$$

for each sublayer  $s \in \{1, \dots, \log_2 N\}$ .

By treating  $A_l = (A_{1l}^{(0)}, \dots, A_{Nl}^{(0)})$  in Eq. (4.8) as a vector in the anti-commuting operator basis of  $\{\hat{\rho}_1, \dots, \hat{\rho}_N\}$ , one numerically performs parallel Givens rotations on  $A_l$  which correspond to the sequence in  $\hat{D}^\dagger$ , shown in Fig. 4.3. This successively zeros out the vector elements till the first element of  $A_l$  becomes unity  $A_{1l}^{(\log_2 N)} = 1$  corresponding to  $\hat{\rho}_1$ . The corresponding Givens rotation angles  $\theta_{\mu}^{(s)}$  in Eq. (4.8) are calculated as

$$\theta_{\mu}^{(s)} = \frac{1}{2} \arctan \frac{A_{l}^{(s)}}{A_{\mu l}^{(s)}}. \quad (4.12)$$

Under the Jordan-Wigner mapping, the anti-commuting operator  $\hat{\rho}_\mu$  maps to a Pauli

string contain Pauli-Z and X operators,

$$\hat{\rho}_\mu = \prod_{r=1}^{\mu-1} \hat{Z}_r \hat{X}_\mu, \quad (4.13)$$

and thus, the Givens rotation in Eq. (4.9) becomes

$$\hat{U}_\mu ( ) = \exp[-i \hat{Y}_\mu \hat{X}_\mu \prod_{r=\mu+1}^{-1} \hat{Z}_r], \quad (4.14)$$

which is a Pauli string rotation gate that can be easily implemented on a quantum circuit [235, 241] as shown in Fig. 4.2(b). This Givens rotation  $\hat{U}_\mu$  differs from the one used by Kerenidis and Prakash, known as a Fermionic Beam Splitter (FBS) [252]. FBS serves a similar purpose as the Givens rotation  $\hat{U}_\mu$ , that is to implement the unary data loader  $\hat{D}^t(A_l)$ , and has equal two-qubit gate depth complexity, but it differs in terms of its gate decomposition. In the gate decomposition of the Givens rotation  $\hat{U}_\mu$ , the CNOT ladder  $B_\mu$  that consists of a cascade of CNOT gates serves the purpose of encoding the parity of non-excited qubits into the rotation gate [235, 241]. However, this CNOT ladder can be replaced by a non-equivalent binary tree CNOT gate arrangement [252] as shown in Fig. 4.4, without any effect on the Givens rotation  $\hat{U}_\mu$ , thereby reducing the CNOT depth from linear to logarithmic in  $N$ . Thus, by implementing  $d$  such Clifford loaders with these Givens rotation gates, the Slater determinants can be prepared with a shallow  $O(d \log_2^2 N)$  two-qubit gate depth quantum circuit.

In the case of  $d > \frac{N}{2}$ , Clifford loader will instead be applied  $N - d$  times, followed by occupation-vacant mode swap to all Fock basis at the end. This process is equivalent to a Pauli-X bitflip to all qubits under the JW mapping. The Slater determinant in Eq. (4.5) can

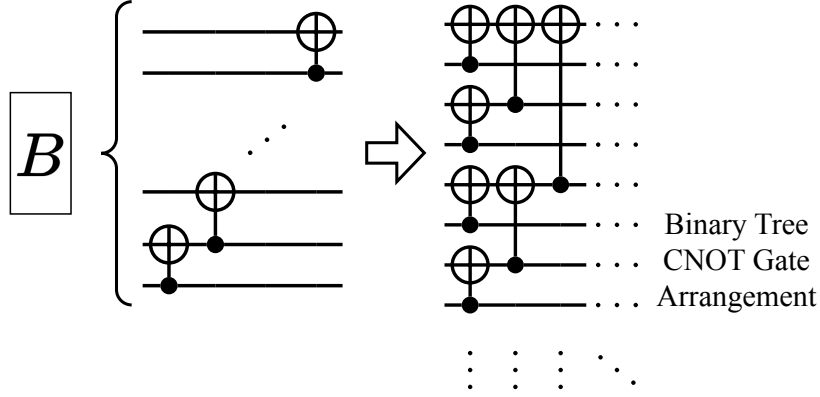


Figure 4.4: Linear-depth cascading CNOT ladder  $B$  in the decomposition of Givens rotations gate  $\hat{U}$  is replaced by a non-equivalent logarithmic-depth circuit that has no effect on  $\hat{U}$ .

be further simplified to [252, 260]

$$|\Psi_1(\mathbf{A})\rangle = \sum_{|B|=d} \det(\mathbf{A}_B) |B\rangle, \quad (4.15)$$

where the sum is over all possible combinations of the ordered set  $B$  containing  $d$ -unique integers from 1 to  $N$  of a fixed set size  $|B| = d$ ,  $\mathbf{A}_B$  is a  $d \times d$  matrix minor of  $\mathbf{A}$  whose row indexes are restricted by  $B$ , and  $|B\rangle$  denotes an  $N$ -mode Fock basis with occupied modes indexed by  $B$ , as shown in Appendix A.3.

### 4.2.3 Extension to Correlated States

This section proposes to extend the technique in the previous section to incorporate  $L$ -wise correlations into the fermionic ansatz state preparation, where  $L = 1$  reduces to the Slater determinant case. The idea is to use a different set of anti-commuting operators containing non-particle preserving multi-body Fock operators and reapply the same technique undertaken in Slater determinant case. For simplicity, consider Pauli string operators instead of the fermionic operators under the Jordan-Wigner mapping. The anti-commuting operator  $\hat{\rho}_\mu$  in Eq. (4.13)

previously used for preparing the Slater determinant is generalized as follows to generate  $L$ -wise correlations,

$$\hat{\rho}_\mu^{(L)} = \prod_{r=1}^{\mu-1} \hat{Z}_{rL} \prod_{r=L(\mu-1)+1}^{\mu L} \hat{X}_r, \quad (4.16)$$

where here Pauli-Z subscript  $rL = r \cdot L$  refers to the qubit order. The modified operator  $\hat{\rho}_\mu^{(L)}$  has  $L$  Pauli-X terms and  $\mu$  Pauli-Z terms with modulo  $L$  indexes such that  $\hat{\rho}_\mu^{(L)}$  remains anti-commuting, as shown in Appendix A.2,

$$\{\hat{\rho}_\mu^{(L)}, \hat{\rho}_\mu^{(L)}\} = 2^{-\mu} \mathbf{I}. \quad (4.17)$$

For example, the  $L = 2$  pairwise correlated anti-commuting operators are given as

$$\hat{\rho}_\mu^{(2)} = \hat{Z}_2 \hat{Z}_4 \hat{Z}_6 \dots \hat{Z}_{2\mu-2} \hat{X}_{2\mu-1} \hat{X}_{2\mu}. \quad (4.18)$$

Thus, an  $N$  mode  $d$ -occupied  $L$ -wise correlated state  $|\Psi_L\rangle$  can be prepared by applying multiple  $L$ -wise Clifford loaders  $\hat{C}_L(G_l)$ , for  $l = 1, \dots, \frac{d}{L}$ , that is

$$|\Psi_L(\mathbf{G})\rangle = \prod_{l=1}^{\frac{d}{L}} \hat{C}_L(G_l) |\text{vac}\rangle, \quad (4.19)$$

where  $\mathbf{G}$  is a  $\frac{N}{L} \times \frac{d}{L}$  orthonormal matrix,  $G_l$  is a column vector of  $\mathbf{G}$ , which simplifies to

$$|\Psi_L(\mathbf{G})\rangle = \frac{1}{\sqrt{\det(\mathbf{G}_B)}} |B_L\rangle, \quad (4.20)$$

up to an unobserved global phase, where the sum is over all combinations of the ordered set  $B$  containing  $\frac{d}{L}$  unique integers between 1 and  $\frac{N}{L}$ ,  $G_B$  is a  $\frac{d}{L} \times \frac{d}{L}$  matrix minor of  $G$  whose rows are restricted to  $B$ ,  $B_L = \{L(j-1)+1, L(j-1)+2, \dots, Lj \mid j \in B\}$ , and  $|B_L\rangle$  denotes an

$N$ -mode Fock state with occupied modes indexed by  $B_L$ , as shown in Appendix A.3.

The  $L$ -wise correlated ansatz state  $|\Psi_L\rangle$  in Eq. (4.20) is similar to the Slater determinant  $|\Psi_1\rangle$  from Eq. (4.15) in how the amplitudes are calculated, but differs in the Fock states that have non-zero amplitudes. In the Slater determinant case, all Fock states with  $d$  particle number will have non-zero amplitudes, while in the  $L = 2$  pairwise case, all Fock states that have both  $d$  particle number and  $(L=2)$ -tuple of neighboring occupations and neighboring vacants will have non-zero amplitudes. For instance, in the case  $N = 4$  and  $d = 2$ , Fock states  $\{|0011\rangle, |1100\rangle\}$  will have non-zero amplitudes, and  $\{|0101\rangle, |0110\rangle, |1010\rangle, |1001\rangle\}$  will have zero amplitudes. For the case  $N = 8$  and  $d = 4$ , Fock states  $\{|00001111\rangle, |00110011\rangle, |11000011\rangle, |00111100\rangle, |11001100\rangle, |11110000\rangle\}$  will have non-zero amplitudes, and all remaining Fock states will have zero amplitudes.

For a given normalized column  $G_l$ , a corresponding  $L$ -wise correlated Clifford loader is defined as

$$\hat{C}_L(G_l) = \hat{D}_L^\dagger(G_l) \hat{\rho}_1^{(L)} \hat{D}_L(G_l), \quad (4.21)$$

where the corresponding anti-commuting operator

$$\hat{\rho}_1^{(L)} = \prod_{r=1}^L \hat{X}_r, \quad (4.22)$$

consists of  $L$  Pauli X gates that acts on the first  $L$  qubits sandwiched two sets of multiple Givens rotations  $\hat{D}_L, \hat{D}_L^\dagger$ . Each  $\hat{D}_L$  is composed of Givens rotations gates

$$\hat{U}_\mu^{(L)}(\theta) = \exp(-i\theta \hat{\rho}_\mu^{(L)} \hat{\rho}^{(L)}), \quad (4.23)$$

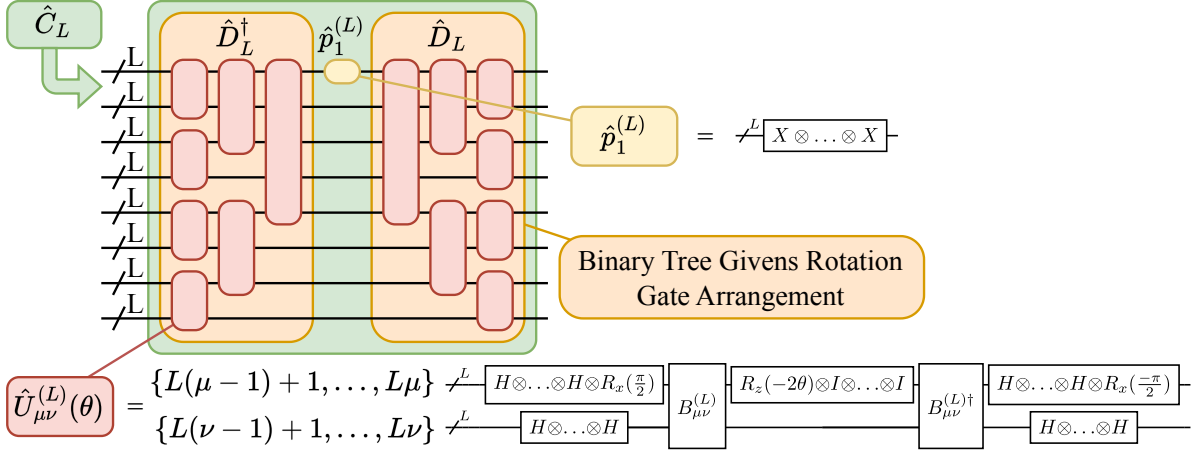


Figure 4.5:  $N = 8L$  qubit example of  $L$ -wise Clifford Loader  $\hat{C}_L$ . It consists of  $L$  Pauli X acting on the first  $L$  qubits sandwiched by two sets of multiple Givens rotations  $\hat{D}_L^\dagger$  and  $\hat{D}_L$ , where the Givens rotations  $\hat{U}_{\mu\nu}^{(L)}$  are arranged in a binary tree arrangement. Each  $\hat{U}_{\mu\nu}^{(L)}$  is decomposed using Pauli rotation gates  $R_x$  that acts on qubit  $L\mu$ ,  $R_z$  that act on qubit  $L(\mu-1)+1$ , Hadamards  $H$  and CNOT ladders  $B_{\mu\nu}^{(L)}$  that act on all  $2L-1$  qubits in  $\{L(\mu-1)+1, \dots, L\mu-1\}$  and  $\{L(\mu-1)+1, \dots, L\}$ , with  $B_{\mu\nu}^{(L)}$  also acting on  $-\mu$  additional qubits in  $\{L\mu, L(\mu+1), L(\mu+2), \dots, L(\mu-1)\}$ .  $\theta$  is a rotation angle.

arranged in a similar binary tree pattern as shown in Fig. 4.5. Since the Givens rotation gate  $\hat{U}_{\mu\nu}^{(L)}(\theta)$  is a Pauli-string rotation gate, its gate decomposition [241] and the corresponding rotation angle can be obtained in a similar fashion as in the Slater determinant case. The explicit form of the Givens Rotation in terms of Pauli operators is detailed in Appendix A.4.

#### 4.2.4 Resource Analysis

For simplicity, all types of two-qubit gates depths are treated as equal and no circuit compilation is assumed. To prepare the  $L$ -wise correlated ansatz state  $|\Psi_L\rangle$  on a quantum computer under Jordan-Wigner mapping,  $\frac{d}{L}$  Clifford loaders  $\hat{C}_L$  are applied on an all-zero qubit state  $|0\rangle$ . Each Clifford loader  $\hat{C}_L$  has two sets of multiple Givens rotation  $\hat{D}_L$  and  $\hat{D}_L^\dagger$ . Each  $\hat{D}_L$  has  $\log_2 \frac{N}{L}$  Givens rotation gate depth. Each Givens rotation gate  $\hat{U}_{\mu\nu}^{(L)}$  contains two CNOT ladders  $B_{\mu\nu}^{(L)}$  that act on all  $2L + \mu - 1$  qubits in  $\{L(\mu-1)+1, \dots, L\mu\}$ ,  $\{L(\mu+1), L(\mu+2), \dots, L(\mu-1)\}$

and  $\{L(\mu - 1) + 1, \dots, L\}$ . Here, each CNOT ladder  $B_\mu^{(L)}$  uses the logarithmic-depth CNOT ladders, as shown in Fig. 4.4, which has a two-qubit gate depth of

$$\log_2(2L + \mu - 1) = O(\log_2 N). \quad (4.24)$$

Focusing on all Givens rotations  $\hat{U}_{1,2^s}^{(L)}$  that act on the first qubit in every sublayer  $s = 1, 2, \dots, \log_2 \frac{N}{L}$ , as shown in Fig. 4.5, the overall two-qubit gate depth of the quantum circuit required to prepare  $L$ -wise correlated ansatz state  $|\Psi_L\rangle$  is estimated to be,

$$\begin{aligned} & \frac{2d}{L} \sum_{s=1}^{\log_2 \frac{N}{L}} 2 \log_2(2L + 2^s - 1 - 1) \\ & \frac{4d}{L} \sum_{s=1}^{\log_2 \frac{N}{L}} \log_2(2^{s+\log_2(L)}) \end{aligned} \quad (4.25)$$

$$= \frac{4d}{L} \sum_{s=1}^{\log_2 \frac{N}{L}} (s + \log_2(L)) \quad (4.26)$$

$$= \frac{2d}{L} \log_2^2 \frac{N}{L} + (1 + 2 \log_2 L) \log_2 \frac{N}{L} \quad (4.27)$$

$$= O\left(\frac{d}{L} \log_2^2 \frac{N}{L}\right). \quad (4.28)$$

This shows that the proposed Clifford ladder approach to prepare a  $L$ -wise correlated ansatz state  $|\Psi_L\rangle$  is shallower than a Slater determinant  $|\Psi_1\rangle$  by at least a factor of  $L$ , *ceteris paribus*.

The estimated two-qubit gate depth per occupied mode for Slater determinants  $|\Psi_1\rangle$  and pairwise correlated ansatz states  $|\Psi_2\rangle$  on a quantum computer is plotted in Fig. 4.6, and compared against the previous linear depth approach of preparing  $d = 2, 16$  and 128-occupied Slater determinants, which has a  $d$ -independent two-qubit gate depth of about  $2N$  [157, 171, 172].

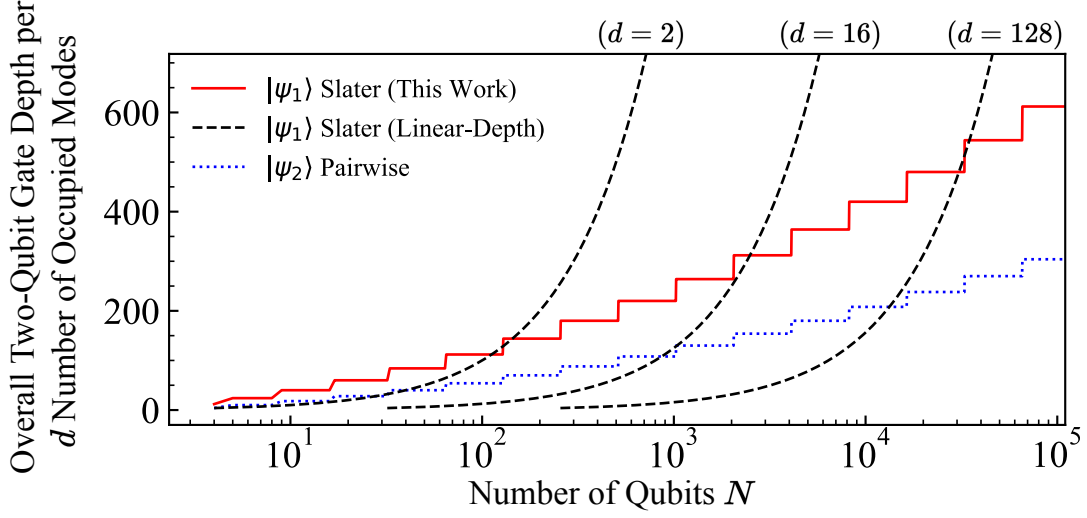


Figure 4.6: Estimated two-qubit gate depth per occupied mode  $d$  to prepare an  $N$  mode Slater determinant  $|\Psi_1\rangle$  and an  $L=2$  pairwise correlated ansatz state  $|\Psi_2\rangle$  using Clifford loaders compared to existing  $d$ -independent linear-depth approaches.

Indeed, the crossover point  $d \sim \frac{N}{\log_2 N}$  shows that the minimum number of qubits  $N$  required to achieve a shallower circuit increases sub-exponentially with the number of occupied modes  $d$ . However, this crossover point can be practically surpassed by near-term quantum devices such as superconducting qubits [261] and trapped-ions [37] with less than  $10^5$  qubits for systems with  $2 \leq d \leq 128$  occupied fermionic modes, which is a sizable range that encompasses many systems of interest in quantum chemistry and condensed matter physics. In general, the Clifford loader approach is suitable for problems classes that have a sufficiently slow growing  $d \sim O\left(\frac{N}{\log_2 N}\right)$ . One such problem is computation of quantum observable quantities for fermionic systems for the complete basis set limit, where  $d$  is preserved, but said quantities are computed for increasing values of  $N$  and extrapolated using various schemes to very large limits of  $N$  [262–264].

### 4.2.5 Example and Results

To validate the  $L = 2$  pairwise correlated ansatz state, the ansatz is variationally optimized to generate the best approximation to the exact ground state of three linear hydrogen molecular chains ( $\text{H}_2$ ,  $\text{H}_4$  and  $\text{H}_6$ ) with ( $d = 2, 4, 6$ ) electrons at a fixed interatomic distance of 1.4 bohr, where pairwise electronic correlation is likely to be significant. After ansatz optimization, the fraction of the electronic correlation energy  $E_{\text{pair}}/E_{\text{corr}}$  captured by the optimized pairwise correlated ansatz state  $|\Psi_2(\mathbf{G})\rangle$  is then numerically evaluated.  $E_{\text{pair}} = E_{\text{HF}} - \hat{H}_e$  is the correlation energy beyond the mean-field energy  $E_{\text{HF}}$  of a molecule captured by  $|\Psi_2(\mathbf{G})\rangle$ , while  $E_{\text{corr}} = E_{\text{HF}} - E_{\text{FCI}}$  is the exact value of the correlation energy, where  $E_{\text{FCI}}$  is known as the full configuration interaction (FCI) energy.  $\mathbf{G}$  is an optimized parameter matrix, obtained using a classical quasi-Newton L-BFGS-B optimizer that minimizes the expectation of the electronic Hamiltonian  $\hat{H}_e$ .

Different mixtures of atomic basis sets [186] are considered in this demonstration, (STO-3G, 6-31G, 6-311G, cc-pVDZ, aug-cc-pVDZ) for each hydrogen atom, resulting in system sizes ranging from 4 to 20 qubits. Such mixing of basis sets for each atom is a common strategy in computational quantum chemistry to reduce the resources required to achieve a desired precision [265]. All calculations were performed numerically using SciPy [242], PYSCF [266] and PennyLane [267]. Fig. 4.7 shows that a large fraction of the electronic correlation energy  $E_{\text{pair}}/E_{\text{corr}}$  is captured by the optimized pairwise correlated ansatz state  $|\Psi_2(\mathbf{G})\rangle$ .

## 4.3 Summary and Outlook

We have proposed Givens rotation-based Clifford loaders for efficient preparation of  $d$ -occupied Slater determinants  $|\Psi_1\rangle$  of  $N$  modes using shallower  $O(d \log_2^2 N)$  two-qubit gate depth quantum

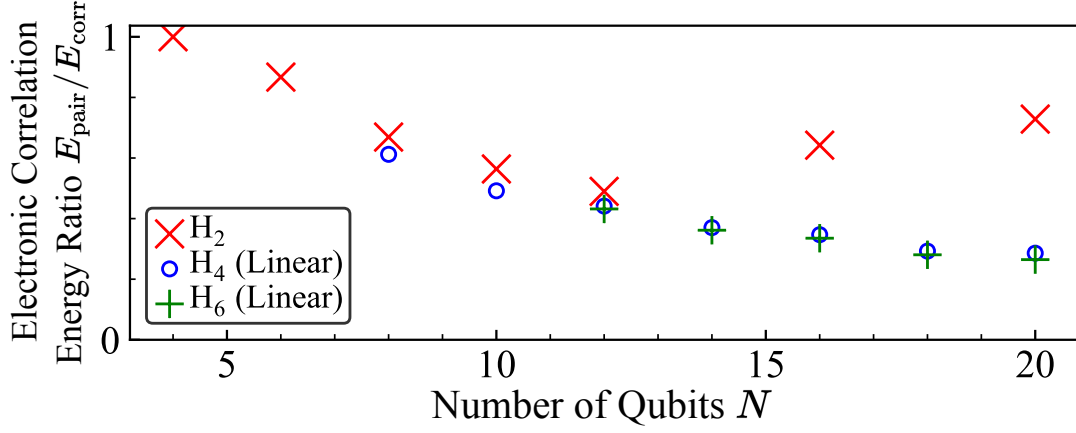


Figure 4.7: Numerically calculated fraction of the electronic correlation energy ratio  $E_{\text{pair}}/E_{\text{corr}}$  captured by an optimized pairwise correlated ansatz state for hydrogen chains up to  $H_6$  at fixed interatomic distance of 1.4 bohr for various basis set mixtures up to 20 qubits. The plot shows that significant amount of correlation is captured by the pairwise correlated state despite having a circuit depth that is half of a Slater determinant.

circuits. We have also showed that by redefining new sets of the anti-commutation operators  $\hat{\rho}_\mu$  for the Clifford loaders, the same technique can be extended prepare  $L$ -wise correlated ansatz states  $|\Psi_L\rangle$ . This yields shallower quantum circuits than that of Slater determinants by at least a factor of  $L$ .

As demonstrated in the application of  $L = 2$  pairwise correlated ansatz states to hydrogen chains,  $L$ -wise correlated states are potentially useful in fermionic systems with significant  $L$ -wise fermionic correlation, even though it is not expected to fully capture all the correlation energy. It will be interesting to generalize the Clifford loaders to other types of fermionic correlation while keeping the same shallow gate depth scaling intact. The other interesting future research direction would be consider extending the Clifford loaders method to imbue all types fermionic correlations so as to generate the Full Configuration Interaction (FCI) wavefunction, as introduced in Section 3.2.2. While the expected circuit depth would be exponential in the system size, new approaches of systematically capturing various types of

correlations would be of great value in correlated fermionic state preparation.

The Clifford loader approach to fermionic ansatz state preparation offers an subexponential improvement in gate depth over the existing methods. This includes the fermionic basis transformation in preparing Slater determinants and the UCC ansatz approach in preparing  $L$ -wise correlated ansatz states for problem cases with  $d = O\left(\frac{N}{\log_2 N}\right)$  number of occupied modes. Nonetheless, the results have established Clifford loaders via Givens rotations as an efficient, yet practical and scalable fermionic ansatz state preparation technique, which will enable the study of molecules and materials requiring larger basis set sizes on near-term quantum devices.

## Chapter 5

# Resource-Efficient

# Quantum-Assisted Simulation for

# Quantum Dynamics

This chapter adapts the material published in:

- C. H. Chee, D. Leykam, A. M. Mak, K. Bharti, and D. G. Angelakis, *Resource-Efficient Hybrid Quantum-Classical Simulation Algorithm*, 2024, [arXiv:2405.10528](#).

### 5.1 Introduction

Consider a quantum chemical system characterized by a time-independent Hamiltonian  $\hat{H}$ , initially in an unknown state  $|\psi_0\rangle$ , with an observable  $\hat{O}$  representing the physical quantity of interest. The goal is to compute the dynamical expectation value of the observable  $\hat{O}$  at fixed

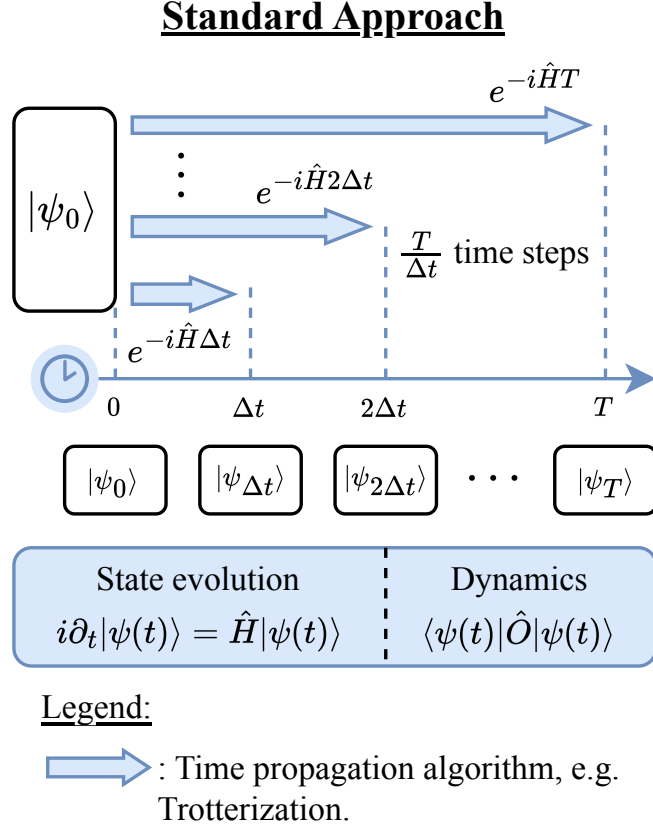


Figure 5.1: Standard method that uses quantum time-propagation algorithms to simulate the quantum dynamics of a system of Hamiltonian  $\hat{H}$ , initialized in  $|\psi_0\rangle$ , up to a time  $T$ , measured by an observable  $\hat{O}$  at fixed time intervals  $\Delta t$ . It requires preparation of multiple copies of time-evolved states and measuring each with the observable for every intermediate time step. This can result in a significant computation bottleneck at larger number of time steps.

time intervals  $\Delta t$  over a total simulation time  $T$ . A standard approach of using a quantum computer for this task involves preparing multiple copies of the initial state and evolve these copies  $|\psi_0\rangle$  using quantum time-propagators for various amounts of time, and subsequently measuring them with the observable  $\hat{O}$  as depicted in Fig. 5.1.

Whilst the time propagation of the quantum states is a crucial aspect to quantum dynamics, the equally important task of extracting desired properties of these quantum states at intermediate times is often overlooked. It is important to highlight that the standard approach shown in Fig. 5.1 faces a significant computational bottleneck. This arises due the

phenomenon of wavefunction collapse upon measurement [191] and constraints imposed by the no-fast-forwarding theorem, which prevents evolved states from being prepared faster than their actual simulation time [9, 192]. Consequently, simulating dynamics with long durations or rapid oscillations becomes computationally demanding, as it typically requires more frequent intermediate time-step measurements. Therefore, there is a pressing need for resource-efficient quantum simulators for quantum dynamics.

To address the computational bottleneck associated with the increasing number of measurements, it is worth exploring algorithms from the Noisy Intermediate-Scale Quantum (NISQ) era, which are specifically designed to make prudent use of quantum resources so as to minimize quantum noise effects [66, 168]. Presently, most NISQ algorithms utilize a hybrid quantum-classical framework to simulate quantum dynamics. This approach strategically distributes computational tasks between quantum and classical devices, with the latter handling the bulk of the computational burden. The proposed quantum algorithm in the chapter adheres to this model. However, before detailing the specifics of the proposed algorithm, it is informative to examine existing approaches for quantum time-propagation. Section 5.2.1 describes standard approaches termed as Hamiltonian Simulation. Section 5.2.2 describes Variational Quantum Simulator which is a hybrid quantum-classical approach that is compatible on NISQ devices. Finally, Section 5.2.3 describes Quantum-Assisted Simulator which is an alternative hybrid approach that inspired the main work of this chapter.

## 5.2 Existing Approaches for Quantum Time-Propagation

### 5.2.1 Hamiltonian Simulation

Hamiltonian simulation aims to propagate an input wavefunction with a quantum circuit  $\hat{U}$  that approximates the quantum time propagator  $e^{-i\hat{H}t}$  with an error  $\epsilon$ , such that  $\|\hat{U} - e^{-i\hat{H}t}\| \leq \epsilon$  [8]. It offers a provable exponential speedup over its classical counterparts, provided that the Hamiltonian involves only local interactions [8]. In this context, the Hamiltonian  $\hat{H}$  is expressed as a sum of  $L$  local Hamiltonians  $\hat{H}_j$  where each  $\hat{H}_j$  act on a few qubits,

$$\hat{H} = \sum_j^L \hat{H}_j. \quad (5.1)$$

The simplest approach to Hamiltonian simulation is through the first-order Trotter-Suzuki product decomposition [8, 9, 120–122, 124], where the time propagator can be approximated as a product sequence [123, 268],

$$\hat{U} = \prod_j^L e^{-it\hat{H}_j} + O\left(\sum_{j>k}^L [\hat{H}_j, \hat{H}_k] t^2\right), \quad (5.2)$$

where  $t = T/\tau$  and  $\tau$  is the trotter number. As a result, the overall quantum circuit gate depth scales  $O(L^3 T^2 \tau^{-1})$  where  $T$  is the maximum effective local evolution time. For a Hamiltonian with an arbitrary structure, that is  $L = O(\exp(N))$  where  $N$  is the total number of qubits, an exponential quantum circuit depth would be required to simulate the quantum time propagator  $e^{-i\hat{H}t}$  [8]. However, most Hamiltonians of interest, including the electronic Hamiltonian, contain finite and well-defined structures such that  $L = O(\text{Poly}(N))$ . Thus, the overall quantum runtime becomes polynomial in the quantum system size  $N$ , total simulation  $T$  and error  $\epsilon^{-1}$ , offering

an exponential speedup in quantum time evolution tasks over its classical counterparts [12, 126, 129, 269]. As a result, exact quantum time evolution of electronic states are more efficient on quantum computer than classical mean-field methods such as real-time time-dependent Hartree-fock [135]. Other approaches of Hamiltonian simulation includes the Split-Operator method [125–127], linear combination of unitaries [128, 129], quantum walks [130, 131], quantum signal processing [132], qubitization [133], stochastic quantum simulation [270–272] and time-dependent quantum simulation in the interaction picture [273–276].

Despite the exponential speedup, Hamiltonian simulation remains prohibitive on NISQ devices for many-body interacting systems due to the need for deep entangling quantum circuits that scales polynomially with system size. To address this challenge, various approaches have been explored to reduce the quantum circuit depth down to manageable levels. This include using efficient fermion-to-qubit mapping to reduce the number of qubits involved in each local simulations [277] and employing shallow-depth parameter circuit ansatz for the evolved wavefunction in Variational Quantum Simulator, as described in the following subsection.

### 5.2.2 Variational Quantum Simulator

The Variational Quantum Simulator (VQS) is a hybrid algorithm designed for simulating Time-Dependent Schrödinger Equation (TDSE) in the NISQ era [160–166, 278]. It aims to approximate the time-evolution state  $|\psi(t)\rangle = U(t)|\psi(0)\rangle$  as a parameterized quantum circuit ansatz with a predetermined set of quantum gates  $\{\hat{U}_j\}$ ,

$$|\psi(t)\rangle = \prod_j \hat{U}_j(\theta_j(t)) |\psi(0)\rangle, \quad (5.3)$$

so that the TDSE can be approximated as

$$i \frac{d}{dt} |\psi(t)\rangle = \hat{H} |\psi(t)\rangle. \quad (5.4)$$

The approximated TDSE in Eq. 5.4 can be reduced to a set of dynamical equations in terms of parameters  $\theta(t)$  based on dynamical variational principles. One may consider the McLachlan's variational principle [279] which states that the quantum time-evolution always minimizes the square root state error overlap or the state norm of the difference between the left-hand and right-hand sides of the approximated TDSE in Eq. (5.4). This implies that the variation of state norm with respect to parameters is always zero, that is,

$$\langle (i \frac{d}{dt} - \hat{H}) \psi(t) | \psi(t) \rangle = 0. \quad (5.5)$$

Evaluating Eq. (5.5) would result in the following dynamical matrix equation,

$$\dot{\mathbf{A}} = \mathbf{C}, \quad (5.6)$$

where the elements of matrices  $\mathbf{A}$  and  $\mathbf{C}$  are given by,

$$A_{jk} = \text{Re} \left[ \frac{\langle \psi | \frac{d}{dt} \psi \rangle}{j} \frac{\langle \psi | \psi \rangle}{k} + \frac{\langle \psi | \psi \rangle}{j} \frac{\langle \psi | \frac{d}{dt} \psi \rangle}{k} \right], \quad (5.7)$$

$$C_k = \text{Im} \left[ \frac{\langle \psi | \frac{d}{dt} H \psi \rangle}{k} + \frac{\langle \psi | \frac{d}{dt} \psi \rangle}{k} H \right], \quad (5.8)$$

which consists of expectation values and quantum state overlaps that can be efficiently estimated on near-term quantum devices [280]. The classical computer will store and solve the dynamics of the ansatz parameters in Eq. (5.6) using ODE solvers.

However, energy conservation for a time-independent Hamiltonian is not always guaranteed in VQS with McLachlan or any other dynamical variational principles, such as state fidelity. The necessary and sufficient condition for energy conservation in VQS is that the ansatz subspace must encompass the entire time-evolution Hilbert subspace — the subset of the full quantum Hilbert space that encompasses all possible time-evolved states. Unfortunately, circuit ansatzes are typically optimized for NISQ devices to reduce noise, resulting in some, but not all, time-evolution states being effectively represented. As a result, the VQS approach may not always uphold energy conservation, thus leading to potentially inaccurate simulations. Furthermore, the VQS method does not eliminate the previously highlighted bottleneck, as it still requires the preparation of multiple copies of ansatz at different intermediate times steps so as to evaluate the quantum dynamics.

### 5.2.3 Quantum-Assisted Simulator

Quantum-Assisted Simulator (QAS) is another hybrid quantum-classical NISQ algorithm that adapts the VQS approach to simulate the TDSE while attempting to overcome this bottleneck [281, 282]. Here, QAS assumes a time-evolution ansatz  $|\psi(t)\rangle$  as a complex linear combination of  $n_{\text{basis}}$  basis states  $\{ |j\rangle \mid j = 0, 1, \dots, n_{\text{basis}} - 1 \}$  that is,

$$|\psi(t)\rangle = \sum_{j=0}^{n_{\text{basis}}-1} c_j(t) |j\rangle, \quad (5.9)$$

where the initial system state  $|\psi_0\rangle$  is part of the basis set. This allows the initial linear coefficients to be simply written as  $c_j(t=0) = (1, 0, \dots, 0)$ , thereby avoiding the need for expensive initial state tomography. To ensure an accurate simulation and guarantee energy conservation, it is necessary for the basis states  $\{ |j\rangle \}$  to be linearly independent and to span the entire time-

evolution Hilbert subspace.

Similar to the VQS approach, the corresponding dynamical equation can be obtained by applying McLachlan's dynamical variational principle in Eq. (5.5) and substituting the ansatz from Eq. (5.9),

$$\dot{\mathbf{F}} = -i\mathbf{H} \mathbf{F}, \quad (5.10)$$

where the elements of the matrices  $\mathbf{F}$  and  $\mathbf{H}$  are the basis state overlap  $F_{jk}$  and Hamiltonian matrix  $H_{jk}$ , respectively,

$$F_{jk} = \langle j | k \rangle, \quad (5.11)$$

$$H_{jk} = \langle j | \hat{H} | k \rangle. \quad (5.12)$$

The full derivation of parameter evolution in Eq. (5.10) can be found in the end of this section in page 100.

By using the quantum computer solely to calculate basis state overlaps  $\mathbf{F}$ , Hamiltonian elements  $\mathbf{H}$  in Eqs. (5.11), (5.12), respectively and the observable elements

$$O_{jk} = \langle j | \hat{O} | k \rangle, \quad (5.13)$$

one can bypass the computational bottleneck associated with preparing and measuring multiple copies of the time-evolved quantum states for every intermediate time step. The dynamical properties of the quantum state are then computed classically using the determined observable

elements  $O_{jk}$  and the evolved linear coefficients  $\{c_j(t)\}$ ,

$$\langle \psi(t) | \hat{O} | \psi(t) \rangle = \sum_{j,k=0}^{n_{\text{basis}}-1} c_j(t) O_{jk} c_k(t). \quad (5.14)$$

Hence, QAS can be summarized in four steps:

1. Choose a suitable basis set that includes the initial state for the simulation.
2. Use a quantum computer to estimate basis state overlap  $F$  in Eq. (5.11), Hamiltonian matrix  $H$  in Eq. (5.12), and the observable matrix  $O$  in Eq. (5.13). This can be done using a variety of quantum subroutines such as the Hadamard Test [236] or the projective measurements-based protocol [280].
3. Use a classical computer to solve the complex dynamical equations in Eq. (5.10) using a complex ordinary differential equation (ODE) solver to obtain the dynamics of the linear coefficients  $c_j(t)$ .
4. Estimate the expectation value of observable  $\hat{O}$  in Eq. (5.14) at fixed time intervals  $\Delta t$  up to a simulation time  $T$  to solve the quantum dynamics,

Both the VQS and QAS leverage dynamical variational principles for simulation, avoiding the use of quantum variational optimization subroutines [168]. This approach avoids the barren plateau problem [180, 181] by eliminating the need to estimate the variational landscape [281, 282]. Unlike other VQS methods, QAS can ensure energy conservation in simulations with time-independent Hamiltonians by selecting an appropriate basis set.

However, in the original formulation of the QAS algorithm, the chosen basis states are derived from applying different single Pauli-string operators, generated from the Pauli Hamiltonian terms, into the initial state [281], which often leads to linear dependency. This results in an exponential growth in the basis set size, as it becomes unnecessarily large to span the entire time-evolution quantum Hilbert subspace [281, 283, 284]. Consequently, the original approach to QAS becomes impractically inefficient for both quantum and classical computers.

### Derivation of Parameter Evolution

This section presents the derivation of the parameter evolution in Eq. (5.10), adapted from Bharti and Haug [281], and Yuan et al. [160]. The McLachlan's variational principle [279] states that the quantum time-evolution always minimizes the square root error overlap between the left and right hand side states of the Schrödinger equation,

$$\langle \tilde{\psi}(t) | \hat{H} | \psi(t) \rangle - E(t) \langle \tilde{\psi}(t) | \psi(t) \rangle = 0, \quad (5.15)$$

$$\langle \tilde{\psi}(t) | \hat{H} | \psi(t) \rangle = E(t) \langle \tilde{\psi}(t) | \psi(t) \rangle. \quad (5.16)$$

Substituting the time-evolution ansatz in Eq. (5.9), the error overlap is evaluated to be,

$$\langle \tilde{\psi}(t) | \hat{H} | \psi(t) \rangle - E(t) \langle \tilde{\psi}(t) | \psi(t) \rangle \quad (5.17)$$

$$\begin{aligned} &= \sum_{j,k=0}^{n_{\text{basis}}-1} \langle \tilde{\psi}_j(t) | \hat{H} | \psi_k(t) \rangle \langle \tilde{\psi}_j | \psi_k \rangle + i \sum_{j=0}^{n_{\text{basis}}-1} \langle \tilde{\psi}_j(t) | \hat{H} | \psi_j(t) \rangle \langle \tilde{\psi}_j | \psi_j \rangle \\ &\quad - i \sum_{k=0}^{n_{\text{basis}}-1} \langle \tilde{\psi}_k(t) | \hat{H} | \psi_k(t) \rangle \langle \tilde{\psi}_k | \psi_k \rangle + \langle \tilde{\psi}(t) | \hat{H}^2 | \psi(t) \rangle - E(t)^2 \langle \tilde{\psi}(t) | \psi(t) \rangle. \end{aligned} \quad (5.18)$$

Since,

$$\langle \tilde{\psi}_j | \psi_j \rangle = \langle \tilde{\psi}_j | \psi_j \rangle, \quad (5.19)$$

the error overlap in Eq. (5.18) simplifies to

$$\begin{aligned}
 &= \sum_{j,k=0}^{n_{\text{basis}}-1} \langle j | \dot{\rho}_k \rangle + i \sum_{j=0}^{n_{\text{basis}}-1} \langle j | \hat{H} | \rho \rangle_j \\
 &\quad - i \sum_{k=0}^{n_{\text{basis}}-1} \langle \rho | \hat{H} | k \rangle + \langle \rho | \hat{H}^2 | \rho \rangle
 \end{aligned} \tag{5.20}$$

$$= \dot{F} - i \dot{H} + i H + \langle H^2 \rangle, \tag{5.21}$$

where  $F$  and  $H$  represents the overlap and Hamiltonian matrices with elements given in Eqs. (5.11) and (5.12), respectively,  $(H^2)$  represents the squared Hamiltonian matrix with elements

$$(H^2)_{jk} = \langle j | \hat{H}^2 | k \rangle. \tag{5.22}$$

As the variation of the square root error overlap is equivalent to the variation of the error overlap up to a constant factor, we may focus on variation of the error overlap instead, then we have

$$\begin{aligned}
 \dot{\rho}_k &= \sum_{j=0}^{n_{\text{basis}}-1} \left[ \langle j | \rho \rangle \langle j | \dot{\rho}_k \rangle + i \left[ \langle j | \rho \rangle \langle j | \hat{H} | \rho \rangle - \langle \rho | \hat{H} | j \rangle \langle j | \rho \rangle \right] \right] \\
 &\quad + \sum_{j=0}^{n_{\text{basis}}-1} \left[ \langle j | \rho \rangle \langle j | \dot{\rho}_k \rangle - i \left[ \langle j | \rho \rangle \langle j | \hat{H} | \rho \rangle - \langle \rho | \hat{H} | j \rangle \langle j | \rho \rangle \right] \right]
 \end{aligned} \tag{5.23}$$

$$= (\dot{F} + iH) \rho_k + (\dot{F} - iH) \rho_k. \tag{5.24}$$

Thus, by setting the variation in Eq. (5.24) to zero, the parameter evolution is derived to be

$$\dot{F} = -iH, \tag{5.25}$$

which minimizes the error overlap in Eq.(5.21) throughout the entire evolution,

$$\min = \langle \cdot | H^2 | \cdot \rangle - \langle \cdot | F | \cdot \rangle. \quad (5.26)$$

## 5.3 Resource-Efficient Quantum-Assisted Simulation

### 5.3.1 Idea: Linear Combinations of Time-Evolved States

This section shall demonstrate how QAS can be modified to leverage the strengths of both quantum and classical computations by complementing existing quantum time propagation algorithms to improve the efficiency of simulating quantum dynamics on FTQC devices. Consider a system of size  $N$  initialized in an unknown superposition of  $n$  non-degenerate eigenstates  $|e_j\rangle$ , where  $n$  is defined as the number of eigenstates that span the time-evolution subspace of the quantum system, and assuming  $n \ll 2^N$ ,

$$|0\rangle = \sum_{j=0}^{n-1} |e_j\rangle. \quad (5.27)$$

Suppose the time-evolved states  $|j\rangle$  are chosen as a basis,

$$|j\rangle = e^{-iHs_j} |0\rangle, \quad (5.28)$$

where  $s_j$  are parameter times which are not exceeding the total simulation time  $T$ ,  $0 = s_0 < s_1 < \dots < s_{n_{\text{basis}}-1} \leq T$ , as shown in Fig 5.2.

By selecting just  $n_{\text{basis}} = n$  linearly independent time-evolved basis states, the time-evolution Hilbert subspace can be fully spanned. While the FTQC device handles the basis

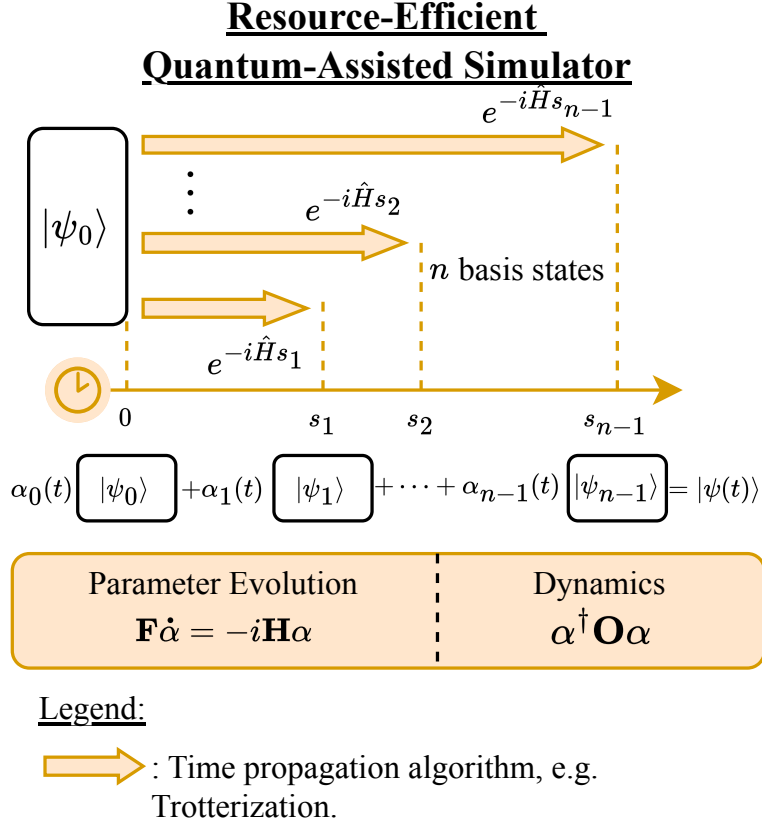


Figure 5.2: Our proposal to modify Quantum-Assisted Simulator (QAS) to complement quantum time propagation algorithms to efficiently simulate quantum dynamics. QAS assumes a time evolution state  $|\psi(t)\rangle$  as a linear combination of time-evolved states. Here the quantum computer is required to estimate the basis overlap  $\mathbf{F}$ , Hamiltonian  $\mathbf{H}$  and observable  $\mathbf{O}$  matrix, while the classical computer solves parameter evolution and computes the dynamics numerically.

states, each having a dimensionality of  $2^N$ , the classical computer is tasked with storing and updating merely  $n_{\text{basis}} = n$  linear coefficients. If there are fewer time-evolved basis states than  $n$ , that is  $n_{\text{basis}} < n$ , the time-evolution ansatz is under-parameterized, leading to incorrect results. On the other hand, if the number of basis states is much larger than  $n$ , that is  $n_{\text{basis}} > n$ , the ansatz becomes over-parameterized which may lead to numerical convergence issues. Crucially, the system eigenvalues, eigenstates  $|e_j\rangle$ , and the linear coefficients  $c_j$  in the initial state in Eq. (5.27) remain unknown and do not need to be explicitly determined. This means that, when  $n \ll 2^N$  is small, the QAS approach overcomes the bottleneck in the standard approach

associated with preparing multiple copies of the time-evolved state at different time steps for dynamical measurements, while avoiding any exponential complexity arising from large basis sets. Therefore, the modified QAS offers better efficiency in simulating large  $N$  system sizes, allowing for a greater number of time steps to be simulated compared to most existing hybrid quantum simulation algorithms.

### 5.3.2 Resource Analysis

For a  $2N$ -qubit quantum device, the modified QAS is expected to consume fewer quantum resources than the standard method when the number of time steps exceeds roughly  $100n^2$ . To derive this efficiency gain, several key quantities and quantum subroutines employed will be delineated. For simplicity, assume the system Hamiltonian  $\hat{H}$  and observable  $\hat{O}$  both decompose into a linear combination of  $L$  number of Pauli strings  $\hat{P}_l = \sum_{j=1}^N \hat{\alpha}_j$ , where  $\hat{\alpha}_j \in \{\hat{I}_j, \hat{X}_j, \hat{Y}_j, \hat{Z}_j\}$  which may or may not share the same Pauli string. In this setting, the estimation of the basis state overlap  $F$ , Hamiltonian  $H$  and observable  $O$  matrices requires the estimation of the following quantities

$$F_{jk} = \langle 0 | e^{i\hat{H} s_{jk}} | 0 \rangle, \quad (5.29)$$

$$P_{jkl} = \langle 0 | \hat{P}_l e^{i\hat{H} s_{jk}} | 0 \rangle, \quad (5.30)$$

where  $\Delta s_{jk} = s_j - s_k$  parameterizes the differences in the evolution times of the basis states.

Consider the Hadamard Test quantum subroutine, with the time propagator  $\hat{U} = e^{-i\hat{H} t}$  with a fixed time duration  $\Delta t$ , which can evaluate the quantities,  $F_{jk}$  and  $P_{jkl}$  in Eqs. (5.29) and (5.30), respectively. The ancilla-controlled- $\hat{U}$  in the Hadamard Test would have a longer quantum runtime complexity than the standard  $\hat{U}$ , but only by a constant multiple factor [285].

With access to a  $2N$ -qubit quantum computer, a modified Hadamard test with  $N$  ancilla qubits, instead of just one ancilla qubit, can be employed. So that, the controlled-quantum gates in the controlled- $\hat{U}$  that act on separate sets of systems qubits can remain parallel if controlled by separate ancilla qubits [285]. Detailed information on this modified Hadamard Test is provided in Appendix B.1. In the worst case scenario, given that all times  $S_j$  are not more than the total simulation time  $T$ , all modified Hadamard tests would have a maximum  $\frac{T}{\Delta t}$  number of ancilla controlled- $\hat{U}$ s. As there is a combined total of  $O(Ln^2)$  of quantities,  $F_{jk}$  and  $P_{jkl}$ , there are  $O(Ln^2)$  number of Hadamard Test subroutines to estimate all the required quantities in Eqs. (5.29) and (5.30). Therefore, the total overall quantum runtime complexity is

$$O \left( \frac{T}{\Delta t} L n^2 \text{Poly}(L, n^{-1}, \Delta t) \right) \quad (5.31)$$

where  $\text{Poly}(L, n^{-1}, \Delta t)$  is the quantum runtime complexity of  $\hat{U}$  and  $\|e^{i\hat{H}t} - \hat{U}\|$  is the time evolution error.

Conversely, the standard method involves preparing  $L$  copies of time-evolved states and measuring each with the corresponding Pauli strings, decomposed from the observable, for every intermediate time step. Thus, this requires  $O \left( L \left( \frac{T}{\Delta t} \right)^2 \right)$  repetitions of  $\hat{U}$  to estimate the expectation value of the observable  $\hat{O}$ . Thus, the overall quantum runtime complexity to run the standard method is

$$O \left( L \left( \frac{T}{\Delta t} \right)^2 \text{Poly}(L, n^{-1}, \Delta t) \right) . \quad (5.32)$$

Hence, by comparing (5.31) and (5.32), QAS is expected to consume fewer quantum resources than the standard method in terms of overall quantum runtime complexity, when the number

of time steps exceeds

$$\frac{T}{\Delta t} \ll 16 n^2. \quad (5.33)$$

Assuming  $n \ll 6$ , based on the general observation that a 3-qubit Toffoli gate can be decomposed into at least 6 CNOT gates [29, 286], the threshold is approximated to be

$$\frac{T}{\Delta t} \ll 100n^2. \quad (5.34)$$

The full derivation of this claim is available in Appendix B.2.

After populating the basis state overlap  $F$ , Hamiltonian  $H$  matrices, the complex linear dynamical equation in Eq. (5.10) is solved on a classical computer using a complex ODE solver with an  $O\left(\frac{Tn^3}{\tau}\right)$  classical runtime complexity. Although QAS is computationally inefficient when  $n \sim O(2^N)$ , it becomes efficient when  $n \ll 2^N$  is small, avoiding any exponential classical runtime or memory scaling. Therefore, while QAS is unsuitable for simulating the time-evolution of a system with arbitrary state initialization, it can be useful when simulating large systems initialized in a superposition of a low number of eigenstates  $n$  with a large number of time steps that exceeding  $100n^2$ .

### 5.3.3 Examples and Results

Two examples are provided to demonstrate the modified QAS approach in the context of quantum chemistry: the orbital population dynamics of a Helium (He) atom and a hydrogen ( $H_2$ ) molecule at an equilibrium bond distance of 1.4 Bohr, both using the 6-31G atomic basis set, initialized in an equal superposition of  $n = 2$  eigenstates (the ground and highest excited eigenstate). The chemical systems are described by the second-quantized electronic Hamiltonian

$\hat{H}_{\text{elec}}$  [199],

$$\hat{H}_{\text{elec}} = \sum_{p,q=1}^N h_q^p \hat{a}_p^\dagger \hat{a}_q + \frac{1}{2} \sum_{p,q,r,s=1}^N h_{rs}^{pq} \hat{a}_p^\dagger \hat{a}_q^\dagger \hat{a}_r \hat{a}_s, \quad (5.35)$$

where  $\hat{a}_p^\dagger$  and  $\hat{a}_p$  are fermionic creation and annihilation operators, respectively for the  $p^{\text{th}}$  atomic/molecular spin-orbital,  $h_q^p$  are one-electron core integrals, and  $h_{rs}^{pq}$  are two-electron repulsion integrals. The orbital population observable is the sum of spin-up and spin-down number operators  $\hat{a}^\dagger \hat{a} + \hat{a}^\dagger \hat{a}$  that act on the corresponding orbital.

A numerical statevector calculation is implemented using the Pauli Hamiltonian  $\hat{H}_P$ , which was mapped from the electronic Hamiltonian  $\hat{H}_{\text{elec}}$  using the Jordan-Wigner (JW) fermion-to-qubit mapping described in Section 2.5, that contains up to  $L = O(N^4)$  Pauli terms [14, 15]. For the He atom,  $\hat{H}_{\text{elec}}$  is mapped to a 4-qubit system with 27 terms in  $\hat{H}_P$ , and for the H<sub>2</sub> molecule, it is mapped to an 8-qubit system with 185 terms in  $\hat{H}_P$ . The time-evolved basis set consist of  $n = 2$  states: the initial state  $|0\rangle$  and  $|1\rangle = e^{-i\hat{H}/2} |0\rangle$ , where the parameter time is set to  $s_1 = \frac{1}{2}$ . Assuming an ideal, noiseless Hadamard Test with  $10^4$  simulated shots, 100 sets of the basis state overlaps  $\mathbf{F}$ , Hamiltonian matrices  $\mathbf{H}$  and the orbital population observable  $\mathbf{O}$  are randomly sampled. The ODE in Eq. (5.10) is then solved accordingly for every sample pair of  $\mathbf{F}$  and  $\mathbf{H}$  independently up to a simulation time  $t = 4 \text{ Hartree}^{-1}$  with a time step interval of  $\Delta t = 0.001 \text{ Hartree}^{-1}$ . The total number of time steps in this simulation is 4000, which far exceeds the threshold of  $100 \cdot 2^2 = 400$  time steps, placing this QAS demonstration well within the quantum resource-efficient regime. Finally, the orbital population is calculated at every time step for each sample run. Details on the sampling of  $\mathbf{F}$ ,  $\mathbf{H}$  and  $\mathbf{O}$  matrices can be found in Appendix B.3.

The orbital population dynamics of the He atom and H<sub>2</sub> molecule are plotted in Figs. 5.3

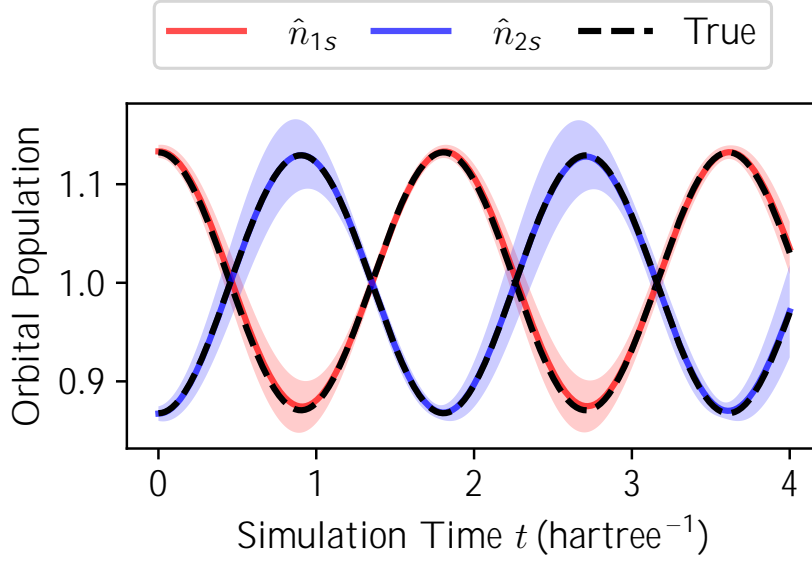


Figure 5.3: Atomic orbital population dynamics for the Helium atom using the 6-31G atomic orbital basis set, initialized in an equal superposition of the ground and highest excited state of eigenenergies  $-2.87$  and  $0.609$  Hartrees, respectively. The solid colored lines and shaded regions represents the mean and uncertainty of the 100 independent QAS simulation samples, each with  $10^4$  simulated shots, respectively. The true time-evolution is denoted by the black dashed line.

and 5.4, respectively. The colored solid lines and shaded regions represent the population mean and uncertainty of 100 independent QAS simulation samples, respectively. The true time-evolution is denoted by the black dashed line. Further plots of the total, Coulomb, kinetic, and potential energy dynamics, which demonstrate the total energy conservation feature of QAS, are provided in Appendix B.4.

For both systems, the orbital populations are observed to oscillate with a frequency of approximately  $0.5$  Hartree. These observations are in agreement with the true frequencies of  $-0.554$  and  $-0.490$  Hartrees respectively. For the helium atom, the maximum fractional population uncertainty is about  $4\%$  for the  $1s$  and  $5\%$  for the  $2s$  atomic orbitals. For the hydrogen molecule, the maximum fractional population uncertainty is about  $6\%$  for both the  $1$  and  $2$  molecular orbitals.

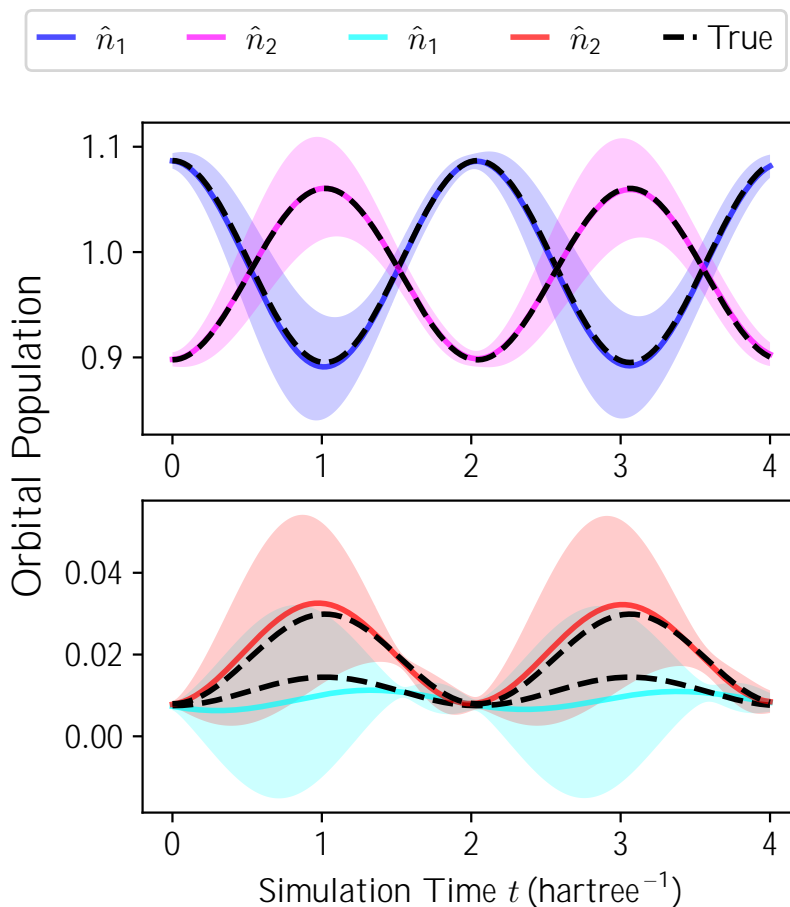


Figure 5.4: Molecular orbital population for Hydrogen molecule using the 6-31G atomic orbital basis set, at equilibrium distance of 1.4 Bohr, initialized in an equal superposition of the ground and highest excited state of eigenenergies -1.15 and 1.93 Hartrees, respectively. Solid colored line and shaded regions represent the mean and uncertainty of the 100 independent QAS simulation samples, each with  $10^4$  simulated shots, respectively. The true time-evolution is denoted by the black dashed line.

The population estimations of 1 and 2 molecular orbitals are observed to be extremely imprecise due to their low orbital population. This low precision can be improved by simply increasing number of shots, as shown by the linear relationship between the variance of the estimated quantities and number of shots in Appendix B.5. In principle, if the quantum subroutines are executed with minimal and unbiased quantum noise, indistinguishable to statistical shot noise, then the modified QAS can accurately simulate the quantum dynamics, though more shots would be needed to improve its precision.

## 5.4 Discussion and Outlook

By using a linear combination of time-evolved basis states as the evolution ansatz, the modified QAS can simulate the quantum dynamics of large systems more efficiently than the standard method. More precisely, if the system is initialized in an unknown superposition of  $n$  system eigenstates, then the QAS requires fewer quantum resources when the number of time steps exceeds  $100n^2$ . This efficiency is independent of the system size  $N$ , the number of terms in the electronic Hamiltonian or the mapped Pauli Hamiltonian, and the knowledge of the eigenstates and eigenvalues.

While the modified QAS has been demonstrated to simulate quantum dynamics using digital FTQC devices, analog quantum devices may be used as well due to its potential for practical quantum advantage in quantum simulation [28]. Several possible QAS approaches for analog quantum computation includes analog emulation of digital quantum simulation [287] or Hamiltonian learning techniques [288] to estimate elements of QAS dynamical equations in Eq. 5.10. However, these approaches must be further refined to mitigate any additional overheads that could negate the efficiency of QAS.

The results demonstrate that useful dynamical quantities of chemical systems can be estimated fairly accurately and precisely with modest amount of quantum-classical resources and minimal heuristics. However, the performance of QAS is highly dependent on the quality of the quantum time propagation algorithm employed. As an example, consider implementing the first-order Trotterization of time-evolved basis to prepare time-evolution basis for the helium atom case. A large number of Trotter steps would be required to achieve good simulation fidelity as shown in Appendix B.6. The trade-offs between the quality of the time-evolved basis state

and the overall quantum runtime complexity must be thoroughly analyzed. Thus, an important future direction would be to identify and refine time propagation techniques that minimize quantum resources while maximizing simulation accuracy for different system types.

Whilst QAS may seem very accurate when compared with other simulation algorithms, there is a major caveat that needs to be pointed out. The time-evolved basis is often linearly dependent, making the complex dynamical equation in Eq. (5.10) prone to ill-conditioning, thus resulting in numerical instabilities. As the number of eigenstates in the initial state  $n$  increases, there is an increasing likelihood of the time-evolved basis becoming too similar to each other as the corresponding eigenbasis amplitudes only differ in its phase angles but not in its magnitude, resulting in linear dependence of the basis. The parameter times must then be chosen carefully to avoid such an issue. In the  $n = 2$  base case, any parameter time  $s_1 = \frac{2-k}{e}$ , for any  $k \in \mathbb{Z}$  and eigenvalue difference  $\Delta e$ , is acceptable as it leads to a well-conditioned problem, as shown in Appendix B.7. For the  $n > 2$  case, however, solving for the complete set of conditions for the parameter times becomes an incredibly difficult problem and remains an open question on the best method to choose a optimal set of parameter times. In practice, for small  $n$ , a suitable set of parameter times is chosen heuristically via trial and error to avoid the complexity of solving the conditions so as to ensure an accurate and efficient simulation.

The resource analysis has suggested that if  $n \ll 2^N$  is kept significantly smaller than the size of the Hilbert space, then QAS becomes a practical hybrid quantum-classical algorithm as the classical runtime and memory scales polynomially in  $n$ . Quantum dynamical problems involving the dynamics of a few (unknown) eigenstates that may particularly benefit from QAS implementation. For example, in systems hosting quantum many-body scars, special simple initial states termed scar states can be expressed as a superposition of a few eigenstates with

dynamics restricted to a small subspace of the full Hilbert space [289, 290]. More generally, one may envisage quantum simulation applications involving systems whose ground state is resonantly excited by a fixed frequency drive term that is briefly applied, leading to dynamics involving eigenstates resonantly excited by the periodic drive term and its harmonics.

Besides applications to static systems, QAS can be extended to systems with a time-dependent Hamiltonian such as light-matter interaction, and atomic and molecular dynamics, though such tasks will likely involve a quantum-classical feedback loop which updates the Hamiltonian matrix  $H$  at every simulation time step, which will significantly increase the computation runtime and quantum resources. Nevertheless, to realize such applications, an important direction would be to develop efficient quantum state preparation algorithms which can reliably generate interesting superpositions of a few eigenstates.

It is expected that digital quantum computers with dozens of error-corrected qubits and gates will be available for use in the near future. If so, the aforementioned quantum time propagation algorithms may potentially be demonstrated beyond trivial toy systems to small, yet interesting systems. However, there is still a need for quantum resource-efficient simulation algorithms even when FTQC devices are available. Hence, QAS may thereby achieve a “quantum-assisted advantage” in the simulation of quantum dynamics, realizing a practical end-to-end quantum solution for quantum simulation as first envisioned by Feynman.

# Chapter 6

## Conclusion

This concluding chapter consists of two final sections. Section 6.1 briefly summarizes the ideas and results of the quantum algorithms proposed in this thesis: Variational Quantum Algorithm (VQA) for the estimation of correlation energies using perturbation theory using Noisy Intermediate-Scale Quantum (NISQ) devices in Chapter 3, shallow circuits for efficient correlated state preparation in Chapter 4 and Resource-Efficient Quantum-Assisted Simulator (QAS) in Chapter 5. Lastly, Section 6.2 discusses several emerging research directions and opportunities in quantum computational chemistry in the context of the rapid progress in quantum computing hardware.

### 6.1 Research Summary

First, Chapter 3 proposed a new VQA algorithm, the NISQ Orbital-Optimised Second-order Møller-Plesset Perturbation (NISQ-OMP2), that estimates the electronic ground correlation energy of chemical systems up the second order. The core idea is to treat electronic correlation as

a perturbation to the parameterized mean-field description of the chemical system. As a result, the correlation energy in NISQ-OMP2 can be expressed in terms of ordinary expectation values of the correlated operator with respect to the parameterized reference HF ground state, excited states and their equal superposition. These states are NISQ-friendly linear-depth Hartree-Fock (HF) ansatzes which differs in typical approaches that uses deep entangling circuits ansatz to estimate correlation energies. NISQ-OMP2 variationally optimizes these parameterized states using a hybrid quantum-classical optimization framework. Since the electronic correlation is a small correction to the initial HF energy, the ansatz optimization is made local by restricting the parameter landscape to a small region around the origin. This avoids the barren plateau problem that is prevalent in global ansatz optimization, which plagues many existing Variational Quantum Eigensolver (VQE) approaches such as Unitary Coupled Cluster (UCC). NISQ-OMP2 was demonstrated on two quantum computing platforms provided by IBM and AWS: FakeAuckland, numerically-simulated noisy model of a IBM NISQ device and cloud-accessed NISQ devices. The results successfully reproduce the equilibrium molecular energies and capturing perturbative electronic correlation effects at various molecular bond distances.

Second, Chapter 4 developed shallow circuits to efficiently prepare various types of fermionic states including Slater determinants and correlated states. The main idea is to apply linear combinations of anti-commuting fermionic operators, known as Clifford loaders, onto a vacuum state  $d$  times to prepare a  $d$ -fermion Slater determinant. These Clifford loaders can be decomposed using Givens rotation gates, that perform rotations within a two-dimensional fermionic subspace of a larger Hilbert space. This results in a quantum circuit with an overall  $O(\log_2 N)$  two-qubit gate depth under the Jordan-Wigner mapping. Thus, this method provides a subexponential reduction in two-qubit gate depth in preparing Slater determinants compared

to existing linear-depth approaches such as fermionic basis transformation. Additionally, this method was extended to imbue correlation between  $L$ -tuples of modes in the fermionic state. As a simple example, this method is used to prepare  $L = 2$ -wise correlated ansatz that captures a significant fraction of the correlation energy of hydrogen chains of sizes up to 20 qubits. The corresponding quantum circuits are ( $L = 2$ )-times shallower than that of the Slater determinant. This was a surprising result as generating correlated states in existing problem-inspired approaches such as UCC, typically requires deep entangling circuits than HF states which lacks electronic correlation. As a result, this method has the potential to enable high-accuracy quantum chemistry studies of sufficiently slow-growing  $d = O(N/\log_2^2 N)$  fermionic systems with larger basis sets on near-term quantum devices.

Third, Chapter 5 proposed the Resource-Efficient QAS algorithm to address the computational bottleneck of extracting desired quantum properties at intermediate time steps in quantum dynamics simulations. The central idea involves considering the time-evolution quantum ansatz as a complex linear combination of time-evolved basis states. This allows the quantum dynamics simulation to be split between a Fault-tolerant Quantum Computing (FTQC) device and a classical computer. If the system is initialized in an unknown superposition of  $n$  system eigenstates, then the FTQC device will only need to prepare  $n$  orthogonal time-evolved basis states at different fixed times and compute the corresponding basis overlaps, Hamiltonian and observable elements. These elements define the time evolution of the ansatz parameters and the observed quantities. The classical computer will only need to store  $n$  linear coefficients and evolve them according to the parameter evolution, without requiring any optimization or information on the eigenvalues and eigenstates. Once the entire ansatz parameter evolution is obtained, the quantum dynamics of the observable can be numerically

calculated without further quantum measurement on the system. If the number of superposing eigenstates in the initial system state  $n = 2^N$  is small, then QAS can efficiently simulate large  $N$  system sizes for a large number of time steps above  $100n^2$ , outperforming most existing quantum simulators. This was demonstrated in the orbital population simulation of a Helium atom and a Hydrogen molecule initialized in a superposition of  $n = 2$  eigenstates with 4000 time steps that far exceeds the threshold of  $100 \cdot 2^2 = 400$  time steps. As a result, it shows that the QAS consumes fewer quantum resources than the standard approach of preparing multiple copies of time-evolved states for quantum measurement of the dynamical quantities.

## 6.2 Emerging Directions and Future Research

With the recent success in demonstrating intermediate-scale Quantum Error Correction (QEC), it is reasonable to expect that early-forms of digital FTQC devices with a few logical qubits and gates will become available in the next decade. Should these FTQC devices become available, deeper entangling ansatz and FTQC algorithms such as Hamiltonian simulation and QPE may become feasible. However, current quantum resources estimates of FTQC applications in quantum chemistry remain prohibitively expensive due to the large overhead required for QEC [34]. For example, performing a two-qubit iterative QPE for a one-qubit hydrogen molecule in a minimal basis set using a 2D surface code requires thousands of physical qubits and QEC rounds, assuming physical error rate of  $10^{-3}$  [291]. As a result, large chemically-relevant problems requiring hundreds of logical qubits – and potentially millions of physical qubits and QEC rounds – are likely to remain beyond reach in the foreseeable future.

Given this challenge, there is a pressing need to minimize the number of logical or physics qubits required to represent the chemical system accurately. Potential solutions include

the development of efficient sets of atomic or molecular basis sets using existing quantum techniques such as tensor network techniques [292] or density functional theory [293]. Another promising direction is to develop resource-efficient error correction procedures tailored for large-scale chemistry problems [294], efficiently distributing limited QEC resources over different computational parts to minimize overheads.

While FTQC algorithms offer exponential speedups in quantum time-evolution and eigenvalue estimation tasks, no known quantum advantage exists for eigen-structure problems in quantum chemistry [142]. The reason is that achieving exponential quantum advantage in quantum eigenstate preparation is conjectured to be highly unlikely [295]. As quantum computational chemistry advances toward realizing quantum advantage, it is therefore increasingly important to focus other, less explored, yet significant computational tasks that do not explicitly involve solving quantum eigenstructures. These tasks include classical Molecular Dynamics (MD) simulations [296], chemical reactions [297] and Quantum Monte-Carlo (QMC) [298], where quantum computers may provide tangible speedups.

Moreover, developing efficient quantum subroutines that complement promising FTQC algorithms is crucial to ensure optimal use of quantum resources. For instance, future FTQC applications in quantum chemistry could draw inspirations from decomposition approaches. In these, key chemical subsystems are accurately simulated, while less critical subsystems are treated with lower accuracy, thus optimizing quantum resources utilization for simulating large quantum systems [299–302].

Quantum computational chemistry is a rapidly evolving field that aims to leverage quantum computing for efficiently simulation of complex chemical systems. Although efficient

quantum algorithms exist, quantum chemistry problems are inherently difficult and are expected to remain so. Even with the advent of FTQC devices, the large resource requirements pose significant computational challenges that could impede practical demonstration of chemically-relevant quantum simulation. Therefore, NISQy-type algorithms developed in this thesis may play an important role as efficient subroutines when running algorithms in the FTQC or early-FTQC [303] era. These developments deepen our understanding of quantum computing capabilities in quantum chemistry and motivate future research prospects. Given the significant strides in computation chemistry enabled by the invention of the modern computer, there is reasonable hope for further exciting innovations in quantum computation chemistry hereafter as quantum hardware continues progresses toward Fault-Tolerance.

# References

- [1] P. A. M. Dirac, “Quantum mechanics of many-electron systems”, *Proc. R. Soc. A* **123**, 714–733 (1929).
- [2] T. Helgaker, S. Coriani, P. Jørgensen, K. Kristensen, J. Olsen, and K. Ruud, “Recent Advances in Wave Function-Based Methods of Molecular-Property Calculations”, *Chem. Rev.* **112**, 543–631 (2012).
- [3] V. A. Rassolov and S. Garashchuk, “Computational complexity in quantum chemistry”, *Chem. Phys. Lett.* **464**, 262–264 (2008).
- [4] J. D. Whitfield, P. J. Love, and A. Aspuru-Guzik, “Computational complexity in electronic structure”, *Phys. Chem. Chem. Phys.* **15**, 397–411 (2013).
- [5] P. Jordan and E. Wigner, “Über das Paulische Äquivalenzverbot”, *Z. Physik.* **47**, 631–651 (1928).
- [6] S. B. Bravyi and A. Y. Kitaev, “Fermionic Quantum Computation”, *Ann. Phys. (N. Y.)* **298**, 210–226 (2002).
- [7] D. Deutsch, “Quantum theory, the Church–Turing principle and the universal quantum computer”, *Proc. R. Soc. A* **400**, 97–117 (1985).
- [8] S. Lloyd, “Universal Quantum Simulators”, *Science* **273**, 1073–1078 (1996).

- [9] D. W. Berry, G. Ahokas, R. Cleve, and B. C. Sanders, “Efficient Quantum Algorithms for Simulating Sparse Hamiltonians”, *Commun. Math. Phys.* **270**, 359–371 (2007).
- [10] I. M. Georgescu, S. Ashhab, and F. Nori, “Quantum simulation”, *Rev. Mod. Phys.* **86**, 153–185 (2014).
- [11] R. P. Muller and R. Blume-Kohout, “The Promise of Quantum Simulation”, *ACS Nano* **9**, 7738–7741 (2015).
- [12] A. M. Childs, D. Maslov, Y. Nam, N. J. Ross, and Y. Su, “Toward the first quantum simulation with quantum speedup”, *Proc. Natl. Acad. Sci. U.S.A.* **115**, 9456–9461 (2018).
- [13] Y. Cao, J. Romero, J. P. Olson, M. Degroote, P. D. Johnson, M. Kieferová, I. D. Kivlichan, T. Menke, B. Peropadre, N. P. D. Sawaya, S. Sim, L. Veis, and A. Aspuru-Guzik, “Quantum Chemistry in the Age of Quantum Computing”, *Chem. Rev.* **119**, 10856–10915 (2019).
- [14] S. McArdle, S. Endo, A. Aspuru-Guzik, S. C. Benjamin, and X. Yuan, “Quantum computational chemistry”, *Rev. Mod. Phys.* **92**, 015003 (2020).
- [15] B. Bauer, S. Bravyi, M. Motta, and G. K.-L. Chan, “Quantum Algorithms for Quantum Chemistry and Quantum Materials Science”, *Chem. Rev.* **120**, 12685–12717 (2020).
- [16] M. Motta and J. E. Rice, “Emerging quantum computing algorithms for quantum chemistry”, *WIREs Comput. Mol. Sci.* **12**, e1580 (2022).
- [17] P. Benioff, “The computer as a physical system: A microscopic quantum mechanical Hamiltonian model of computers as represented by Turing machines”, *J. Stat. Phys.* **22**, 563–591 (1980).
- [18] R. P. Feynman, “Simulating physics with computers”, *Int. J. Theor. Phys.* **21**, 467–488 (1982).
- [19] R. P. Feynman, “Quantum mechanical computers”, *Found. Phys.* **16**, 507–531 (1986).

- [20] P. Shor, “Algorithms for quantum computation: discrete logarithms and factoring”, in *Proceedings 35th Annual Symposium on Foundations of Computer Science* (1994), pp. 124–134.
- [21] L. K. Grover, “A fast quantum mechanical algorithm for database search”, in *Proceedings of the twenty-eighth annual ACM symposium on Theory of Computing, STOC '96* (1996), pp. 212–219.
- [22] A. W. Harrow, A. Hassidim, and S. Lloyd, “Quantum Algorithm for Linear Systems of Equations”, *Phys. Rev. Lett.* **103**, 150502 (2009).
- [23] S. L. Braunstein, H.-K. Lo, and P. Kok, eds., *Scalable quantum computers: paving the way to realization* (Wiley-VCH, Berlin, 2001).
- [24] T. D. Ladd, F. Jelezko, R. Laflamme, Y. Nakamura, C. Monroe, and J. L. O’Brien, “Quantum computers”, *Nature* **464**, 45–53 (2010).
- [25] G. Falci and E. Paladino, “The physics of quantum computation”, *Int. J. Quantum Inf.* **12**, 1430003 (2014).
- [26] L. Gyongyosi and S. Imre, “A Survey on quantum computing technology”, *Comput. Sci. Rev.* **31**, 51–71 (2019).
- [27] J. I. Cirac and P. Zoller, “Goals and opportunities in quantum simulation”, *Nat. Phys.* **8**, 264–266 (2012).
- [28] A. J. Daley, I. Bloch, C. Kokail, S. Flannigan, N. Pearson, M. Troyer, and P. Zoller, “Practical quantum advantage in quantum simulation”, *Nature* **607**, 667–676 (2022).
- [29] M. A. Nielsen and I. L. Chuang, *Quantum Computation and Quantum Information: 10th Anniversary Edition* (Cambridge University Press, 2010).
- [30] J. Argüello-Luengo, A. González-Tudela, T. Shi, P. Zoller, and J. I. Cirac, “Analogue quantum chemistry simulation”, *Nature* **574**, 215–218 (2019).

- [31] A. Y. Smirnov, S. Savel'ev, L. G. Mouroukh, and F. Nori, "Modelling chemical reactions using semiconductor quantum dots", *EPL* **80**, 67008 (2007).
- [32] M. Kang, H. Nuomin, S. N. Chowdhury, J. L. Yuly, K. Sun, J. Whitlow, J. Valdiviezo, Z. Zhang, P. Zhang, D. N. Beratan, and K. R. Brown, "Seeking a quantum advantage with trapped-ion quantum simulations of condensed-phase chemical dynamics", *Nat. Rev. Chem.* **8**, 340–358 (2024).
- [33] I. Kassal, J. D. Whitfield, A. Perdomo-Ortiz, M.-H. Yung, and A. Aspuru-Guzik, "Simulating Chemistry Using Quantum Computers", *Annu. Rev. Phys. Chem.* **62**, 185–207 (2011).
- [34] M. Reiher, N. Wiebe, K. M. Svore, D. Wecker, and M. Troyer, "Elucidating reaction mechanisms on quantum computers", *Proc. Natl. Acad. Sci. U.S.A.* **114**, 7555–7560 (2017).
- [35] P. Krantz, M. Kjaergaard, F. Yan, T. P. Orlando, S. Gustavsson, and W. D. Oliver, "A quantum engineer's guide to superconducting qubits", *Appl. Phys. Rev.* **6**, 021318 (2019).
- [36] H.-L. Huang, D. Wu, D. Fan, and X. Zhu, "Superconducting quantum computing: a review", *Sci. China Inf. Sci.* **63**, 180501 (2020).
- [37] C. D. Bruzewicz, J. Chiaverini, R. McConnell, and J. M. Sage, "Trapped-ion quantum computing: Progress and challenges", *Appl. Phys. Rev.* **6**, 021314 (2019).
- [38] C. Monroe, W. C. Campbell, L.-M. Duan, Z.-X. Gong, A. V. Gorshkov, P. W. Hess, R. Islam, K. Kim, N. M. Linke, G. Pagano, P. Richerme, C. Senko, and N. Y. Yao, "Programmable quantum simulations of spin systems with trapped ions", *Rev. Mod. Phys.* **93**, 025001 (2021).

- [39] M. Saffman, T. G. Walker, and K. Mølmer, “Quantum information with Rydberg atoms”, *Rev. Mod. Phys.* **82**, 2313–2363 (2010).
- [40] M. Saffman, “Quantum computing with atomic qubits and Rydberg interactions: progress and challenges”, *J. Phys. B* **49**, 202001 (2016).
- [41] M. Morgado and S. Whitlock, “Quantum simulation and computing with Rydberg-interacting qubits”, *AVS Quantum Sci.* **3**, 023501 (2021).
- [42] A. Chatterjee, P. Stevenson, S. De Franceschi, A. Morello, N. P. de Leon, and F. Kuemmeth, “Semiconductor qubits in practice”, *Nat. Rev. Phys.* **3**, 157–177 (2021).
- [43] G. Burkard, T. D. Ladd, A. Pan, J. M. Nichol, and J. R. Petta, “Semiconductor spin qubits”, *Rev. Mod. Phys.* **95**, 025003 (2023).
- [44] F. Flamini, N. Spagnolo, and F. Sciarrino, “Photonic quantum information processing: a review”, *Rep. Prog. Phys.* **82**, 016001 (2018).
- [45] S. Slussarenko and G. J. Pryde, “Photonic quantum information processing: A concise review”, *Appl. Phys. Rev.* **6**, 041303 (2019).
- [46] W. Bogaerts, D. Pérez, J. Capmany, D. A. B. Miller, J. Poon, D. Englund, F. Morichetti, and A. Melloni, “Programmable photonic circuits”, *Nature* **586**, 207–216 (2020).
- [47] J. E. Bourassa, R. N. Alexander, M. Vasmer, A. Patil, I. Tzitrin, T. Matsuura, D. Su, B. Q. Baragiola, S. Guha, G. Dauphinais, K. K. Sabapathy, N. C. Menicucci, and I. Dhand, “Blueprint for a Scalable Photonic Fault-Tolerant Quantum Computer”, *Quantum* **5**, 392 (2021).
- [48] J. M. Arrazola et al., “Quantum circuits with many photons on a programmable nanophotonic chip”, *Nature* **591**, 54–60 (2021).
- [49] P. W. Shor, “Scheme for reducing decoherence in quantum computer memory”, *Phys. Rev. A* **52**, R2493–R2496 (1995).

- [50] D. E. Gottesman, “Stabilizer Codes and Quantum Error Correction”, PhD thesis (California Institute of Technology, 1997).
- [51] D. A. Lidar and T. A. Brun, eds., *Quantum Error Correction*, Illustrated edition (Cambridge University Press, Cambridge, United Kingdom ; New York, Oct. 2013).
- [52] B. M. Terhal, “Quantum error correction for quantum memories”, *Rev. Mod. Phys.* **87**, 307–346 (2015).
- [53] G. G. L. Guardia, *Quantum Error Correction: Symmetric, Asymmetric, Synchronizable, and Convolutional Codes*, 1st ed. 2020 edition (Springer, Cham, Switzerland, June 2020).
- [54] P. Shor, “Fault-tolerant quantum computation”, in *Proceedings of 37th Conference on Foundations of Computer Science* (1996), pp. 56–65.
- [55] E. Knill, R. Laflamme, and W. H. Zurek, “Resilient Quantum Computation”, *Science* **279**, 342–345 (1998).
- [56] A. Y. Kitaev, “Fault-tolerant quantum computation by anyons”, *Ann. Phys. (N. Y.)* **303**, 2–30 (2003).
- [57] D. Aharonov and M. Ben-Or, “Fault-Tolerant Quantum Computation with Constant Error Rate”, *SIAM J. Comput.* **38**, 1207–1282 (2008).
- [58] Google Quantum AI, “Suppressing quantum errors by scaling a surface code logical qubit”, *Nature* **614**, 676–681 (2023).
- [59] Google Quantum AI, *Quantum error correction below the surface code threshold*, Aug. 2024, [arXiv:2408.13687](https://arxiv.org/abs/2408.13687).
- [60] D. Bluvstein et al., “Logical quantum processor based on reconfigurable atom arrays”, *Nature* **626**, 58–65 (2024).
- [61] M. P. da Silva et al., *Demonstration of logical qubits and repeated error correction with better-than-physical error rates*, Apr. 2024, [arXiv:2404.02280](https://arxiv.org/abs/2404.02280).

- [62] I. Thorvaldson et al., *Grover’s algorithm in a four-qubit silicon processor above the fault-tolerant threshold*, Apr. 2024, [arXiv:2404.08741](#).
- [63] E. Campbell, “A series of fast-paced advances in Quantum Error Correction”, *Nat. Rev. Phys.* **6**, 160–161 (2024).
- [64] J. Preskill, “Quantum Computing in the NISQ era and beyond”, *Quantum* **2**, 79 (2018).
- [65] S. Endo, Z. Cai, S. C. Benjamin, and X. Yuan, “Hybrid Quantum-Classical Algorithms and Quantum Error Mitigation”, *J. Phys. Soc. Jpn.* **90**, 032001 (2021).
- [66] K. Bharti, A. Cervera-Lierta, T. H. Kyaw, T. Haug, S. Alperin-Lea, A. Anand, M. Degroote, H. Heimonen, J. S. Kottmann, T. Menke, W.-K. Mok, S. Sim, L.-C. Kwek, and A. Aspuru-Guzik, “Noisy intermediate-scale quantum algorithms”, *Rev. Mod. Phys.* **94**, 015004 (2022).
- [67] H.-L. Huang, X.-Y. Xu, C. Guo, G. Tian, S.-J. Wei, X. Sun, W.-S. Bao, and G.-L. Long, “Near-term quantum computing techniques: Variational quantum algorithms, error mitigation, circuit compilation, benchmarking and classical simulation”, *Sci. China Phys. Mech. Astron.* **66**, 250302 (2023).
- [68] S. Bravyi, J. M. Gambetta, A. Mezzacapo, and K. Temme, *Tapering off qubits to simulate fermionic Hamiltonians*, Jan. 2017, [arXiv:1701.08213](#).
- [69] K. Setia, R. Chen, J. E. Rice, A. Mezzacapo, M. Pistoia, and J. D. Whitfield, “Reducing Qubit Requirements for Quantum Simulations Using Molecular Point Group Symmetries”, *J. Chem. Theory Comput.* **16**, 6091–6097 (2020).
- [70] D. Picozzi and J. Tennyson, “Symmetry-adapted encodings for qubit number reduction by point-group and other Boolean symmetries”, *Quantum Sci. Technol.* **8**, 035026 (2023).

- [71] V. Verteletskyi, T.-C. Yen, and A. F. Izmaylov, “Measurement optimization in the variational quantum eigensolver using a minimum clique cover”, *J. Chem. Phys.* **152**, 124114 (2020).
- [72] A. F. Izmaylov, T.-C. Yen, R. A. Lang, and V. Verteletskyi, “Unitary Partitioning Approach to the Measurement Problem in the Variational Quantum Eigensolver Method”, *J. Chem. Theory Comput.* **16**, 190–195 (2020).
- [73] A. Zhao, A. Tranter, W. M. Kirby, S. F. Ung, A. Miyake, and P. J. Love, “Measurement reduction in variational quantum algorithms”, *Phys. Rev. A* **101**, 062322 (2020).
- [74] O. Crawford, B. van Straaten, D. Wang, T. Parks, E. Campbell, and S. Brierley, “Efficient quantum measurement of Pauli operators in the presence of finite sampling error”, *Quantum* **5**, 385 (2021).
- [75] S. E. Smart and D. A. Mazziotti, “Lowering tomography costs in quantum simulation with a symmetry projected operator basis”, *Phys. Rev. A* **103**, 012420 (2021).
- [76] R. Kondo, Y. Sato, S. Koide, S. Kajita, and H. Takamatsu, “Computationally Efficient Quantum Expectation with Extended Bell Measurements”, *Quantum* **6**, 688 (2022).
- [77] B. Wu, J. Sun, Q. Huang, and X. Yuan, “Overlapped grouping measurement: A unified framework for measuring quantum states”, *Quantum* **7**, 896 (2023), [arXiv:2105.13091](https://arxiv.org/abs/2105.13091).
- [78] T.-C. Yen, A. Ganeshram, and A. F. Izmaylov, “Deterministic improvements of quantum measurements with grouping of compatible operators, non-local transformations, and covariance estimates”, *npj Quantum Inf.* **9**, 1–7 (2023).
- [79] H.-Y. Huang, R. Kueng, and J. Preskill, “Predicting many properties of a quantum system from very few measurements”, *Nat. Phys.* **16**, 1050–1057 (2020).
- [80] A. Zhao, N. C. Rubin, and A. Miyake, “Fermionic Partial Tomography via Classical Shadows”, *Phys. Rev. Lett.* **127**, 110504 (2021).

- [81] R. Levy, D. Luo, and B. K. Clark, “Classical shadows for quantum process tomography on near-term quantum computers”, *Phys. Rev. Res.* **6**, 013029 (2024).
- [82] Y. Hirata, M. Nakanishi, S. Yamashita, and Y. Nakashima, “An efficient conversion of quantum circuits to a linear nearest neighbor architecture”, *Quantum Info. Comput.* **11**, 142–166 (2011).
- [83] D. Maslov, “Basic circuit compilation techniques for an ion-trap quantum machine”, *New J. Phys.* **19**, 023035 (2017).
- [84] A. Paler, I. Polian, K. Nemoto, and S. J. Devitt, “Fault-tolerant, high-level quantum circuits: form, compilation and description”, *Quantum Sci. Technol.* **2**, 025003 (2017).
- [85] S. Khatri, R. LaRose, A. Poremba, L. Cincio, A. T. Sornborger, and P. J. Coles, “Quantum-assisted quantum compiling”, *Quantum* **3**, 140 (2019), [arXiv:1807.00800](https://arxiv.org/abs/1807.00800).
- [86] P. Jurcevic et al., “Demonstration of quantum volume 64 on a superconducting quantum computing system”, *Quantum Sci. Technol.* **6**, 025020 (2021).
- [87] K. Temme, S. Bravyi, and J. M. Gambetta, “Error Mitigation for Short-Depth Quantum Circuits”, *Phys. Rev. Lett.* **119**, 180509 (2017).
- [88] A. Kandala, K. Temme, A. D. Córcoles, A. Mezzacapo, J. M. Chow, and J. M. Gambetta, “Error mitigation extends the computational reach of a noisy quantum processor”, *Nature* **567**, 491–495 (2019).
- [89] Z. Cai, R. Babbush, S. C. Benjamin, S. Endo, W. J. Huggins, Y. Li, J. R. McClean, and T. E. O’Brien, “Quantum error mitigation”, *Rev. Mod. Phys.* **95**, 045005 (2023).
- [90] J. Izaac and J. Wang, *Computational Quantum Mechanics*, Undergraduate Lecture Notes in Physics (Springer, Cham, 2018).

- [91] G. D. Smith, *Numerical Solution of Partial Differential Equations: Finite Difference Methods*, 3rd ed., Oxford Applied Mathematics and Computing Science Series (Clarendon Press, Oxford, Dec. 1985).
- [92] J. W. Thomas, *Numerical Partial Differential Equations: Finite Difference Methods*, edited by J. E. Marsden, L. Sirovich, M. Golubitsky, and W. Jäger, Vol. 22, Texts in Applied Mathematics (Springer, New York, NY, 1995).
- [93] H. P. Langtangen and S. Linge, *Finite Difference Computing with PDEs: A Modern Software Approach*, Vol. 16, Texts in Computational Science and Engineering (Springer, Cham, 2017).
- [94] W. H. Press, S. A. Teukolsky, W. T. Vetterling, and B. P. Flannery, *Numerical Recipes 3rd Edition: The Art of Scientific Computing*, 3rd ed. (Cambridge University Press, USA, 2007).
- [95] R. Dick, “Time-Dependent Perturbations in Quantum Mechanics”, in *Advanced Quantum Mechanics*, Graduate Texts in Physics (Springer, Cham, 2020), pp. 265–310.
- [96] A. McLachlan, “A variational solution of the time-dependent Schrodinger equation”, *Mol. Phys.* **8**, 39–44 (1964).
- [97] “The time-dependent variational principle (TDVP)”, in *Geometry of the Time-Dependent Variational Principle in Quantum Mechanics*, edited by P. Kramer and M. Saraceno, Lecture Notes in Physics (Springer, Berlin, Heidelberg, 1981), pp. 3–14.
- [98] J. Broeckhove, L. Lathouwers, E. Kesteloot, and P. Van Leuven, “On the equivalence of time-dependent variational principles”, *Chem. Phys. Lett.* **149**, 547–550 (1988).
- [99] P. Kramer, “A review of the time-dependent variational principle”, *J. Phys. Conf. Ser.* **99**, 012009 (2008).

- [100] G. Carleo, F. Becca, M. Schiró, and M. Fabrizio, “Localization and Glassy Dynamics Of Many-Body Quantum Systems”, *Sci. Rep.* **2**, 243 (2012).
- [101] G. Carleo, L. Cevolani, L. Sanchez-Palencia, and M. Holzmann, “Unitary Dynamics of Strongly Interacting Bose Gases with the Time-Dependent Variational Monte Carlo Method in Continuous Space”, *Phys. Rev. X* **7**, 031026 (2017).
- [102] M. Born and R. Oppenheimer, “Zur Quantentheorie der Molekeln”, *Ann. Phys. (Berl.)* **389**, 457–484 (1927).
- [103] R. S. Mulliken, “Spectroscopy, Molecular Orbitals, and Chemical Bonding”, *Science* **157**, 13–24 (1967).
- [104] P.-O. Löwdin, “Correlation Problem in Many-Electron Quantum Mechanics I. Review of Different Approaches and Discussion of Some Current Ideas”, in *Advances in Chemical Physics*, edited by I. Prigogine (John Wiley & Sons, Ltd, 1958), pp. 207–322.
- [105] J. M. L. Martin, “Electron Correlation: Nature’s Weird and Wonderful Chemical Glue”, *Isr. J. Chem.* **62**, e202100111 (2022).
- [106] J. C. Slater, “A Simplification of the Hartree-Fock Method”, *Phys. Rev.* **81**, 385–390 (1951).
- [107] R. J. Bartlett and M. Musiał, “Coupled-cluster theory in quantum chemistry”, *Rev. Mod. Phys.* **79**, 291–352 (2007).
- [108] I. Shavitt, “The Method of Configuration Interaction”, in *Methods of Electronic Structure Theory*, Vol. 3, edited by H. F. Schaefer, Modern Theoretical Chemistry (Springer, Boston, MA, 1977), pp. 189–275.
- [109] C. David Sherrill and H. F. Schaefer, “The Configuration Interaction Method: Advances in Highly Correlated Approaches”, in *Advances in Quantum Chemistry*, Vol. 34, edited

- by P.-O. Löwdin, J. R. Sabin, M. C. Zerner, and E. Brändas (Academic Press, 1999), pp. 143–269.
- [110] P.-O. Löwdin, “Quantum Theory of Many-Particle Systems. III. Extension of the Hartree-Fock Scheme to Include Degenerate Systems and Correlation Effects”, *Phys. Rev.* **97**, 1509–1520 (1955).
- [111] J. P. Perdew, “Jacob’s ladder of density functional approximations for the exchange-correlation energy”, in *AIP Conference Proceedings*, Vol. 577 (2001), pp. 1–20.
- [112] M. P. Housden and N. C. Pyper, “The noble gas dimers as a probe of the energetic contributions of dispersion and short-range electron correlation in weakly bound systems”, *Mol. Phys.* **105**, 2353–2361 (2007).
- [113] V. Magnasco, “Post-Hartree–Fock Methods”, in *Methods of Molecular Quantum Mechanics* (John Wiley & Sons, Ltd, 2009) Chap. 8, pp. 133–139.
- [114] H. Gao, S. Imamura, A. Kasagi, and E. Yoshida, “Distributed Implementation of Full Configuration Interaction for One Trillion Determinants”, *J. Chem. Theory Comput.* **20**, 1185–1192 (2024).
- [115] Editorial, “Green ammonia synthesis”, *Nat. Synth.* **2**, 581–582 (2023).
- [116] V. Kyriakou, I. Garagounis, A. Vourros, E. Vasileiou, and M. Stoukides, “An Electrochemical Haber-Bosch Process”, *Joule* **4**, 142–158 (2020).
- [117] B. M. Boghosian and W. Taylor, “Simulating quantum mechanics on a quantum computer”, *Physica D* **120**, 30–42 (1998).
- [118] A. Miessen, P. J. Ollitrault, F. Tacchino, and I. Tavernelli, “Quantum algorithms for quantum dynamics”, *Nat Comput Sci* **3**, 25–37 (2023).
- [119] B. Fauseweh, “Quantum many-body simulations on digital quantum computers: State-of-the-art and future challenges”, *Nat. Commun.* **15**, 2123 (2024).

- [120] M. Suzuki, “Fractal decomposition of exponential operators with applications to many-body theories and Monte Carlo simulations”, *Phys. Lett. A* **146**, 319–323 (1990).
- [121] M. Suzuki, “General theory of fractal path integrals with applications to many-body theories and statistical physics”, *J. Math. Phys.* **32**, 400–407 (1991).
- [122] A. M. Childs and Y. Su, “Nearly Optimal Lattice Simulation by Product Formulas”, *Phys. Rev. Lett.* **123**, 050503 (2019).
- [123] A. M. Childs, Y. Su, M. C. Tran, N. Wiebe, and S. Zhu, “Theory of Trotter Error with Commutator Scaling”, *Phys. Rev. X* **11**, 011020 (2021).
- [124] J. Haah, M. B. Hastings, R. Kothari, and G. H. Low, “Quantum Algorithm for Simulating Real Time Evolution of Lattice Hamiltonians”, *SIAM J. Comput.* **52**, FOCS18–250 (2023).
- [125] S. Wiesner, *Simulations of Many-Body Quantum Systems by a Quantum Computer*, Mar. 1996, [arXiv:quant-ph/9603028](https://arxiv.org/abs/quant-ph/9603028).
- [126] C. Zalka, “Simulating quantum systems on a quantum computer”, *Proc. R. Soc. A.* **454**, 313–322 (1998).
- [127] I. Kassal, S. P. Jordan, P. J. Love, M. Mohseni, and A. Aspuru-Guzik, “Polynomial-time quantum algorithm for the simulation of chemical dynamics”, *Proc. Natl. Acad. Sci. U.S.A.* **105**, 18681–18686 (2008).
- [128] A. M. Childs and N. Wiebe, “Hamiltonian simulation using linear combinations of unitary operations”, *Quantum Info. Comput.* **12**, 901–924 (2012).
- [129] D. W. Berry, A. M. Childs, R. Cleve, R. Kothari, and R. D. Somma, “Simulating Hamiltonian Dynamics with a Truncated Taylor Series”, *Phys. Rev. Lett.* **114**, 090502 (2015).

- [130] A. M. Childs and D. W. Berry, “Black-box Hamiltonian simulation and unitary implementation”, *Quantum Inf. Comput.* **12**, 29–62 (2012).
- [131] D. W. Berry, A. M. Childs, and R. Kothari, “Hamiltonian Simulation with Nearly Optimal Dependence on all Parameters”, in *2015 IEEE 56th Annual Symposium on Foundations of Computer Science* (2015), pp. 792–809.
- [132] G. H. Low and I. L. Chuang, “Optimal Hamiltonian Simulation by Quantum Signal Processing”, *Phys. Rev. Lett.* **118**, 010501 (2017).
- [133] G. H. Low and I. L. Chuang, “Hamiltonian Simulation by Qubitization”, *Quantum* **3**, 163 (2019).
- [134] D. S. Abrams and S. Lloyd, “Simulation of Many-Body Fermi Systems on a Universal Quantum Computer”, *Phys. Rev. Lett.* **79**, 2586–2589 (1997).
- [135] R. Babbush, W. J. Huggins, D. W. Berry, S. F. Ung, A. Zhao, D. R. Reichman, H. Neven, A. D. Baczewski, and J. Lee, “Quantum simulation of exact electron dynamics can be more efficient than classical mean-field methods”, *Nat. Commun.* **14**, 4058 (2023).
- [136] D. A. Lidar and H. Wang, “Calculating the thermal rate constant with exponential speedup on a quantum computer”, *Phys. Rev. E* **59**, 2429–2438 (1999).
- [137] D. S. Abrams and S. Lloyd, “Quantum Algorithm Providing Exponential Speed Increase for Finding Eigenvalues and Eigenvectors”, *Phys. Rev. Lett.* **83**, 5162–5165 (1999).
- [138] A. Aspuru-Guzik, A. D. Dutoi, P. J. Love, and M. Head-Gordon, “Simulated Quantum Computation of Molecular Energies”, *Science* **309**, 1704–1707 (2005).
- [139] L. Veis and J. Pittner, “Adiabatic state preparation study of methylene”, *J. Chem. Phys.* **140**, 214111 (2014).
- [140] T. Albash and D. A. Lidar, “Adiabatic quantum computation”, *Rev. Mod. Phys.* **90**, 015002 (2018).

- [141] M. Motta, C. Sun, A. T. K. Tan, M. J. O'Rourke, E. Ye, A. J. Minnich, F. G. S. L. Brandão, and G. K.-L. Chan, "Determining eigenstates and thermal states on a quantum computer using quantum imaginary time evolution", *Nat. Phys.* **16**, 205–210 (2020).
- [142] S. Lee, J. Lee, H. Zhai, Y. Tong, A. M. Dalzell, A. Kumar, P. Helms, J. Gray, Z.-H. Cui, W. Liu, M. Kastoryano, R. Babbush, J. Preskill, D. R. Reichman, E. T. Campbell, E. F. Valeev, L. Lin, and G. K.-L. Chan, "Evaluating the evidence for exponential quantum advantage in ground-state quantum chemistry", *Nat. Commun.* **14**, 1952 (2023).
- [143] V. E. Elfving, B. W. Broer, M. Webber, J. Gavartin, M. D. Halls, K. P. Lorton, and A. Bochevarov, *How will quantum computers provide an industrially relevant computational advantage in quantum chemistry?*, 2020, [arXiv:2009.12472](https://arxiv.org/abs/2009.12472).
- [144] J. R. McClean, J. Romero, R. Babbush, and A. Aspuru-Guzik, "The theory of variational hybrid quantum-classical algorithms", *New J. Phys.* **18**, 023023 (2016).
- [145] A. Peruzzo, J. McClean, P. Shadbolt, M.-H. Yung, X.-Q. Zhou, P. J. Love, A. Aspuru-Guzik, and J. L. O'Brien, "A variational eigenvalue solver on a photonic quantum processor", *Nat. Commun.* **5**, 4213 (2014).
- [146] C. Hempel, C. Maier, J. Romero, J. McClean, T. Monz, H. Shen, P. Jurcevic, B. P. Lanyon, P. Love, R. Babbush, A. Aspuru-Guzik, R. Blatt, and C. F. Roos, "Quantum Chemistry Calculations on a Trapped-Ion Quantum Simulator", *Phys. Rev. X* **8**, 031022 (2018).
- [147] P. J. J. O'Malley et al., "Scalable Quantum Simulation of Molecular Energies", *Phys. Rev. X* **6**, 031007 (2016).
- [148] Y. Shen, X. Zhang, S. Zhang, J.-N. Zhang, M.-H. Yung, and K. Kim, "Quantum implementation of the unitary coupled cluster for simulating molecular electronic structure", *Phys. Rev. A* **95**, 020501 (2017).

- [149] A. Kandala, A. Mezzacapo, K. Temme, M. Takita, M. Brink, J. M. Chow, and J. M. Gambetta, “Hardware-efficient variational quantum eigensolver for small molecules and quantum magnets”, *Nature* **549**, 242–246 (2017).
- [150] R. Santagati, J. Wang, A. A. Gentile, S. Paesani, N. Wiebe, J. R. McClean, S. Morley-Short, P. J. Shadbolt, D. Bonneau, J. W. Silverstone, D. P. Tew, X. Zhou, J. L. O’Brien, and M. G. Thompson, “Witnessing eigenstates for quantum simulation of Hamiltonian spectra”, *Sci. Adv.* **4**, eaap9646 (2018).
- [151] J. I. Colless, V. V. Ramasesh, D. Dahlen, M. S. Blok, M. E. Kimchi-Schwartz, J. R. McClean, J. Carter, W. A. de Jong, and I. Siddiqi, “Computation of Molecular Spectra on a Quantum Processor with an Error-Resilient Algorithm”, *Phys. Rev. X* **8**, 011021 (2018).
- [152] I. G. Ryabinkin, T.-C. Yen, S. N. Genin, and A. F. Izmaylov, “Qubit Coupled Cluster Method: A Systematic Approach to Quantum Chemistry on a Quantum Computer”, *J. Chem. Theory Comput.* **14**, 6317–6326 (2018).
- [153] Z. Li, X. Liu, H. Wang, S. Ashhab, J. Cui, H. Chen, X. Peng, and J. Du, “Quantum Simulation of Resonant Transitions for Solving the Eigenproblem of an Effective Water Hamiltonian”, *Phys. Rev. Lett.* **122**, 090504 (2019).
- [154] A. J. McCaskey, Z. P. Parks, J. Jakowski, S. V. Moore, T. D. Morris, T. S. Humble, and R. C. Pooser, “Quantum chemistry as a benchmark for near-term quantum computers”, *npj Quantum Inf.* **5**, 1–8 (2019).
- [155] S. E. Smart and D. A. Mazziotti, “Quantum-classical hybrid algorithm using an error-mitigating  $\mathbb{N}$ -representability condition to compute the Mott metal-insulator transition”, *Phys. Rev. A* **100**, 022517 (2019).

- [156] Y. Nam et al., “Ground-state energy estimation of the water molecule on a trapped-ion quantum computer”, *npj Quantum Inf.* **6**, 1–6 (2020).
- [157] F. Arute et al., “Hartree-Fock on a superconducting qubit quantum computer”, *Science* **369**, 1084–1089 (2020).
- [158] Q. Gao, H. Nakamura, T. P. Gujarati, G. O. Jones, J. E. Rice, S. P. Wood, M. Pistoia, J. M. Garcia, and N. Yamamoto, “Computational Investigations of the Lithium Superoxide Dimer Rearrangement on Noisy Quantum Devices”, *J. Phys. Chem. A* **125**, 1827–1836 (2021).
- [159] Q. Gao, G. O. Jones, M. Motta, M. Sugawara, H. C. Watanabe, T. Kobayashi, E. Watanabe, Y.-y. Ohnishi, H. Nakamura, and N. Yamamoto, “Applications of quantum computing for investigations of electronic transitions in phenylsulfonyl-carbazole TADF emitters”, *npj Comput. Mater.* **7**, 1–9 (2021).
- [160] X. Yuan, S. Endo, Q. Zhao, Y. Li, and S. C. Benjamin, “Theory of variational quantum simulation”, *Quantum* **3**, 191 (2019).
- [161] Y. Li and S. C. Benjamin, “Efficient Variational Quantum Simulator Incorporating Active Error Minimization”, *Phys. Rev. X* **7**, 021050 (2017).
- [162] C. Cîrstoiu, Z. Holmes, J. Iosue, L. Cincio, P. J. Coles, and A. Sornborger, “Variational fast forwarding for quantum simulation beyond the coherence time”, *npj Quantum Inf.* **6**, 1–10 (2020).
- [163] M. Benedetti, M. Fiorentini, and M. Lubasch, “Hardware-efficient variational quantum algorithms for time evolution”, *Phys. Rev. Research* **3**, 033083 (2021).
- [164] Y.-X. Yao, N. Gomes, F. Zhang, C.-Z. Wang, K.-M. Ho, T. Iadecola, and P. P. Orth, “Adaptive Variational Quantum Dynamics Simulations”, *PRX Quantum* **2**, 030307 (2021).

- [165] S. Barison, F. Vicentini, and G. Carleo, “An efficient quantum algorithm for the time evolution of parameterized circuits”, *Quantum* **5**, 512 (2021).
- [166] N. F. Berthussen, T. V. Trevisan, T. Iadecola, and P. P. Orth, “Quantum dynamics simulations beyond the coherence time on noisy intermediate-scale quantum hardware by variational Trotter compression”, *Phys. Rev. Research* **4**, 023097 (2022).
- [167] A. Delgado, J. M. Arrazola, S. Jahangiri, Z. Niu, J. Izaac, C. Roberts, and N. Killoran, “Variational quantum algorithm for molecular geometry optimization”, *Phys. Rev. A* **104**, 052402 (2021).
- [168] M. Cerezo, A. Arrasmith, R. Babbush, S. C. Benjamin, S. Endo, K. Fujii, J. R. McClean, K. Mitarai, X. Yuan, L. Cincio, and P. J. Coles, “Variational quantum algorithms”, *Nat. Rev. Phys.* **3**, 625–644 (2021).
- [169] J. Tilly, H. Chen, S. Cao, D. Picozzi, K. Setia, Y. Li, E. Grant, L. Wossnig, I. Rungger, G. H. Booth, and J. Tennyson, “The Variational Quantum Eigensolver: A review of methods and best practices”, *Phys. Rep.* **986**, 1–128 (2022).
- [170] L. Bittel and M. Kliesch, “Training Variational Quantum Algorithms Is NP-Hard”, *Phys. Rev. Lett.* **127**, 120502 (2021).
- [171] D. Wecker, M. B. Hastings, N. Wiebe, B. K. Clark, C. Nayak, and M. Troyer, “Solving strongly correlated electron models on a quantum computer”, *Phys. Rev. A* **92**, 062318 (2015).
- [172] I. D. Kivlichan, J. McClean, N. Wiebe, C. Gidney, A. Aspuru-Guzik, G. K.-L. Chan, and R. Babbush, “Quantum Simulation of Electronic Structure with Linear Depth and Connectivity”, *Phys. Rev. Lett.* **120**, 110501 (2018).

- [173] A. Anand, P. Schleich, S. Alperin-Lea, P. W. K. Jensen, S. Sim, M. Díaz-Tinoco, J. S. Kottmann, M. Degroote, A. F. Izmaylov, and A. Aspuru-Guzik, “A quantum computing view on unitary coupled cluster theory”, *Chem. Soc. Rev.* **51**, 1659–1684 (2022).
- [174] J. Romero, R. Babbush, J. R. McClean, C. Hempel, P. J. Love, and A. Aspuru-Guzik, “Strategies for quantum computing molecular energies using the unitary coupled cluster ansatz”, *Quantum Sci. Technol.* **4**, 014008 (2018).
- [175] F. A. Evangelista, G. K.-L. Chan, and G. E. Scuseria, “Exact parameterization of fermionic wave functions via unitary coupled cluster theory”, *J. Chem. Phys.* **151**, 244112 (2019).
- [176] Q. Wang, M. Li, C. Monroe, and Y. Nam, “Resource-Optimized Fermionic Local-Hamiltonian Simulation on a Quantum Computer for Quantum Chemistry”, *Quantum* **5**, 509 (2021).
- [177] J. S. Kottmann and A. Aspuru-Guzik, “Optimized low-depth quantum circuits for molecular electronic structure using a separable-pair approximation”, *Phys. Rev. A* **105**, 032449 (2022).
- [178] H. L. Tang, V. O. Shkolnikov, G. S. Barron, H. R. Grimsley, N. J. Mayhall, E. Barnes, and S. E. Economou, “Qubit-ADAPT-VQE: An Adaptive Algorithm for Constructing Hardware-Efficient Ansätze on a Quantum Processor”, *PRX Quantum* **2**, 020310 (2021).
- [179] M. Motta, K. J. Sung, K. B. Whaley, M. Head-Gordon, and J. Shee, “Bridging physical intuition and hardware efficiency for correlated electronic states: the local unitary cluster Jastrow ansatz for electronic structure”, *Chem. Sci.* **14**, 11213–11227 (2023).
- [180] J. R. McClean, S. Boixo, V. N. Smelyanskiy, R. Babbush, and H. Neven, “Barren plateaus in quantum neural network training landscapes”, *Nat. Commun.* **9**, 4812 (2018).

- [181] M. Larocca, S. Thanasilp, S. Wang, K. Sharma, J. Biamonte, P. J. Coles, L. Cincio, J. R. McClean, Z. Holmes, and M. Cerezo, *A Review of Barren Plateaus in Variational Quantum Computing*, 2024, [arXiv:2405.00781](#).
- [182] H. R. Grimsley, S. E. Economou, E. Barnes, and N. J. Mayhall, “An adaptive variational algorithm for exact molecular simulations on a quantum computer”, *Nat. Commun.* **10**, 3007 (2019).
- [183] H. R. Grimsley, G. S. Barron, E. Barnes, S. E. Economou, and N. J. Mayhall, “Adaptive, problem-tailored variational quantum eigensolver mitigates rough parameter landscapes and barren plateaus”, *npj Quantum Inf.* **9**, 1–8 (2023).
- [184] T. E. O’Brien et al., “Purification-based quantum error mitigation of pair-correlated electron simulations”, *Nat. Phys.* **19**, 1787–1792 (2023).
- [185] R. N. Tazhigulov, S.-N. Sun, R. Haghshenas, H. Zhai, A. T. Tan, N. C. Rubin, R. Babbush, A. J. Minnich, and G. K.-L. Chan, “Simulating Models of Challenging Correlated Molecules and Materials on the Sycamore Quantum Processor”, *PRX Quantum* **3**, 040318 (2022).
- [186] B. Nagy and F. Jensen, “Basis Sets in Quantum Chemistry”, in *Reviews in Computational Chemistry*, Vol. 30, edited by A. L. Parrill and K. B. Lipkowitz (John Wiley & Sons, Ltd, 2017) Chap. 3, pp. 93–149.
- [187] P. R. Hegde, O. Kyriienko, H. Heimonen, P. Tolas, G. Netzer, P. Barkoutsos, R. Vinuesa, I. Peng, and S. Markidis, “Beyond the Buzz: Strategic Paths for Enabling Useful NISQ Applications”, in *Proceedings of the 21st ACM International Conference on Computing Frontiers*, CF '24 (2024), pp. 310–313.
- [188] A. Bentellis, A. Matic-Flierl, C. B. Mendl, and J. M. Lorenz, “Benchmarking the Variational Quantum Eigensolver using different quantum hardware”, in *2023 IEEE*

- International Conference on Quantum Computing and Engineering (QCE), Vol. 01 (2023), pp. 518–523.
- [189] R. Schade, C. Bauer, K. Tamoev, L. Mazur, C. Plessl, and T. D. Kühne, “Parallel quantum chemistry on noisy intermediate-scale quantum computers”, *Phys. Rev. Research* **4**, 033160 (2022).
- [190] J. Robledo-Moreno, M. Motta, H. Haas, A. Javadi-Abhari, P. Jurcevic, W. Kirby, S. Martiel, K. Sharma, S. Sharma, T. Shirakawa, I. Sitdikov, R.-Y. Sun, K. J. Sung, M. Takita, M. C. Tran, S. Yunoki, and A. Mezzacapo, *Chemistry Beyond Exact Solutions on a Quantum-Centric Supercomputer*, 2024, [arXiv:2405.05068](https://arxiv.org/abs/2405.05068).
- [191] I.-O. Stamatescu, “Wave Function Collapse”, in *Compendium of Quantum Physics*, edited by D. Greenberger, K. Hentschel, and F. Weinert (Springer, Berlin, Heidelberg, 2009), pp. 813–822.
- [192] A. M. Childs and R. Kothari, “Limitations on the simulation of non-sparse hamiltonians”, *Quantum Info. Comput.* **10**, 669–684 (2010).
- [193] B. T. Sutcliffe, “Fundamentals of Computational Quantum Chemistry”, in *Computational Techniques in Quantum Chemistry and Molecular Physics*, Vol. 15, edited by G. H. F. Diercksen, B. T. Sutcliffe, and A. Veillard, NATO Advanced Study Institutes Series (1975), pp. 1–105.
- [194] I. Mayer, “The Born-Oppenheimer Hamiltonian”, in *Simple Theorems, Proofs, and Derivations in Quantum Chemistry*, edited by I. Mayer (Springer US, Boston, MA, 2003), pp. 1–18.
- [195] J. C. Slater, “Atomic Shielding Constants”, *Phys. Rev.* **36**, 57–64 (1930).

- [196] S. F. Boys and A. C. Egerton, “Electronic wave functions - I. A general method of calculation for the stationary states of any molecular system”, *Proc. R. Soc. A.* **200**, 542–554 (1950).
- [197] T. Helgaker, P. Jørgensen, and J. Olsen, *Molecular electronic-structure theory* (John Wiley & Sons, Ltd, 2000).
- [198] J. C. Slater, “The Theory of Complex Spectra”, *Phys. Rev.* **34**, 1293–1322 (1929).
- [199] A. Szabo and N. S. Ostlund, *Modern Quantum Chemistry: Introduction to Advanced Electronic Structure Theory* (Courier Corporation, 1996).
- [200] G. M. J. Barca, A. T. B. Gilbert, and P. M. W. Gill, “Communication: Hartree-Fock description of excited states of H<sub>2</sub>”, *J. Chem. Phys.* **141**, 111104 (2014).
- [201] E. U. Condon, “The Theory of Complex Spectra”, *Phys. Rev.* **36**, 1121–1133 (1930).
- [202] S. Lehtola, F. Blockhuys, and C. Van Alsenoy, “An Overview of Self-Consistent Field Calculations Within Finite Basis Sets”, *Molecules* **25**, 1218 (2020).
- [203] T. Van Voorhis and M. Head-Gordon, “A geometric approach to direct minimization”, *Mol. Phys.* **100**, 1713–1721 (2002).
- [204] P. Pulay, “Convergence acceleration of iterative sequences. the case of scf iteration”, *Chem. Phys. Lett.* **73**, 393–398 (1980).
- [205] P. Pulay, “Improved SCF convergence acceleration”, *J. Comput. Chem.* **3**, 556–560 (1982).
- [206] K. N. Kudin, G. E. Scuseria, and E. Cancès, “A black-box self-consistent field convergence algorithm: One step closer”, *J. Chem. Phys.* **116**, 8255–8261 (2002).
- [207] X. Hu and W. Yang, “Accelerating self-consistent field convergence with the augmented Roothaan–Hall energy function”, *J. Chem. Phys.* **132**, 054109 (2010).

- [208] J. T. Seeley, M. J. Richard, and P. J. Love, “The Bravyi-Kitaev transformation for quantum computation of electronic structure”, *J. Chem. Phys.* **137**, 224109 (2012).
- [209] A. Tranter, P. J. Love, F. Mintert, and P. V. Coveney, “A Comparison of the Bravyi–Kitaev and Jordan–Wigner Transformations for the Quantum Simulation of Quantum Chemistry”, *J. Chem. Theory Comput.* **14**, 5617–5630 (2018).
- [210] W. J. Huggins, J. R. McClean, N. C. Rubin, Z. Jiang, N. Wiebe, K. B. Whaley, and R. Babbush, “Efficient and noise resilient measurements for quantum chemistry on near-term quantum computers”, *npj Quantum Inf.* **7**, 1–9 (2021).
- [211] J. M. Kübler, A. Arrasmith, L. Cincio, and P. J. Coles, “An Adaptive Optimizer for Measurement-Frugal Variational Algorithms”, *Quantum* **4**, 263 (2020).
- [212] W. R. Clements, P. C. Humphreys, B. J. Metcalf, W. S. Kolthammer, and I. A. Walmsley, “Optimal design for universal multiport interferometers”, *Optica* **3**, 1460–1465 (2016).
- [213] M. Reck, A. Zeilinger, H. J. Bernstein, and P. Bertani, “Experimental realization of any discrete unitary operator”, *Phys. Rev. Lett.* **73**, 58–61 (1994).
- [214] A. F. Izmaylov, M. Díaz-Tinoco, and R. A. Lang, “On the order problem in construction of unitary operators for the variational quantum eigensolver”, *Phys. Chem. Chem. Phys.* **22**, 12980–12986 (2020).
- [215] I. G. Ryabinkin, S. N. Genin, and A. F. Izmaylov, “Constrained Variational Quantum Eigensolver: Quantum Computer Search Engine in the Fock Space”, *J. Chem. Theory Comput.* **15**, 249–255 (2019).
- [216] C. Møller, “Note on an Approximation Treatment for Many-Electron Systems”, *Phys. Rev.* **46**, 618–622 (1934).
- [217] D. Cremer, “Møller–Plesset perturbation theory: from small molecule methods to methods for thousands of atoms”, *WIREs Comput. Mol. Sci.* **1**, 509–530 (2011).

- [218] J. A. Pople, J. S. Binkley, and R. Seeger, “Theoretical models incorporating electron correlation”, *Int. J. Quantum Chem.* **10**, 1–19 (1976).
- [219] J. Li, B. A. Jones, and S. Kais, “Toward perturbation theory methods on a quantum computer”, *Sci. Adv.* **9**, eadg4576 (2023).
- [220] U. Bozkaya, “Orbital-Optimized MP3 and MP2.5 with Density-Fitting and Cholesky Decomposition Approximations”, *J. Chem. Theory Comput.* **12**, 1179–1188 (2016).
- [221] N. T. Le and L. N. Tran, “Correlated Reference-Assisted Variational Quantum Eigensolver”, *J. Phys. Chem. A* **127**, 5222–5230 (2023).
- [222] T. B. Pedersen, F. Aquilante, and R. Lindh, “Density fitting with auxiliary basis sets from Cholesky decompositions”, *Theor. Chem. Acc.* **124**, 1–10 (2009).
- [223] D. Poulin, M. B. Hastings, D. Wecker, N. Wiebe, A. C. Doberty, and M. Troyer, “The trotter step size required for accurate quantum simulation of quantum Chemistry”, *Quantum Info. Comput.* **15**, 361–384 (2015).
- [224] D. W. Berry, C. Gidney, M. Motta, J. R. McClean, and R. Babbush, “Qubitization of Arbitrary Basis Quantum Chemistry Leveraging Sparsity and Low Rank Factorization”, *Quantum* **3**, 208 (2019).
- [225] M. Motta, E. Ye, J. R. McClean, Z. Li, A. J. Minnich, R. Babbush, and G. K.-L. Chan, “Low rank representations for quantum simulation of electronic structure”, *npj Quantum Inf.* **7**, 1–7 (2021).
- [226] J. Gauss, S. Blaschke, S. Burger, T. Nottoli, F. Lipparini, and S. Stopkowicz, “Cholesky decomposition of two-electron integrals in quantum-chemical calculations with perturbative or finite magnetic fields using gauge-including atomic orbitals”, *Mol. Phys.* **121**, e2101562 (2023).

- [227] U. Bozkaya, J. M. Turney, Y. Yamaguchi, H. F. Schaefer, and C. D. Sherrill, “Quadratically convergent algorithm for orbital optimization in the orbital-optimized coupled-cluster doubles method and in orbital-optimized second-order Møller-Plesset perturbation theory”, *J. Chem. Phys.* **135**, 104103 (2011).
- [228] U. Bozkaya and C. D. Sherrill, “Analytic energy gradients for the orbital-optimized second-order Møller–Plesset perturbation theory”, *J. Chem. Phys.* **138**, 184103 (2013).
- [229] C. K. Kim and S. K. You, *The Functional Schrödinger Picture Approach to Many-Particle Systems*, 2002, [arXiv:cond-mat/0212557](https://arxiv.org/abs/cond-mat/0212557).
- [230] P. M. Stevenson, “Optimized perturbation theory”, *Phys. Rev. D* **23**, 2916–2944 (1981).
- [231] A. Okopińska, “Nonstandard expansion techniques for the effective potential in  $\Lambda$  4 quantum field theory”, *Phys. Rev. D* **35**, 1835–1847 (1987).
- [232] S. Yalouz, B. Senjean, J. Günther, F. Buda, T. E. O’Brien, and L. Visscher, “A state-averaged orbital-optimized hybrid quantum–classical algorithm for a democratic description of ground and excited states”, *Quantum Sci. Technol.* **6**, 024004 (2021).
- [233] K. M. Nakanishi, K. Mitarai, and K. Fujii, “Subspace-search variational quantum eigensolver for excited states”, *Phys. Rev. Research* **1**, 033062 (2019).
- [234] N. H. Stair and F. A. Evangelista, “Simulating Many-Body Systems with a Projective Quantum Eigensolver”, *PRX Quantum* **2**, 030301 (2021).
- [235] Y. S. Yordanov, D. R. M. Arvidsson-Shukur, and C. H. W. Barnes, “Efficient quantum circuits for quantum computational chemistry”, *Phys. Rev. A* **102**, 062612 (2020).
- [236] D. Aharonov, V. Jones, and Z. Landau, “A Polynomial Quantum Algorithm for Approximating the Jones Polynomial”, *Algorithmica* **55**, 395–421 (2009).

- [237] A. Barenco, A. Berthiaume, D. Deutsch, A. Ekert, R. Jozsa, and C. Macchiavello, “Stabilization of Quantum Computations by Symmetrization”, *SIAM J. Comput.* **26**, 1541–1557 (1997).
- [238] A. Barenco, C. H. Bennett, R. Cleve, D. P. DiVincenzo, N. Margolus, P. Shor, T. Sleator, J. A. Smolin, and H. Weinfurter, “Elementary gates for quantum computation”, *Phys. Rev. A* **52**, 3457–3467 (1995).
- [239] D. G. A. Smith et al., “PSI4 1.4: Open-source software for high-throughput quantum chemistry”, *J. Chem. Phys.* **152**, 184108 (2020).
- [240] J.R. McClean et al., “OpenFermion: the electronic structure package for quantum computers”, *Quantum Sci. Technol.* **5**, 034014 (2020).
- [241] J. D. Whitfield, J. Biamonte, and A. Aspuru-Guzik, “Simulation of electronic structure Hamiltonians using quantum computers”, *Mol. Phys.* **109**, 735–750 (2011).
- [242] P. Virtanen et al., “SciPy 1.0: fundamental algorithms for scientific computing in Python”, *Nat. Methods* **17**, 261–272 (2020).
- [243] G. Aleksandrowicz et al., *Qiskit: An Open-source Framework for Quantum Computing*, Zenodo, 2019.
- [244] K. Wright et al., “Benchmarking an 11-qubit quantum computer”, *Nat. Commun.* **10**, 5464 (2019).
- [245] D. Gottesman, *An Introduction to Quantum Error Correction and Fault-Tolerant Quantum Computation*, 2009, [arXiv:0904.2557](https://arxiv.org/abs/0904.2557).
- [246] J. Spall, “Implementation of the simultaneous perturbation algorithm for stochastic optimization”, *IEEE Trans. Aerosp. Electron. Syst.* **34**, 817–823 (1998).
- [247] M. R. Bonyadi and Z. Michalewicz, “Particle Swarm Optimization for Single Objective Continuous Space Problems: A Review”, *Evol. Comput.* **25**, 1–54 (2017).

- [248] J. M. Arrazola, O. Di Matteo, N. Quesada, S. Jahangiri, A. Delgado, and N. Killoran, “Universal quantum circuits for quantum chemistry”, *Quantum* **6**, 742 (2022), [arXiv:2106.13839](#).
- [249] G.-L. R. Anselmetti, D. Wierichs, C. Gogolin, and R. M. Parrish, “Local, expressive, quantum-number-preserving VQE ansätze for fermionic systems”, *New J. Phys.* **23**, 113010 (2021).
- [250] I. Magoulas and F. A. Evangelista, “CNOT-Efficient Circuits for Arbitrary Rank Many-Body Fermionic and Qubit Excitations”, *J. Chem. Theory Comput.* **19**, 822–836 (2023).
- [251] C. H. Chee, A. M. Mak, D. Leykam, P. K. Barkoutsos, and D. G. Angelakis, “Computing electronic correlation energies using linear depth quantum circuits”, *Quantum Sci. Technol.* **9**, 025003 (2024).
- [252] I. Kerenidis and A. Prakash, *Quantum machine learning with subspace states*, 2022, [arXiv:2202.00054](#).
- [253] G. W. Stewart, “Computing the CS decomposition of a partitioned orthonormal matrix”, *Numer. Math.* **40**, 297–306 (1982).
- [254] E. S. Gawlik, Y. Nakatsukasa, and B. D. Sutton, “A Backward Stable Algorithm for Computing the CS Decomposition via the Polar Decomposition”, *SIAM J. Matrix Anal. Appl.* **39**, 1448–1469 (2018).
- [255] S. Johri, S. Debnath, A. Mocherla, A. Singk, A. Prakash, J. Kim, and I. Kerenidis, “Nearest centroid classification on a trapped ion quantum computer”, *npj Quantum Inf.* **7**, 1–11 (2021).
- [256] K. Wan, W. J. Huggins, J. Lee, and R. Babbush, “Matchgate Shadows for Fermionic Quantum Simulation”, *Commun. Math. Phys.* **404**, 629–700 (2023).

- [257] G. Ortiz, J. E. Gubernatis, E. Knill, and R. Laflamme, “Quantum algorithms for fermionic simulations”, *Phys. Rev. A* **64**, 022319 (2001).
- [258] Z. Jiang, K. J. Sung, K. Kechedzhi, V. N. Smelyanskiy, and S. Boixo, “Quantum Algorithms to Simulate Many-Body Physics of Correlated Fermions”, *Phys. Rev. Appl.* **9**, 044036 (2018).
- [259] I. Kerenidis, J. Landman, and N. Mathur, *Classical and Quantum Algorithms for Orthogonal Neural Networks*, 2021, [arXiv:2106.07198](https://arxiv.org/abs/2106.07198).
- [260] A. Vourdas, “Exterior calculus and fermionic quantum computation”, *J. Phys. A* **51**, 445301 (2018).
- [261] M. Kjaergaard, M. E. Schwartz, J. Braumüller, P. Krantz, J. I.-J. Wang, S. Gustavsson, and W. D. Oliver, “Superconducting Qubits: Current State of Play”, *Annu. Rev. Condens. Matter Phys.* **11**, 369–395 (2020).
- [262] J. M. L. Martin, “Ab initio total atomization energies of small molecules — towards the basis set limit”, *Chem. Phys. Lett.* **259**, 669–678 (1996).
- [263] A. Halkier, T. Helgaker, P. Jørgensen, W. Klopper, and J. Olsen, “Basis-set convergence of the energy in molecular Hartree–Fock calculations”, *Chem. Phys. Lett.* **302**, 437–446 (1999).
- [264] P. R. Spackman and A. Karton, “Estimating the CCSD basis-set limit energy from small basis sets: basis-set extrapolations vs additivity schemes”, *AIP Advances* **5**, 057148 (2015).
- [265] C. Plascencia, J. Wang, and A. K. Wilson, “Importance of the ligand basis set in ab initio thermochemical calculations of transition metal species”, *Chem. Phys. Lett.* **685**, 496–503 (2017).

- [266] Q. Sun, T. C. Berkelbach, N. S. Blunt, G. H. Booth, S. Guo, Z. Li, J. Liu, J. D. McClain, E. R. Sayfutyarova, S. Sharma, S. Wouters, and G. K.-L. Chan, “PySCF: the Python-based simulations of chemistry framework”, *WIREs Comput. Mol. Sci.* **8**, e1340 (2018).
- [267] V. Bergholm et al., *PennyLane: Automatic differentiation of hybrid quantum-classical computations*, 2022, [arXiv:1811.04968](https://arxiv.org/abs/1811.04968).
- [268] H. F. Trotter, “On the product of semi-groups of operators”, *Proc. Amer. Math. Soc.* **10**, 545–551 (1959).
- [269] D. W. Berry, A. M. Childs, R. Cleve, R. Kothari, and R. D. Somma, “Exponential improvement in precision for simulating sparse Hamiltonians”, in *Proceedings of the forty-sixth annual ACM symposium on Theory of computing*, STOC '14 (2014), pp. 283–292.
- [270] A. M. Childs, A. Ostrander, and Y. Su, “Faster quantum simulation by randomization”, *Quantum* **3**, 182 (2019).
- [271] E. Campbell, “Random Compiler for Fast Hamiltonian Simulation”, *Phys. Rev. Lett.* **123**, 070503 (2019).
- [272] Y. Ouyang, D. R. White, and E. T. Campbell, “Compilation by stochastic Hamiltonian sparsification”, *Quantum* **4**, 235 (2020).
- [273] D. An, D. Fang, and L. Lin, “Time-dependent Hamiltonian Simulation of Highly Oscillatory Dynamics and Superconvergence for Schrödinger Equation”, *Quantum* **6**, 690 (2022).
- [274] G. H. Low and N. Wiebe, *Hamiltonian Simulation in the Interaction Picture*, 2019, [arXiv:1805.00675](https://arxiv.org/abs/1805.00675).
- [275] A. Rajput, A. Roggero, and N. Wiebe, “Hybridized Methods for Quantum Simulation in the Interaction Picture”, *Quantum* **6**, 780 (2022).

- [276] Y.-H. Chen, A. Kalev, and I. Hen, “Quantum Algorithm for Time-Dependent Hamiltonian Simulation by Permutation Expansion”, *PRX Quantum* **2**, 030342 (2021).
- [277] L. Clinton, J. Bausch, and T. Cubitt, “Hamiltonian simulation algorithms for near-term quantum hardware”, *Nat. Commun.* **12**, 4989 (2021).
- [278] A. Miessen, P. J. Ollitrault, and I. Tavernelli, “Quantum algorithms for quantum dynamics: A performance study on the spin-boson model”, *Phys. Rev. Res.* **3**, 043212 (2021).
- [279] A. D. McLachlan and M. A. Ball, “Time-Dependent Hartree—Fock Theory for Molecules”, *Rev. Mod. Phys.* **36**, 844–855 (1964).
- [280] K. Mitarai and K. Fujii, “Methodology for replacing indirect measurements with direct measurements”, *Phys. Rev. Res.* **1**, 013006 (2019).
- [281] K. Bharti and T. Haug, “Quantum-assisted simulator”, *Phys. Rev. A* **104**, 042418 (2021).
- [282] T. Haug and K. Bharti, “Generalized quantum assisted simulator”, *Quantum Sci. Technol.* **7**, 045019 (2022).
- [283] K. H. Lim, T. Haug, L. C. Kwek, and K. Bharti, “Fast-forwarding with NISQ processors without feedback loop”, *Quantum Sci. Technol.* **7**, 015001 (2021).
- [284] J. W. Z. Lau, T. Haug, L.-C. Kwek, and K. Bharti, “NISQ Algorithm for Hamiltonian simulation via truncated Taylor series”, *SciPost Physics* **12**, 122 (2022).
- [285] B. Wu, M. Ray, L. Zhao, X. Sun, and P. Rebentrost, “Quantum-classical algorithms for skewed linear systems with an optimized Hadamard test”, *Phys. Rev. A* **103**, 042422 (2021).
- [286] V. V. Shende and I. L. Markov, “On the CNOT-cost of TOFFOLI gates”, *Quantum Info. Comput.* **9**, 461–486 (2009).

- [287] C. Chevallier, J. Vovrosh, J. de Hond, M. Dagrada, A. Dauphin, and V. E. Elfving, “Variational protocols for emulating digital gates using analog control with always-on interactions”, *Phys. Rev. A* **109**, 062604 (2024).
- [288] J. Wang, S. Paesani, R. Santagati, S. Knauer, A. A. Gentile, N. Wiebe, M. Petruzzella, J. L. O’Brien, J. G. Rarity, A. Laing, and M. G. Thompson, “Experimental quantum Hamiltonian learning”, *Nat. Phys.* **13**, 551–555 (2017).
- [289] M. Serbyn, D. A. Abanin, and Z. Papić, “Quantum many-body scars and weak breaking of ergodicity”, *Nat. Phys.* **17**, 675–685 (2021).
- [290] G.-X. Su, H. Sun, A. Hudomal, J.-Y. Desaulles, Z.-Y. Zhou, B. Yang, J. C. Halimeh, Z.-S. Yuan, Z. Papić, and J.-W. Pan, “Observation of many-body scarring in a Bose-Hubbard quantum simulator”, *Phys. Rev. Res.* **5**, 023010 (2023).
- [291] N. S. Blunt, G. P. Gehér, and A. E. Moylett, “Compilation of a simple chemistry application to quantum error correction primitives”, *Phys. Rev. Research* **6**, 013325 (2024).
- [292] W. J. Huggins, O. Leimkuhler, T. F. Stetina, and K. B. Whaley, *Efficient state preparation for the quantum simulation of molecules in first quantization*, June 2024, [arXiv:2407.00249](https://arxiv.org/abs/2407.00249).
- [293] D. Traore, O. Adjoua, C. Feniou, I.-M. Lygatsika, Y. Maday, E. Posenitskiy, K. Hammernik, A. Peruzzo, J. Toulouse, E. Giner, and J.-P. Piquemal, *Shortcut to Chemically Accurate Quantum Computing via Density-based Basis-set Correction*, May 2024, [arXiv:2405.11567](https://arxiv.org/abs/2405.11567).
- [294] Y.-A. Chen, A. V. Gorshkov, and Y. Xu, “Error-correcting codes for fermionic quantum simulation”, *SciPost Phys.* **16**, 033 (2024).

- [295] G. Kin-Lic Chan, “Quantum chemistry, classical heuristics, and quantum advantage”, *Faraday Discuss.*, **10**, 1039/D4FD00141A (2024).
- [296] R. Babbush, D. W. Berry, R. Kothari, R. D. Somma, and N. Wiebe, “Exponential Quantum Speedup in Simulating Coupled Classical Oscillators”, *Phys. Rev. X* **13**, 041041 (2023).
- [297] S. S. Kale and S. Kais, “Simulation of Chemical Reactions on a Quantum Computer”, *J. Phys. Chem. Lett.* **15**, 5633–5642 (2024).
- [298] G. Mazzola, “Quantum computing for chemistry and physics applications from a Monte Carlo perspective”, *J. Chem. Phys.* **160**, 010901 (2024).
- [299] B. Bauer, D. Wecker, A. J. Millis, M. B. Hastings, and M. Troyer, “Hybrid Quantum-Classical Approach to Correlated Materials”, *Phys. Rev. X* **6**, 031045 (2016).
- [300] J. M. Kreula, S. R. Clark, and D. Jaksch, “Non-linear quantum-classical scheme to simulate non-equilibrium strongly correlated fermionic many-body dynamics”, *Sci. Rep.* **6**, 32940 (2016).
- [301] N. C. Rubin, *A Hybrid Classical/Quantum Approach for Large-Scale Studies of Quantum Systems with Density Matrix Embedding Theory*, 2016, [arXiv:1610.06910](https://arxiv.org/abs/1610.06910).
- [302] T. Yamazaki, S. Matsuura, A. Narimani, A. Saidmuradov, and A. Zaribafiyani, *Towards the Practical Application of Near-Term Quantum Computers in Quantum Chemistry Simulations: A Problem Decomposition Approach*, 2018, [arXiv:1806.01305](https://arxiv.org/abs/1806.01305).
- [303] A. Katabarwa, K. Gratsea, A. Caesura, and P. D. Johnson, “Early Fault-Tolerant Quantum Computing”, *PRX Quantum* **5**, 020101 (2024).
- [304] V. Balasubramanian, M. DeCross, A. Kar, and O. Parrikar, “Binding complexity and multiparty entanglement”, *J. High Energ. Phys.* **2019**, 69 (2019).

# Appendix A

## Shallow Circuits for Efficient Correlated State Preparation

### A.1 Proof of Equivalence between Two Definitions of an Arbitrary Slater Determinant

An arbitrary Slater determinant  $|\Psi_1(\mathbf{A})\rangle$  with  $d$  occupied and  $N - d$  unoccupied fermionic modes is defined as

$$|\Psi_1(\mathbf{A})\rangle = \prod_{l=1}^d \prod_{k=1}^N A_{lk} \hat{a}_k^\dagger |\text{vac}\rangle, \quad (\text{A.1})$$

where  $\mathbf{A}$  is an  $N \times d$  real matrix such that all the  $d$  columns are orthogonal and normalized,  $|\text{vac}\rangle$  is a fermionic vacuum state, and  $\hat{a}_k^\dagger$  is a creation operator acting on the  $k^{\text{th}}$  mode.

Begin by expanding the product in Eq. (A.1) and replacing the index  $k$  in the summation

with indices  $k_1, \dots, k_d$ ,

$$|\Psi_1(\mathbf{A})\rangle = \prod_{k_d=1}^N A_{dk_d} \hat{a}_{k_d}^\dagger \dots \prod_{k_1=1}^N A_{1k_1} \hat{a}_{k_1}^\dagger |\text{vac}\rangle \quad (\text{A.2})$$

$$= \prod_{k_d, \dots, k_1=1}^N A_{dk_d} \dots A_{1k_1} \hat{a}_{k_d}^\dagger \dots \hat{a}_{k_1}^\dagger |\text{vac}\rangle, \quad (\text{A.3})$$

The aim is to show that Eq. (A.3) is equivalent to the alternate definition of the Slater determinant,

$$|\Psi_{1,\text{alt}}(\mathbf{A})\rangle = \prod_{l=1}^d \prod_{k=1}^N A_{lk} \hat{a}_k^\dagger + \hat{a}_k |\text{vac}\rangle, \quad (\text{A.4})$$

where  $\hat{a}_k^\dagger + \hat{a}_k$  is an anti-commuting operator. Starting from Eq. (A.4), expand the product and replace index  $k$  in the summation with indices  $k_1, \dots, k_d$ ,

$$|\Psi_{1,\text{alt}}(\mathbf{A})\rangle = \prod_{k_d=1}^N A_{dk_d} \hat{a}_{k_d}^\dagger + \hat{a}_{k_d} \dots \prod_{k_1=1}^N A_{1k_1} \hat{a}_{k_1}^\dagger + \hat{a}_{k_1} |\text{vac}\rangle. \quad (\text{A.5})$$

Here, consider evaluating the product of the rightmost two summation terms in Eq. (A.5). Now, the derivation is split into two cases  $d = 1$  and  $d > 1$ . For  $d = 1$ , note that  $\hat{a}_j |\text{vac}\rangle = 0$  for any mode  $j$ , thus both Eq. (A.3) and (A.5) become trivially equivalent. For  $d > 1$ ,

$$\begin{aligned} & \prod_{k_2=1}^N A_{2k_2} \hat{a}_{k_2}^\dagger + \hat{a}_{k_2} \prod_{k_1=1}^N A_{1k_1} \hat{a}_{k_1}^\dagger + \hat{a}_{k_1} \\ = & \prod_{k_2, k_1=1}^N A_{2k_2} A_{1k_1} \hat{a}_{k_2}^\dagger + \hat{a}_{k_2} \hat{a}_{k_1}^\dagger + \hat{a}_{k_1} \end{aligned} \quad (\text{A.6})$$

$$= \prod_{k_2, k_1=1}^N A_{2k_2} A_{1k_1} \hat{a}_{k_2}^\dagger \hat{a}_{k_1}^\dagger + \hat{a}_{k_2}^\dagger \hat{a}_{k_1} + \hat{a}_{k_2} \hat{a}_{k_1}^\dagger + \hat{a}_{k_2} \hat{a}_{k_1}. \quad (\text{A.7})$$

Then, apply the fermionic commutation relation  $\{\hat{a}_i, \hat{a}_j^\dagger\} = \mathbf{I}$  to Eq. (A.7) to get,

$$= \prod_{k_2, k_1=1}^N A_{2k_2} A_{1k_1} \hat{a}_{k_2}^\dagger \hat{a}_{k_1}^\dagger + \prod_{k_2, k_1=1}^N \mathbf{I} + \hat{a}_{k_2} \hat{a}_{k_1} \quad , \quad (\text{A.8})$$

and since the columns of  $\mathbf{A}$  are orthogonal, the inner product between any column  $i, j$  vanishes

$\sum_k A_{ik} A_{jk} = 0$ , thus

$$= \prod_{k_2, k_1=1}^N A_{2k_2} A_{1k_1} \hat{a}_{k_2}^\dagger \hat{a}_{k_1}^\dagger + \hat{a}_{k_2} \hat{a}_{k_1} \quad . \quad (\text{A.9})$$

Substituting Eq. (A.9) back into Eq. (A.5), and using  $\hat{a}_j/\text{vac} = 0$  for any mode  $j$  gives

$$|\Psi_{1,\text{alt}}(\mathbf{A})\rangle = \prod_{k_d=1}^N A_{dk_d} \hat{a}_{k_d}^\dagger + \hat{a}_{k_d} \quad \dots \quad \prod_{k_2, k_1=1}^N A_{2k_2} A_{1k_1} \hat{a}_{k_2}^\dagger \hat{a}_{k_1}^\dagger \quad / \text{vac} \quad . \quad (\text{A.10})$$

Henceforth, consider the even and odd  $d$  cases separately. First, assuming  $d$  is even, consider reapplying the result Eq. (A.9) to the rest of the pairs of summation terms in Eq. (A.10), which yields

$$|\Psi_{1,\text{alt}}(\mathbf{A})\rangle = \prod_{k_d, k_{d-1}=1}^N A_{dk_d} A_{d-1k_{d-1}} \hat{a}_{k_d}^\dagger \hat{a}_{k_{d-1}}^\dagger \quad \dots \quad \prod_{k_2, k_1=1}^N A_{2k_2} A_{1k_1} \hat{a}_{k_2}^\dagger \hat{a}_{k_1}^\dagger \quad / \text{vac} \quad (\text{A.11})$$

$$= \prod_{k_d, \dots, k_1=1}^N A_{dk_d} \dots A_{1k_1} \hat{a}_{k_d}^\dagger \dots \hat{a}_{k_1}^\dagger / \text{vac} \quad . \quad (\text{A.12})$$

Alternatively, if  $d$  is odd, then

$$|\Psi_{1,\text{alt}}(\mathbf{A})\rangle = \sum_{k_d=1}^N A_{dk_d} \hat{a}_{k_d}^\dagger + \hat{a}_{k_d} \sum_{k_{d-1}, \dots, k_1=1}^N A_{d-1k_{d-1}} \dots A_{1k_1} \hat{a}_{k_{d-1}}^\dagger \dots \hat{a}_{k_1}^\dagger / \text{vac} \quad (\text{A.13})$$

$$= \sum_{k_d, \dots, k_1=1}^N A_{dk_d} \dots A_{1k_1} \hat{a}_{k_d}^\dagger \hat{a}_{k_{d-1}}^\dagger \dots \hat{a}_{k_1}^\dagger + \hat{a}_{k_d} \hat{a}_{k_{d-1}}^\dagger \dots \hat{a}_{k_1}^\dagger / \text{vac} \quad (\text{A.14})$$

$$= \sum_{k_d, \dots, k_1=1}^N A_{dk_d} \dots A_{1k_1} \hat{a}_{k_d}^\dagger \hat{a}_{k_{d-1}}^\dagger \dots \hat{a}_{k_1}^\dagger + \sum_{k_d k_{d-1}} \hat{a}_{k_{d-2}}^\dagger \dots \hat{a}_{k_1}^\dagger - \hat{a}_{k_{d-1}}^\dagger \hat{a}_{k_d} \hat{a}_{k_{d-2}}^\dagger \dots \hat{a}_{k_1}^\dagger / \text{vac} \quad (\text{A.15})$$

$$= \sum_{k_d, \dots, k_1=1}^N A_{dk_d} \dots A_{1k_1} \hat{a}_{k_d}^\dagger \hat{a}_{k_{d-1}}^\dagger \dots \hat{a}_{k_1}^\dagger - \hat{a}_{k_{d-1}}^\dagger \sum_{k_d k_{d-2}} \hat{a}_{k_{d-3}}^\dagger \dots \hat{a}_{k_1}^\dagger + \hat{a}_{k_{d-1}}^\dagger \hat{a}_{k_{d-2}}^\dagger \hat{a}_{k_d} \hat{a}_{k_{d-3}}^\dagger \dots \hat{a}_{k_1}^\dagger / \text{vac} \quad (\text{A.16})$$

$$= \sum_{k_d, \dots, k_1=1}^N A_{dk_d} \dots A_{1k_1} \hat{a}_{k_d}^\dagger \dots \hat{a}_{k_1}^\dagger / \text{vac} , \quad (\text{A.17})$$

where the fermionic commutation relation in Eq. (A.14) and matrix orthogonality in Eq. (A.15), (A.16) are applied. Hence, by combining the even Eq. (A.12) and odd Eq. (A.17) results, the equivalence between the alternative definition in Eq. (A.4) to the original definition in Eq. (A.1) is established.

## A.2 Proof of Anti-Commutation Relations

Here, the aim is to show that  $\rho_k = \hat{a}_k^\dagger + \hat{a}_k$  has the desired anti-commutation relation  $\{\rho_i, \rho_j\} = 2 \delta_{ij} \mathbf{I}$ .

$$\{\rho_i, \rho_j\} = \{\hat{a}_i^\dagger + \hat{a}_i, \hat{a}_j^\dagger + \hat{a}_j\} \quad (\text{A.18})$$

$$= (\hat{a}_i^\dagger + \hat{a}_i)(\hat{a}_j^\dagger + \hat{a}_j) + (\hat{a}_j^\dagger + \hat{a}_j)(\hat{a}_i^\dagger + \hat{a}_i) \quad (\text{A.19})$$

$$= \hat{a}_i^\dagger \hat{a}_j^\dagger + \hat{a}_i \hat{a}_j^\dagger + \hat{a}_i^\dagger \hat{a}_j + \hat{a}_i \hat{a}_j + \hat{a}_j^\dagger \hat{a}_i^\dagger + \hat{a}_j \hat{a}_i^\dagger + \hat{a}_j^\dagger \hat{a}_i + \hat{a}_j \hat{a}_i \quad (\text{A.20})$$

$$= \hat{a}_i \hat{a}_j^\dagger + \hat{a}_i^\dagger \hat{a}_j + \hat{a}_j \hat{a}_i^\dagger + \hat{a}_j^\dagger \hat{a}_i \quad (\text{A.21})$$

$$= 2 \delta_{ij} \mathbf{I} \quad (\text{shown}). \quad (\text{A.22})$$

Next, the aim is to show that

$$\rho_\mu^{(L)} = \prod_{r=1}^{\mu-1} \hat{Z}_{rL} \prod_{r=L(\mu-1)+1}^{\mu L} \hat{X}_r, \quad (\text{A.23})$$

used to incorporate  $L$ -wise correlation into the Clifford loaders via the Givens rotation approach has the desired anti-commutation relation  $\{\rho_\mu^{(L)}, \rho^{(L)}\} = 2 \delta_{\mu} \mathbf{I}$ . Here, the Pauli-Z subscript  $rL = r \cdot L$  refers to the qubit order. Now, the derivation is split into two cases  $\mu = \frac{L}{2}$  and  $\mu < \frac{L}{2}$ .

First, consider  $\mu = \frac{L}{2}$ , where

$$2\rho_\mu^{(L)} \rho_\mu^{(L)} = 2 \prod_{r=1}^{\mu-1} \hat{Z}_{rL} \prod_{r=L(\mu-1)+1}^{\mu L} \hat{X}_r \prod_{s=1}^{\mu-1} \hat{Z}_{sL} \prod_{s=L(\mu-1)+1}^{\mu L} \hat{X}_s \quad (\text{A.24})$$

$$= 2\mathbf{I} \quad (\text{shown}). \quad (\text{A.25})$$

Second, without loss of generality, consider  $\mu < \lfloor L/2 \rfloor$  and note that  $\hat{X}_\mu \hat{Z}_\mu = -i \hat{Y}_\mu$ ,

$$\hat{\rho}_\mu^{(L)} \hat{\rho}^{(L)} = \prod_{r=1}^{\mu-1} \hat{Z}_{rL} \prod_{r=L(\mu-1)+1}^{\mu L} \hat{X}_r \prod_{s=1}^{-1} \hat{Z}_{sL} \prod_{s=L(-1)+1}^L \hat{X}_s \quad (\text{A.26})$$

$$= -i \prod_{r=(\mu-1)L+1}^{\mu L-1} \hat{X}_r \hat{Y}_{\mu L} \prod_{r=\mu+1}^{-1} \hat{Z}_{rL} \prod_{r=(L-1)L+1}^L \hat{X}_r \quad (\text{A.27})$$

where here, the Pauli-Y subscript  $\mu L = \mu \cdot L$  refers to the qubit order. Therefore, by noting

$\hat{Z}_\mu \hat{X}_\mu = i \hat{Y}_\mu$ , then,

$$\{\hat{\rho}_\mu^{(L)}, \hat{\rho}^{(L)}\} = \hat{\rho}_\mu^{(L)} \hat{\rho}^{(L)} + \hat{\rho}^{(L)} \hat{\rho}_\mu^{(L)} \quad (\text{A.28})$$

$$\begin{aligned} &= -i \prod_{r=(\mu-1)L+1}^{\mu L-1} \hat{X}_r \hat{Y}_{\mu L} \prod_{r=\mu+1}^{-1} \hat{Z}_{rL} \prod_{r=(L-1)L+1}^L \hat{X}_r \\ &+ i \prod_{s=(\mu-1)L+1}^{\mu L-1} \hat{X}_s \hat{Y}_{\mu L} \prod_{s=\mu+1}^{-1} \hat{Z}_{sL} \prod_{s=(L-1)L+1}^L \hat{X}_s \end{aligned} \quad (\text{A.29})$$

$$= 0 \quad (\text{shown}). \quad (\text{A.30})$$

### A.3 Slater Determinant and $L$ -wise Correlated Ansatz using Givens Rotations

In the main text, the Clifford loaders  $\hat{C}$ , consisting of multiple Givens rotations, can be used to prepare Slater determinant  $|\Psi_1(\mathbf{A})\rangle$  as follows

$$|\Psi_1(\mathbf{A})\rangle = \prod_{l=1}^d \hat{C}(A_l) |\text{vac}\rangle. \quad (\text{A.31})$$

Here, the aim is to show that Eq. (A.31) can be mathematically evaluated using

geometric algebra, also known as real Clifford algebra. The Clifford loader  $\hat{C}(x)$  for a given normalized sized- $N$  vectors  $x$  is defined as a linear combination of anti-commuting operators  $\hat{\rho}_r$  as follows

$$\hat{C}(x) = \sum_{\mu=1}^N x_{\mu} \hat{\rho}_{\mu}. \quad (\text{A.32})$$

A geometric product of two Clifford loaders  $\hat{C}(x)\hat{C}(y)$  for any two normalized sized- $N$  vectors  $x, y$  is defined as

$$\hat{C}(x)\hat{C}(y) = \hat{C}(x) \cdot \hat{C}(y) + \hat{C}(x) \wedge \hat{C}(y), \quad (\text{A.33})$$

where  $\cdot$  and  $\wedge$  refers to the standard inner dot and exterior wedge product, respectively.

Substituting the definition Eq. (A.32) into Eq. (A.33),

$$\hat{C}(x)\hat{C}(y) = \sum_{r=1}^N x_r y_r (\hat{\rho}_r \cdot \hat{\rho}_r) + \sum_{\mu, \nu=1}^N x_{\mu} y_{\nu} (\hat{\rho}_{\mu} \wedge \hat{\rho}_{\nu}). \quad (\text{A.34})$$

In this work, consider only orthogonal and normalized sized- $N$  vectors  $A_l$  for  $l = 1, 2, \dots, d$ , such that the inner product of any two vectors is zero. As a result, the geometric product of two Clifford loader is simply equivalent to the its exterior product as the first term of Eq. (A.34) vanishes under orthogonality. Thus, products of multiple Clifford loaders can be easily written as exterior product of mutiple anti-commuting operators

$$\prod_{l=1}^d \hat{C}(A_l) = \sum_{\mu, \dots, r=1}^N A_{\mu 1} A_{2 \dots} A_{r d} \underbrace{(\hat{\rho}_{\mu} \wedge \hat{\rho}_{\dots} \wedge \hat{\rho}_r)}_{d \text{ operators}}. \quad (\text{A.35})$$

Note the following identities of exterior product

$$\hat{\rho}_\mu \wedge \hat{\rho}_\mu = 0, \quad (\text{A.36})$$

and

$$\hat{\rho}_{\pi(1)} \wedge \hat{\rho}_{\pi(2)} \wedge \dots \wedge \hat{\rho}_{\pi(d)} = \text{sgn}(\pi) \hat{\rho}_{B_1} \wedge \hat{\rho}_{B_2} \wedge \dots \wedge \hat{\rho}_{B_d}, \quad (\text{A.37})$$

where  $\pi$  is a permutation of  $\{B_1, B_2, \dots, B_d\}$  for any ordered set  $B$  containing  $d$  unique integers between 1 and  $N$ ,  $B_\mu$  and  $\pi_\mu$  refers to the  $\mu^{\text{th}}$  integer of  $B$  and  $\pi$ , respectively. Using the above identities (A.36) and (A.37), the sum in Eq. (A.35) reduces to

$$\hat{C}(A_I) = \sum_{|B|=d} \sum_B \text{sgn}(\pi) A_{\pi(1)1} A_{\pi(2)2} \dots A_{\pi(d)d} (\hat{\rho}_{B_1} \wedge \hat{\rho}_{B_2} \wedge \dots \wedge \hat{\rho}_{B_d}), \quad (\text{A.38})$$

where the outer sum is over all possible combinations of the ordered set  $B$  containing  $d$ -unique integers between 1 and  $N$  and the inner sum is over all possible integer permutation  $\pi$  of each  $B$ . Using the Leibniz determinant formula for matrix minors

$$\det(A_B) = \sum_B \text{sgn}(\pi) A_{\pi(1)1} A_{\pi(2)2} \dots A_{\pi(d)d}, \quad (\text{A.39})$$

where  $A_B$  is a  $d \times d$  matrix minor of  $\mathbf{A}$  whose rows are restricted to  $B$ , then,

$$\hat{C}(A_I) = \sum_{|B|=d} \det(A_B) \hat{\rho}_{B_1} \wedge \hat{\rho}_{B_2} \wedge \dots \wedge \hat{\rho}_{B_d}. \quad (\text{A.40})$$

Hence, by letting the anti-commuting operator be

$$\hat{\rho}_\mu = \hat{a}_\mu^\dagger + \hat{a}_\mu, \quad (\text{A.41})$$

and applying the product of  $d$  Clifford loaders (A.40) onto a vacuum state  $|vac\rangle$ , the alternative expression of the Slater determinant is obtained

$$\hat{C}(A_I)|vac\rangle = \det(\mathbf{A}_B)|B\rangle, \quad (\text{A.42})$$

$I=1$   $|B|=d$

where  $|B\rangle$  denotes a Fock state whose occupied modes are indexed by  $B$ .

Next, consider extending the application of Clifford loaders to prepare  $L$ -wise correlated ansatz states, where  $L = 1$  reduces to the Slater determinant case. The idea is to use a new set of anti-commuting operators  $\hat{\rho}_\mu^{(L)}$  that contains non-particle preserving multi-body Fock operators for the Clifford loaders in Eq. (A.32). In the main text, under the Jordan-Wigner mapping, the anti-commuting operator  $\hat{\rho}_\mu = \prod_{r=1}^{\mu-1} \hat{Z}_r \hat{X}_\mu$  in Eq. (A.41) used to prepare the Slater determinant above is modified to become

$$\hat{\rho}_\mu^{(L)} = \prod_{r=1}^{\mu-1} \hat{Z}_{rL} \prod_{r=L(\mu-1)+1}^{\mu L} \hat{X}_r, \quad (\text{A.43})$$

to apply  $L$ -wise correlation, where  $r$  index here increments with size  $L$  from  $L$  to  $L(\mu-1)$ . Here, the Pauli-Z subscript  $rL = r \cdot L$  refers to the qubit order. This modified operator  $\hat{\rho}_\mu^{(L)}$  has  $L$  Pauli-X terms and  $\mu$  Pauli-Z terms with modulo  $L$  indexes such that  $\{\hat{\rho}_\mu^{(L)}, \hat{\rho}_\mu^{(L)}\} = 2 \mu \mathbf{I}$ . For example, the  $L = 2$  pairwise correlated anti-commuting operators is given as  $\hat{\rho}_\mu^{(2)} = \hat{Z}_2 \hat{Z}_4 \hat{Z}_6 \dots \hat{Z}_{2\mu-2} \hat{X}_{2\mu-1} \hat{X}_{2\mu}$ . In terms of Fermionic creation and annihilation operators,

Eq. (A.43) maps to back to

$$\rho_\mu^{(L)} = \begin{cases} \prod_{r=1}^{\mu-1} (\mathbf{I} - 2\hat{a}_{rL}^\dagger \hat{a}_{rL}) \prod_{r=L(\mu-1)+1}^{\mu L} [\hat{a}_r^\dagger + (-1)^r \hat{a}_r] & \text{if } L \text{ is even,} \\ - \prod_{r=1/LZ}^{L(\mu-1)-1} (\mathbf{I} - 2\hat{a}_r^\dagger \hat{a}_r) \prod_{r=L(\mu-1)+1}^{\mu L} [\hat{a}_r^\dagger + (-1)^{r-L(\mu-1)-1} \hat{a}_r] & \text{if } L \text{ is odd,} \end{cases} \quad (\text{A.44})$$

Here in Eq. (A.44), the fermionic operator subscript  $rL = r \cdot L$  refers to the mode index. All fermionic terms when in normal ordered form that contain any annihilation operators will vanish when acted upon by a vacuum state and fermionic terms that contain only creation operators will survive. Thus, by substituting Eq. (A.44) into the product of  $\frac{d}{L}$  Clifford loaders Eq. (A.40) and applying it onto a vacuum state  $|\text{vac}\rangle$ , the  $L$ -wise correlated ansatz state is obtained up to an unobservable global phase

$$\sum_{|B|=\frac{d}{L}} \prod_{l=1}^{\frac{d}{L}} \hat{C}_L(G_l) |\text{vac}\rangle \det(\mathbf{G}_B) |B_L\rangle, \quad (\text{A.45})$$

where the sum is over all possible combinations ordered set  $B$  containing  $\frac{d}{L}$  unique integers between 1 and  $\frac{N}{L}$ ,  $\mathbf{G}_B$  is a  $\frac{d}{L} \times \frac{d}{L}$  matrix minor of  $\mathbf{G}$  whose rows are restricted to  $B$ ,  $B_L = \{L(j-1)+1, L(j-1)+2, \dots, Lj | j \in B\}$  and  $|B_L\rangle$  denotes a  $N$ -mode Fock basis whose occupied mode are indexed by  $B_L$ .

## A.4 Givens Rotation Gate Decomposition for the $L$ -wise Correlated Ansatz State

Given rotation gate is defined in the main text as

$$\hat{U}_\mu^{(L)}(\cdot) = \exp[\hat{\rho}_\mu^{(L)} \hat{\rho}^{(L)}], \quad (\text{A.46})$$

where using anti-commuting operators in Eq. (A.43), it becomes

$$\hat{U}_\mu^{(L)}(\theta) = \exp \left[ -i \prod_{r=L(\mu-1)+1}^{\mu L-1} \hat{X}_r \hat{Y}_{\mu L} \prod_{r=L(\mu-1)+1}^L \hat{X}_r \prod_{r=\mu+1}^{\mu L-1} \hat{Z}_r \right]. \quad (\text{A.47})$$

Here, the Pauli operators subscript  $rL = r \cdot L$  refers to the qubit order. For example, a  $L = 2$  pairwise Givens rotation would be

$$\hat{U}_\mu^{(2)}(\theta) = \exp \left[ -i \hat{X}_{2\mu-1} \hat{Y}_{2\mu} \hat{X}_{2\mu-1} \hat{X}_{2\mu} \hat{Z}_{2(\mu+1)} \hat{Z}_{2(\mu+2)} \cdots \hat{Z}_{2(\mu-1)} \right], \quad (\text{A.48})$$

where it can be easily decomposed as shown in Fig. A.1 using gate decomposition techniques from [241]. Therefore, the Givens rotation gate  $\hat{U}_\mu^{(L)}(\theta)$  used in this work is simply a Pauli-string rotation gate where its gate decomposition is a generalization of Fig. A.1 as shown in Fig. 3(b) of the main text.

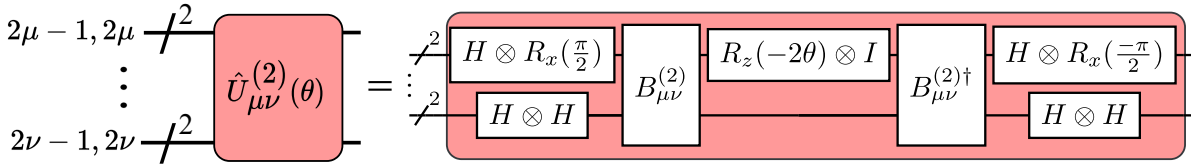


Figure A.1: The pairwise Givens rotation gate  $\hat{U}_{\mu\nu}^{(2)}$  is decomposed using Pauli rotation gates  $R_x$  that acts on qubit  $2\mu$  that correspond to  $\hat{Y}_{2\mu}$ ,  $R_z$  that acts on qubit  $2\mu-1$ , Hadamards  $H$  and CNOT ladders  $B_{\mu\nu}^{(L)}$  that acts on all 3 qubits in  $\{2\mu-1, 2\mu-1, 2\mu\}$  that corresponds to  $\hat{X}_{2\mu-1} \hat{X}_{2\mu-1} \hat{X}_{2\mu}$ , with  $B_{\mu\nu}^{(L)}$  also acting on  $-\mu$  additional qubits in  $\{2\mu, 2(\mu+1), 2(\mu+2), \dots, 2(\mu-1)\}$ .  $\theta$  is a scalar parameter.

# Appendix B

## Resource-Efficient

## Quantum-Assisted Simulator

### B.1 Modified Hadamard Test for Parallel Gates

The standard Hadamard Test estimates the real and imaginary components of  $|\hat{U}|$  using an ancilla qubit and an  $N$ -system-qubit unitary  $\hat{U}$  gate controlled by the ancilla qubit, as shown in Fig. B.1.

This creates a problem: parallel gates in the gate decomposition of  $\hat{U}$  must be serialized

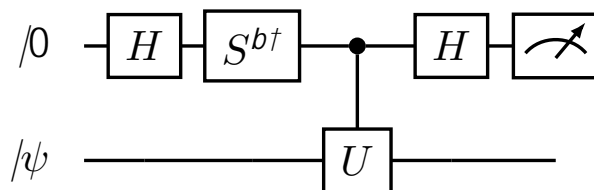


Figure B.1: Standard Hadamard Test that estimates real and imaginary parts of  $|\hat{U}|$  for  $b = 0$  and  $1$ , respectively.

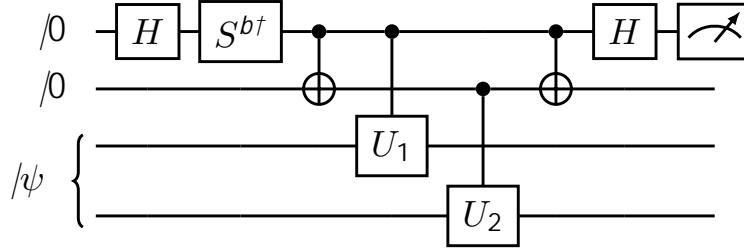


Figure B.2: Modified Hadamard test with two ancilla qubits initialized in  $|0\rangle$  and two sets of system qubits initialized in  $|\psi\rangle$ .

when gate control by the ancilla qubit is applied. This problem can be solved by using more ancilla qubits. As a simple example, let the  $N$ -system-qubit unitary  $\hat{U}$  gate be

$$\hat{U} = \hat{U}_1 \hat{U}_2, \quad (\text{B.1})$$

where  $\hat{U}_1$  and  $\hat{U}_2$  act on two separate sets of system qubits. Then, consider the following modified Hadamard Test that uses two ancilla qubits, as shown in Fig. B.2. The first three quantum gates on the left of the modified Hadamard test circuit in Fig. B.2 generate an ancilla Bell state  $|00\rangle + |11\rangle$  if  $b = 0$  or  $|00\rangle - i|11\rangle$  if  $b = 1$ , where the state normalization is ignored to reduce verbosity. Next,  $\hat{U}_1$  controlled by the top ancilla qubit and  $\hat{U}_2$  controlled by the bottom ancilla qubit are applied to prepare  $|00\rangle / \sqrt{2} + |11\rangle \hat{U} / \sqrt{2}$  if  $b = 0$  or  $|00\rangle / \sqrt{2} - i|11\rangle \hat{U} / \sqrt{2}$  if  $b = 1$ . Then, the inverse of operator that generates the ancilla Bell state, without any phase gates  $S$ , is applied. Finally, the top ancilla qubit is measured in the Pauli-Z basis. The Pauli-Z expectation value  $\langle Z \rangle$  will give the real and imaginary components of  $\langle \hat{U} \rangle$  for  $b = 0$  and 1, respectively.

To maximize gate parallelism, it is sufficient to have  $N$  ancilla qubits. Doing so will require one to prepare an  $N$ -qubit ancilla Greenberger–Horne–Zeilinger (GHZ) state, as shown

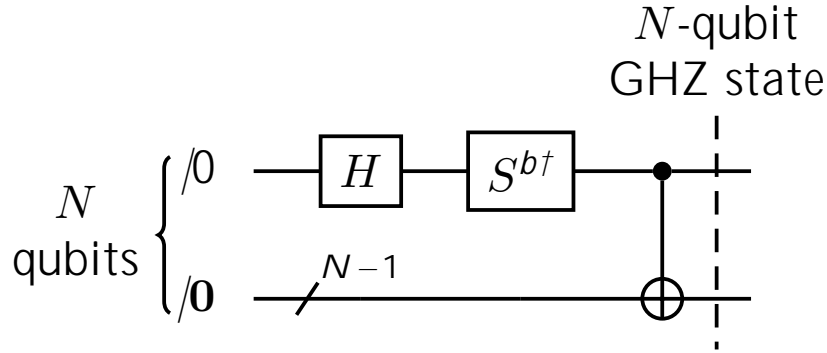


Figure B.3: Quantum circuit preparation of  $N$ -qubit GHZ state [304]. The CNOT gate with an arrow represents a cascade of CNOTs gates, known as a CNOT ladder, as shown in Fig. 3.7

in Fig. B.3. That is,  $|0 \cdots 0\rangle + |1 \cdots 1\rangle$  if  $b = 0$  or  $|0 \cdots 0\rangle - i|1 \cdots 1\rangle$  if  $b = 1$ , instead of an ancilla Bell state.

## B.2 Quantum Resource-Efficient Regime

Here, the total quantum runtime complexity between the standard method and the Quantum-Assisted Simulator (QAS), as described in Chapter 5 are compared. In addition, the condition that QAS has to fulfill in order to be more quantum resource-efficient than standard methods is also derived. Consider a system of qubit size  $N$ , described by a time-independent Hamiltonian  $\hat{H}$ , initialized in an unknown state  $|\psi_0\rangle$ , the goal is to solve the quantum dynamics described by an observable  $\hat{O}$  at fixed time intervals  $\Delta t$  up to a total simulation time  $T$ .

Assume both the Hamiltonian  $\hat{H}$  and observable  $\hat{O}$  decompose into a linear combination of  $L$  Pauli strings  $\hat{P}_l = \sum_{j=1}^N \hat{\sigma}_j$ , where  $\hat{\sigma}_j \in \{\hat{I}_j, \hat{X}_j, \hat{Y}_j, \hat{Z}_j\}$ , which may or may not share the same Pauli string. The quantum runtime complexity of existing quantum algorithms that simulate the  $e^{-i\hat{H}t}$  time propagator for a fixed simulation time of  $\Delta T$ , up to a time evolution error  $\|e^{-i\hat{H}t} - \hat{U}\|$ , is upper bounded by  $O(\text{Poly}_{\hat{U}}(L, \epsilon^{-1}, \Delta t))$  as shown in Table B.1. Thus,

Algorithms Simulating $e^{-i\hat{H}t}$	Quantum runtime complexity
1 <sup>st</sup> Order Trotter [8, 120, 121]	$O(L^3(t \hat{H}_{\max})^2/)$
2 <sup>nd</sup> Order Trotter [8, 120, 121]	$O(L^{\frac{5}{2}}(t \hat{H}_{\max})^{\frac{3}{2}}/ \frac{1}{2})$
2k <sup>th</sup> Order Trotter [8, 9]	$O(5^{2k}L(Lt \hat{H}_{\max})^{1+\frac{1}{2k}}/ \frac{1}{2k})$
Qubitization [133]	$O[t + \log(1/)/\log \log(1/)]$
Linear Combination of Unitaries [129]	$O[t \log(t /)/\log \log(t /)]$
Quantum Signal Processing [132]	$O(t \hat{H}_{\max} + \log(1/)/\log \log(1/))$
Stochastic Simulation (QDRIFT) [271]	$O((t /)^2/)$

Table B.1: The quantum runtime or gate complexity of various quantum algorithms simulating  $e^{-i\hat{H}t}$  time propagator, that are upper bounded by  $O(\text{Poly}_{\hat{U}}(L, \rho_l^{-1}, t))$ , for a time-independent Hamiltonian  $\hat{H}$  and up to a simulation time  $t$  [118]. Here  $\hat{H}_{\max}$  is the largest absolute element of  $\hat{H}$  and  $\rho_l = \sum_i |\rho_i|$  is the sum of all Pauli coefficients of the Pauli-form of Hamiltonian  $\hat{H}$ .

performing the time evolution for a simulation time of  $j\Delta t$ , where  $j \in \mathbb{Z}$  is a non-negative integer, incurs a quantum runtime complexity of  $j \cdot O(\text{Poly}_{\hat{U}}(L, \rho_l^{-1}, \Delta t))$  from applying the  $e^{-i\hat{H} \cdot t}$  time propagator  $j$  times on the initial state.

Due to wavefunction collapse and no-fast-forwarding theorem, the standard approach involves preparing  $L$  copies of time-evolved states at times  $\{j\Delta t | j = 0, 1, \dots, \frac{T}{\Delta t}\}$  for Pauli measurements. Since, QAS will later assume access to a  $2N$ -qubit quantum computer, the standard approach can be parallelized by running two independent the time-evolution at a time, reducing the overall runtime by a factor of 2. Therefore, the overall quantum runtime complexity of the standard approach is

$$\frac{1}{2} \cdot L \cdot \sum_{j=0}^{T/\Delta t} j \cdot O(\text{Poly}_{\hat{U}}(L, \rho_l^{-1}, \Delta t)) = \frac{1}{4} \frac{T}{\Delta t} \left( \frac{T}{\Delta t} + 1 \right) \cdot L \cdot O(\text{Poly}_{\hat{U}}(L, \rho_l^{-1}, \Delta t)). \quad (\text{B.2})$$

For the QAS, the quantum computer is used only for estimating the real and imaginary

components of the overlap  $F$ , Hamiltonian  $H$ , and observable  $O$  matrices, as shown in Chapter 5.2.3. Consider choosing  $n$  time-evolved states  $|j\rangle = e^{-i\hat{H}s_j}|0\rangle$  as basis, where  $j = \{0, 1, \dots, n-1\}$  and parameter times  $0 = s_0 < s_1 < \dots < s_{n-1} \leq T$  are not longer than the total simulation time  $T$ . Then, the aforementioned matrix elements consist of the quantities  $F_{jk} = \langle 0|e^{i\hat{H}s_j} s_k|0\rangle$  and  $P_{jkl} = \langle 0|\hat{P}_l e^{i\hat{H}s_j} s_k|0\rangle$  as shown in Eqs. (5.29) and (5.30), respectively, where  $k = \{0, 1, \dots, n-1\}$ ,  $\Delta s_{jk} = s_j - s_k$  are the parameter time differences and  $l = \{0, 1, \dots, 2L\}$ . In total, there are  $n^2 + 2Ln^2 = O(Ln^2)$  such quantities combined. These quantities can be estimated using the modified Hadamard test from Appendix B.1. It requires a controlled- $e^{-i\hat{H}t}$  time propagator that has a longer quantum runtime complexity than a standard  $e^{-i\hat{H}t}$  time propagator by at most a constant factor of 4. Thus, the overall quantum runtime complexity of the QAS is

$$2 \cdot 2 \cdot L \cdot \sum_{j,k=0}^{n-1} \frac{\Delta s_{jk}}{\Delta t} \cdot O(\text{Poly}_{\hat{U}}(L, n^{-1}, \Delta t)) < 4 \cdot n^2 \cdot \frac{T}{\Delta t} \cdot L \cdot O(\text{Poly}_{\hat{U}}(L, n^{-1}, \Delta t)), \quad (\text{B.3})$$

where following inequality is applied,

$$\sum_{j,k=0}^{n-1} \Delta s_{jk} < Tn^2. \quad (\text{B.4})$$

Comparing the runtime complexities Eqs. (B.2) and (B.3), the condition for the QAS to be more resource-efficient is found to be,

$$\frac{T}{\Delta t} \ll 16 \cdot n^2 - 1. \quad (\text{B.5})$$

By the observation that a 3-qubit Toffoli gate can be decomposed into 6 CNOT gates, consider

the assumption that  $\frac{T}{\Delta t} \gg 6$  and thus the condition in Eq. (B.5) simplifies to

$$\frac{T}{\Delta t} \gg 100r^2 \gg 16 \cdot 6 \cdot r^2 - 1. \quad (\text{B.6})$$

### B.3 Sampling Basis State Overlaps, Hamiltonian and Observable Elements.

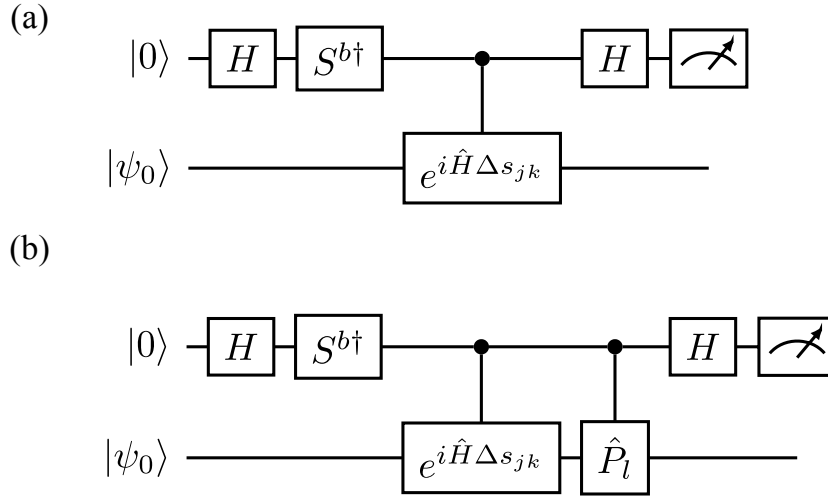


Figure B.4: Hadamard test for estimating the real ( $b=0$ ) and imaginary components ( $b=1$ ) of (a)  $F_{jk}$  and (b)  $P_{jkl}$  quantities.

Here, for the ease of presentation, consider using the standard Hadamard Test with one ancilla qubit to estimate the real and imaginary components of the overlap  $F$ , Hamiltonian  $H$  and observable  $O$  matrices using an ancilla qubit. The aforementioned matrix elements consist of the following quantities:  $F_{jk} = \langle 0 | e^{i\hat{H} s_{jk}} | 0 \rangle$  and  $P_{jkl} = \langle 0 | \hat{P}_l e^{i\hat{H} s_{jk}} | 0 \rangle$  as shown in Eqs. (5.29) and (5.30), respectively, where  $j = \{0, 1, \dots, n-1\}$ ,  $k = \{0, 1, \dots, n-1\}$ ,  $l = \{0, 1, \dots, 2L\}$ ,  $n$  is the number of basis states,  $\Delta s_{jk} = s_j - s_k$  are the time differences,  $L$  is the maximum number of Pauli elements in the Hamiltonian  $\hat{H}$  or the observable  $\hat{O}$  operators,  $0 = s_0 < s_1 < \dots < s_{n-1} = T$  are the time parameters. Both  $F_{jk}$  and  $P_{jkl}$  can be estimated

using the standard Hadamard Test with one ancilla qubit shown in Fig. B.4.

The real and imaginary component of the quantities can be estimated by the Pauli-Z expectation value of the ancilla qubit  $Z$  for  $b = 0$  and  $b = 1$ , respectively. Assuming noiseless quantum circuits and measurements, the  $N_s$ -shots measurement statistics of the ancilla qubit can be treated as a normal distribution with its mean equal to the Pauli-Z expectation value of the ancilla qubit  $Z$  and its variance  $\text{Var}(\hat{Z}) = \frac{1 - \langle \hat{Z} \rangle^2}{N_s}$ . Thus, a sample set of the matrices are obtained by sampling the corresponding normal distributions once for each real and an another for each imaginary components of the corresponding quantities, respectively.

## B.4 Energy Dynamics of Helium Atom and Hydrogen Molecule

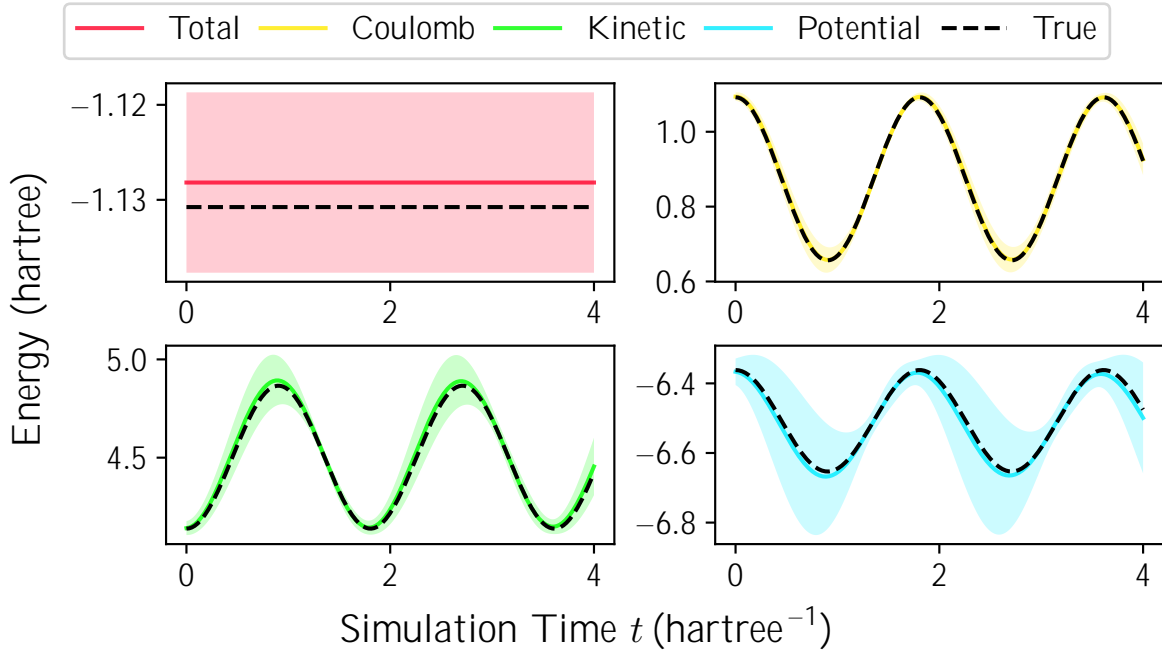


Figure B.5: Energy dynamics for Helium Atom, using the 6-31G basis set, initialized in an equal superposition of the ground and highest excited state of eigenenergies -2.87 and 0.609 Hartrees, respectively.

The energy dynamics of the He atom and  $\text{H}_2$  molecule are plotted in Figs. B.5 and B.6,

respectively. Both initialized in an equal superposition of its ground and highest excited state. The solid colored line and shaded regions represent the mean and uncertainty, respectively, of 100 independent QAS simulation samples, each with  $10^4$  simulated shots. The true time-evolution is denoted by the black dashed line. The top left plots of both figures show the total energy which represents the expectation value of the electronic Hamiltonian of the He atom and H<sub>2</sub> molecule correspondingly. The top right plots show the Coulomb energy which represents the sum of all interaction energy between two electrons due to Coulomb repulsion. The bottom left plots show the kinetic energy, that is the sum of all one-electron kinetic energies. The bottom right plots show the potential energy which represents the sum of all one-electron potential energy of electrons due to nuclear attraction.

For both systems, the total energy is observed to be conserved throughout the entire simulation time, with a fractional energy uncertainty of about 0.8% and 4% for He atom and H<sub>2</sub> molecule case, respectively. For the Coulomb energy, the fractional energy uncertainty of about 6% and 13% for He atom and H<sub>2</sub> molecule case, respectively. For the kinetic energy, the fractional energy uncertainty of about 3% and 5% for He atom and H<sub>2</sub> molecule case, respectively. For the potential energy, the fractional energy uncertainty of about 0.5% and 2% for He atom and H<sub>2</sub> molecule case, respectively. Despite the seemingly-good accuracy and reasonable precision, some energy oscillations cannot be precisely determined, especially the potential energy plots for both cases. This is due to the energy magnitude being larger than the energy oscillating amplitude. A larger number of shots is required to improve the precision of measuring energy oscillating amplitude.

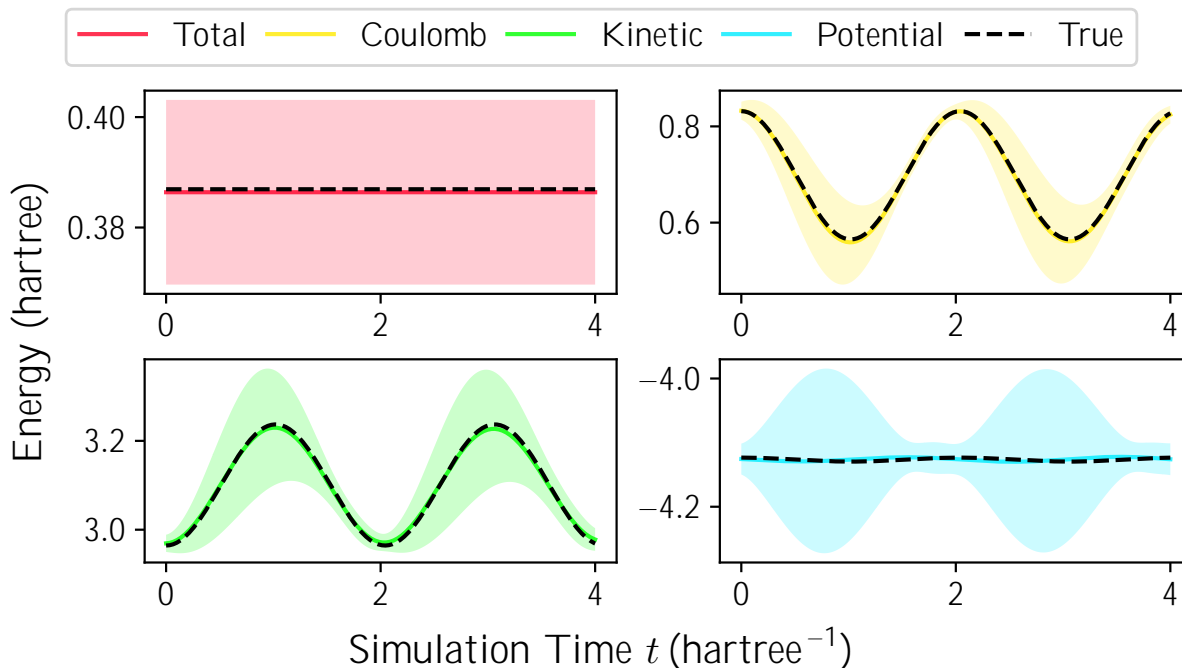


Figure B.6: Energy dynamics for Hydrogen molecule, using the 6-31G basis set, at equilibrium distance of 1.4 Bohr, initialized in an equal superposition of the ground and highest excited state of eigenenergies -1.15 and 1.93 Hartrees, respectively.

## B.5 Variance of Observed Quantities against Number of Shots

The variance of the orbital population and energy against a range of shots between  $10^3$  to  $10^{10}$  per real or imaginary evaluation of basis state overlap and Hamiltonian element are plotted, for the He atom in Figs. B.7 and B.8, respectively, and for the H<sub>2</sub> molecule in Figs. B.9 and B.10. All plots show that the variance is directly proportional to the number of shots, as expected for shot noise.

## B.5.1 Helium Atom Case

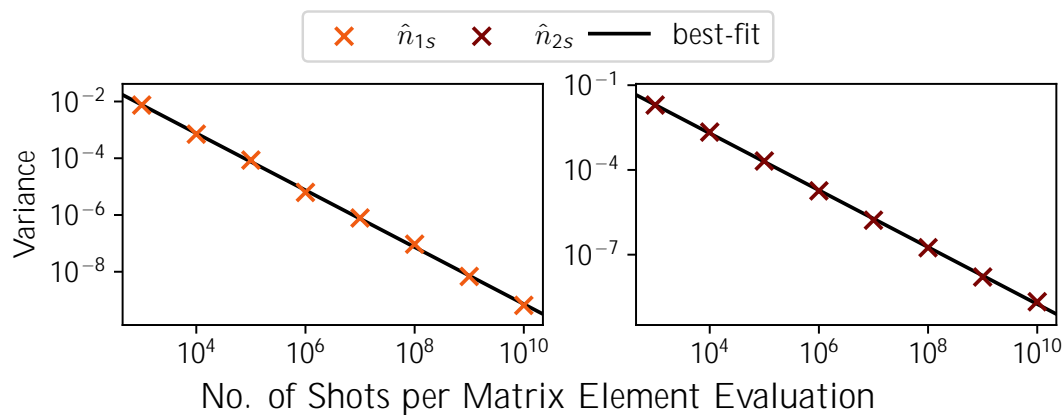


Figure B.7: Atomic orbital population variance for 100 independent QAS samples runs for Helium Atom, using the 6-31G basis set.

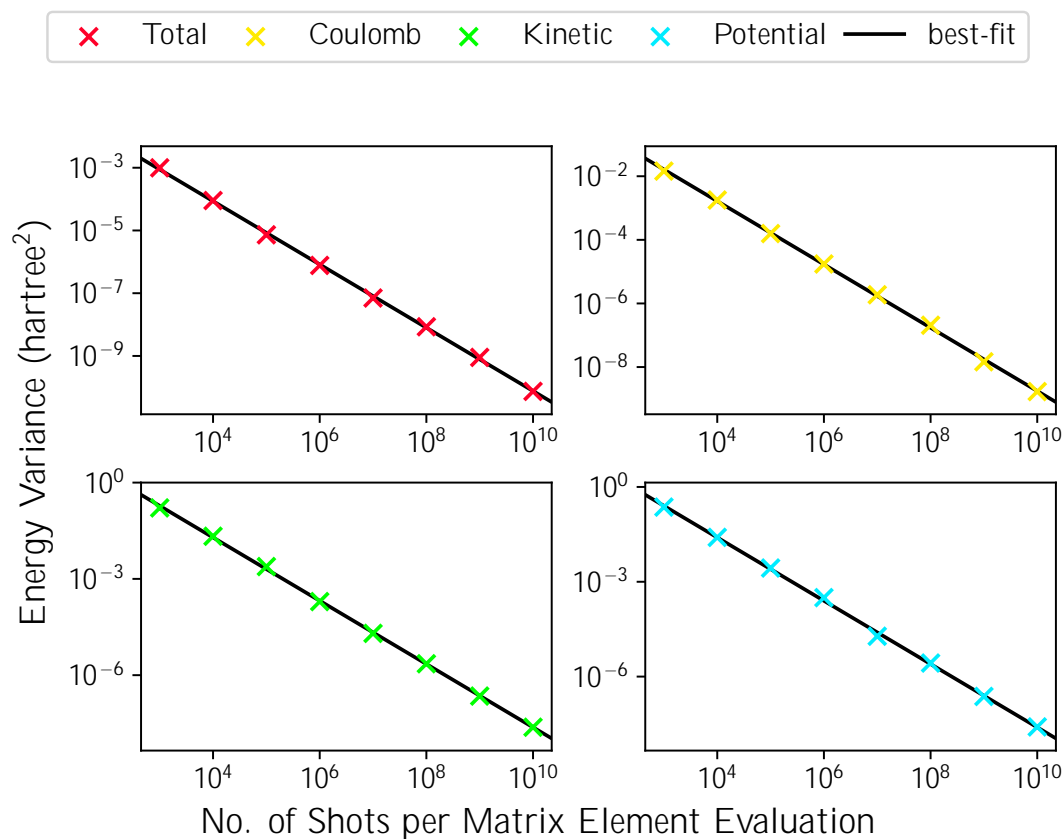


Figure B.8: Energy variance for 100 independent QAS samples runs for Helium Atom, using the 6-31G basis set.

### B.5.2 Hydrogen Molecule Case

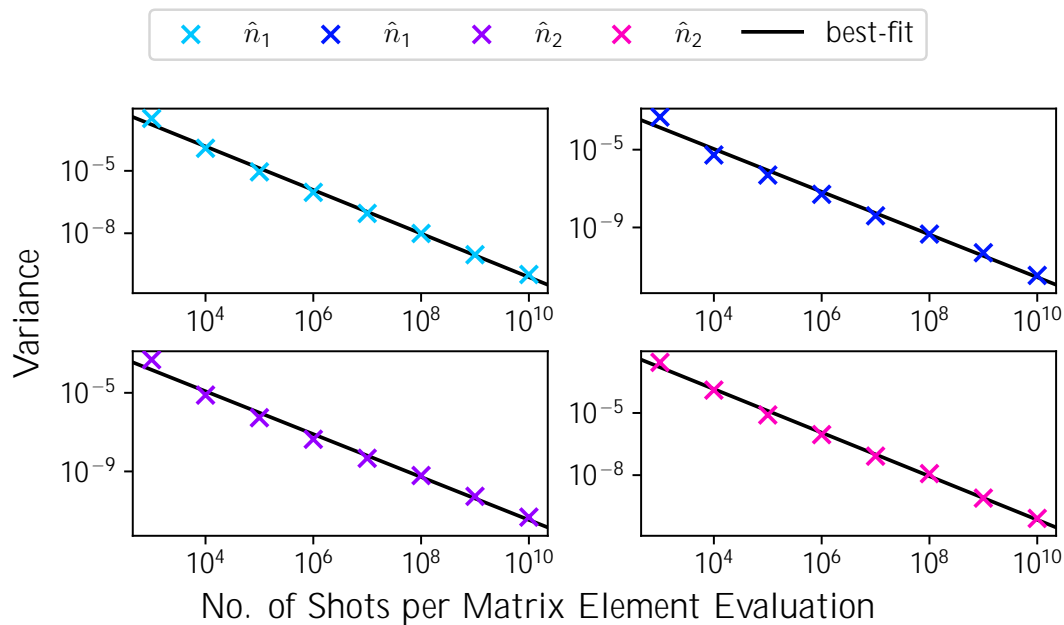


Figure B.9: Molecular orbital population variance for 100 independent QAS samples runs for Hydrogen molecule, using the 6-31G basis set.

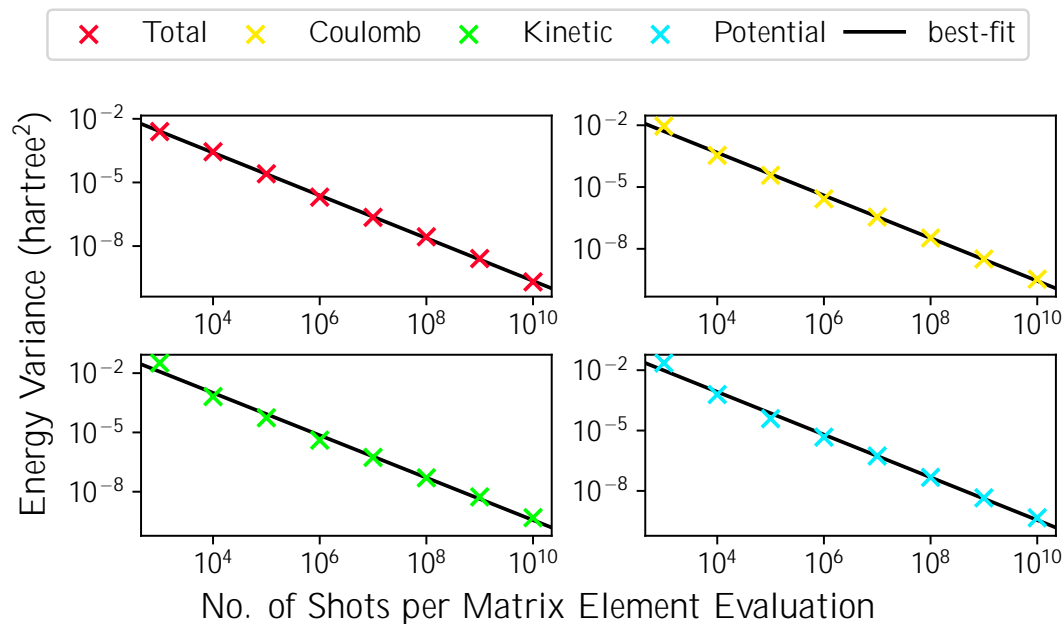


Figure B.10: Energy variance for 100 independent QAS samples runs for Hydrogen molecule, using the 6-31G basis set.

## B.6 First Order Trotterized Time-Evolved Basis States

The first order Trotterization is implemented on the basis  $| \psi_1 \rangle = e^{-i\hat{H}/2} | \psi_0 \rangle$  and the QAS simulation of the Helium atom is repeated. Fig. B.11 plots the state infidelity of the final time-evolved state at the simulation time of  $t=4$  Hartree $^{-1}$  against a range of Trotter steps up to  $10^4$  steps for a range of shots between  $10^4$  and  $10^{10}$ . The results show that state infidelity improves at larger Trotter steps, but quickly plateaus beyond a finite number of steps as the shot noise becomes the limiting factor.

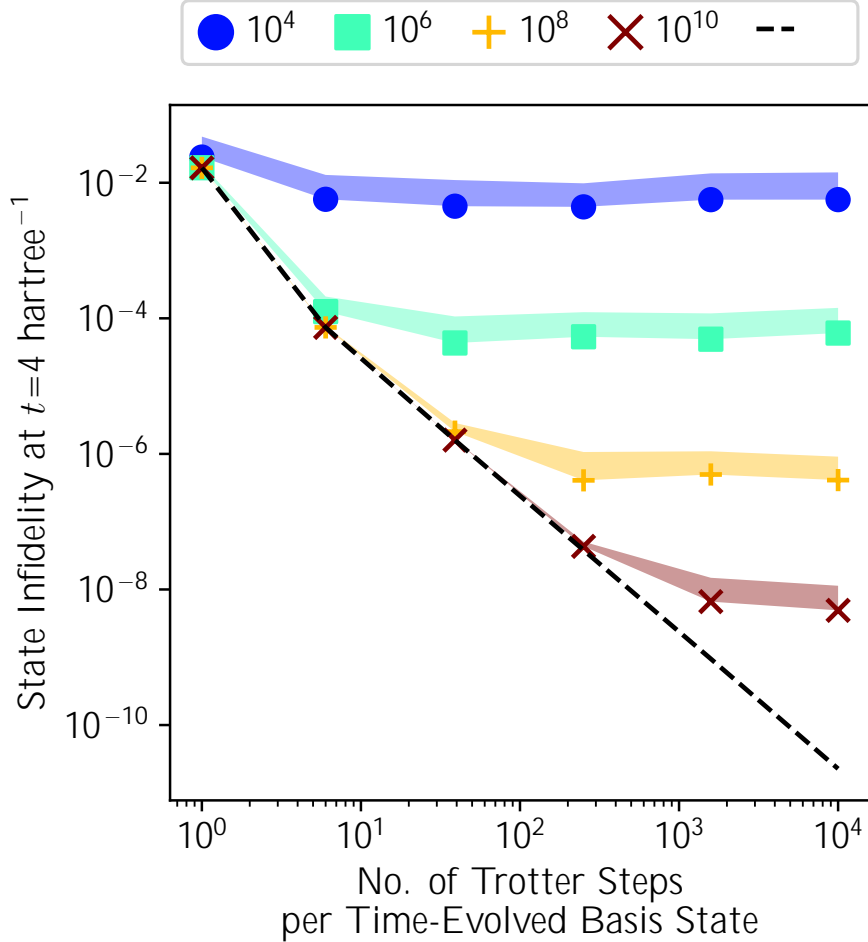


Figure B.11: State infidelity after a simulation time of  $t=4$  Hartree $^{-1}$  as a function of the number of first-order Trotter steps implemented per time-evolved basis state, ranging from 1 to  $10^4$  steps, at various number of shots ranging from  $10^4$  to  $10^{10}$  shots per real and per imaginary evaluation of basis state overlap and Hamiltonian element.

## B.7 Linear Dependence of the Time-Evolved Basis

The time-evolved basis is linearly independent if and only if the basis state overlap  $\mathbf{F}$  is invertible. As basis overlap is defined using the  $L^2$ -inner product,  $\mathbf{F}$  is also semi-positive definite, that is all of the eigenvalues of  $\mathbf{F}$  is either zero or positive real-valued. Using the above properties of the basis state overlap, for  $n = 2$  basis set size, the basis linear independence condition for parameter time  $s_1$  can be derived.

Consider having  $n = 2$  normalized time-evolved basis  $|0\rangle, |1\rangle = e^{-iHs_1} |0\rangle$ , where  $|0\rangle$  is the initial state. The basis state overlap is

$$\mathbf{F} = \begin{pmatrix} \langle 0|0\rangle & \langle 0|1\rangle \\ \langle 1|0\rangle & \langle 1|1\rangle \end{pmatrix}, \quad (\text{B.7})$$

where

$$\langle 0|0\rangle = \langle 1|1\rangle = 1. \quad (\text{B.8})$$

To ensure that  $\mathbf{F}$  is both invertible and semi-positive definite, it must satisfy

$$0 < \det(\mathbf{F}) \quad (\text{B.9})$$

$$< 1 - |\langle 1|0\rangle|^2. \quad (\text{B.10})$$

Suppose the initial state  $|0\rangle$  is a unknown superposition of  $n = 2$  eigenstates with corresponding eigenvalues  $e_0$  and  $e_1$ , that is

$$|0\rangle = |0\rangle e_0 + |1\rangle e_1, \quad (\text{B.11})$$

such that the unknown coefficients are normalized  $|c_0|^2 + |c_1|^2 = 1$ . Then, the inequality above in Eq. (B.10) can be evaluated to

$$|c_0|^4 + |c_1|^4 + 2|c_0|^2|c_1|^2 \cos[s_1(e_1 - e_0)] < 1, \quad (\text{B.12})$$

which simplifies to

$$s_1 = \frac{2k}{e_1 - e_0}, \quad k \in \mathbb{Z}. \quad (\text{B.13})$$